Dielectric phase gradient metasurfaces for classical and quantum optics applications

Rajath Ravindra Sawant

UNIVERSITÉ CÔTE D'AZUR

ÉCOLE DOCTORALE
SCIENCES FONDAMENTALES ET APPLIQUÉES

THÈSE DE DOCTORAT

Métasurfaces à gradient de phase diélectrique pour les applications d'optique classique et quantique

Rajath SAWANT

Centre de Recherche sur l'Hétéro-Epitaxie et ses Applications

Présentée en vue de l'obtention du grade de docteur en Physique **d'**Université Côte d'Azur

Dirigée par : Dr. Patrice Genevet
Chargé de Recherche CNRS,

Soutenue le : 15 Décembre 2020

Devant le jury, composé de :

Béatrice Dagens, Directrice de recherche CNRS, Center for Nanoscience and Nanotechnology, Palaiseau
Benoît Cluzel, Maître de Conférence-HDR, Laboratoire Interdisciplinaire Carnot de Bourgogne, Dijon
Guillaume Baffou, Chargé de Recherche CNRS, Institut Fresnel, Marseille
Nicolas Bonod, Directeur de recherche CNRS, Institut Fresnel, Marseille
Stéphane Barland, Directeur de recherche CNRS, L'Institut de Physique de Nice, Valbonne

cnrs

erc European Research Council
FLATLIGHT – Grant agreement 639109
Horizon 2020

Métasurfaces à gradient de phase diélectrique pour les applications d'optique classique et quantique

Dielectric Phase Gradient Metasurfaces for Classical and Quantum Optics Applications

Jury:

Rapporteurs

Béatrice Dagens, Directrice de recherche CNRS, Center for Nanoscience and Nanotechnology, Université Paris-Saclay, Palaiseau

Nicolas Bonod, Directeur de recherche CNRS, Institut Fresnel, Aix-Marseille Université, Marseille

Examinateurs

Benoît Cluzel, Maître de Conférence-HDR, Laboratoire Interdisciplinaire Carnot de Bourgogne, Université de Bourgogne, Dijon

Guillaume Baffou, Chargé de Recherche CNRS, Institut Fresnel, Aix-Marseille Université, Marseille

Stéphane Barland, Directeur de recherche CNRS, L'Institut de Physique de Nice, Université Côte d'Azur, Valbonne

Métasurface à gradient de phase diélectrique pour les applications d'optique classique et quantique

Résumé :

Ces dernières années, les diverses fonctionnalités optiques démontrées à l'aide de métasurfaces ont attiré une attention considérable. Les métasurfaces étant des composants optiques diffractifs, présentent une plus grande flexibilité. Ces dispositifs sont notamment plus compacts, plus légers et plus fonctionnels par rapport aux composants optiques réfractifs. Cependant, en termes d'efficacité, les composants réfractifs fonctionnent mieux et il est donc nécessaire d'optimiser les performances des métasurfaces pour assurer leur utilisation et implémentation dans des dispositifs optiques. Compte tenu de cela, nous concevons des dispositifs optiques hybrides pour combiner les avantages des deux composants. Tout d'abord, il est démontré comment la dispersion d'un élément optique simple tel qu'un prisme peut être atténuée à l'aide d'une métasurface. En utilisant des métasurfaces à gradient de phase, les vecteurs d'onde sortants peuvent être contrôlés à l'aide de la dispersion diffractive de la métasurface. Nous avons réalisé des métasurfaces avec gradients de phase relativement petits afin de démontrer expérimentalement l'effet d'atténuation de la dispersion du prisme. Étendant le même principe aux optiques focalisantes, nous avons également conçue des métasurfaces pour corriger les aberrations chromatiques dans la plage de longueurs d'onde de 550 à 800 nm. De plus, il est montré qu'une aberration monochromatique telle qu'une aberration sphérique peut également être corrigée en ajoutant au front d'onde sortant un gradient de phase approprié à l'aide de métasurfaces. Nous montrons également des résultats théoriques et expérimentaux sur la realization de métasurface de grande surface, incluant les caractérisations expérimentales completes, pour démontrer la correction d'aberration d'une lentille disponible dans le commerce. Ces résultats sont très prometteurs notamment pour leurs utilisations dans des systèmes d'imagerie compacts.

Ayant démontré le potentiel des métasurfaces pour l'optique classique, nous nous sommes ensuite intéressé à leur utilization pour des applications en optique quantique. L'expérience de Hong Ou Mandel, qui est l'une des expériences de base de l'optique quantique, démontre l'interférence quantique. Ici, nous proposons de modifier la configuration d'origine en remplaçant le séparateur de faisceau par une métasurface à gradient de phase. Une nouvelle métasurface est conçue à cet effet, appelée «métasurface à double gradients», qui confère des fonctionnalités supplémentaires ainsi que la fonctionnalité de séparateur de faisceau sur des états de polarisations mixtes. La nanofabrication de la métasurface est optimisée pour réaliser une transmission 50/50 dans les deux ordres diffractés pour imiter un séparateur de faisceau. Le contrôle supérieur qu'offrent les métasurfaces sur la phase, la polarisation et l'amplitude de la lumière peut être tout à fait bénéfique pour manipuler les états quantiques de la lumière. Nous résultats permettent d'entrevoir des applications intéressantes pour les technologies quantiques.

Mots clés : Phase de gradient, Compensation de dispersion, Correction d'aberration, Composants hybrides, Méta-correcteur, Nanopillaires, Phase Pancharatnam-Berry Interférence à deux photons, Anti-groupage

Dielectric Phase Gradient Metasurfaces for Classical and Quantum Optics Applications

Abstract:

In recent years, various optical functionalities have been demonstrated using metasurfaces which have attracted tremendous attention. Metasurfaces being diffractive optical components, show greater flexibility, including compactness, lightweight, arbitrary wavefront addressing capabilities exceeding those of refractive optical components. However, in terms of efficiency refractive components perform better and further optimization is required for metasurfaces in this direction. Considering this, here we design hybrid optical devices to combine the advantages of both the components. First, it is demonstrated how the dispersion of a simple optical element such as a prism can be mitigated using a metasurface. By employing phase gradient metasurfaces, the outgoing wavevectors can be controlled and hence the diffractive dispersion of metasurface. Utilizing this property, metasurfaces with relatively small phase gradients are designed and prism dispersion mitigation is experimentally demonstrated. Extending the same principle to lenses, metasurface to correct for lens chromatic aberration is designed in the wavelength range of 550-800nm. Also, it is shown that monochromatic aberration such as spherical aberration can also be corrected by designing an appropriate phase gradient for the metasurface. Analytical calculations, large area metasurface fabrication and comprehensive experimental characterization are done to demonstrate aberration correction of commercially available lenses. These developments are promising for future compact imaging systems.

Realizing the potential of metasurfaces in classical optics, they are also used for Quantum optics applications. However, only a few works have been done in this direction. Hong Ou Mandel experiment, which is one of the basic experiments of Quantum optics, demonstrates quantum interference. Here, we propose to modify the original setup by replacing the beam splitter with a phase gradient metasurface. A novel metasurface is designed for this purpose called 'Dual Gradient Metasurface' which imparts additional functionality along with the beam splitter functionality. The nanofabrication of the metasurface is optimized to realize 50/50 transmission in the two diffracted orders to imitate a beam splitter. The superior control that metasurfaces offer over the phase, polarization and amplitude of light can be quite beneficial for manipulating the quantum states of light. This opens doors for harnessing the potential of metasurface for quantum technologies.

Keywords : Phase gradient, Dispersion compensation, Aberration correction, Hybrid components, Meta-corrector, Nanopillars, Pancharatnam-Berry phase, Two-photon interference, Anti-bunching

Acknowledgements

My journey as a Ph.D. student at CRHEA has been a great learning experience for me, both professionally and personally. There were ups and downs along the way, but it wouldn't have been possible without the support of many people. First of all, I would like to express my gratitude to Dr. Patrice Genevet for guiding and having confidence in me throughout my Ph.D. You have always been an open and friendly advisor and at the same time, you have corrected me when necessary. I am grateful to you for not giving up on me when I failed and giving me the freedom to explore various things. Your enthusiasm for research and positivity has been indeed inspiring to me.

Many people at CRHEA have contributed to my Ph.D. training. Many thanks to Samira Khadir for guiding me in my research when I was stuck. I am grateful to you for helping me to do optical experiments, especially in the last one year and carefully correcting my Ph.D. thesis in your busy schedule. It has always been a pleasant experience to work with you. Special thanks to Sebastien Chenot and Virginie Brandli for the Electron beam lithography and cleanroom training. You were very patient while training me, considering that I had no experience with nanofabrication before. I am also thankful to Patrick Chalbet for providing technical support for our experiments in the optical room. For a foreign student like me, with a lot of paperwork to be done in French, Anne-Marie and Michele Pefferkorn were always my go-to people. Right from the beginning, you have co-operated with me and helped me carry out my work smoothly. I am extremely fortunate to be a part of the 'Flatlight' group at CRHEA, it has been a great team to work with. I would like to mention the co-operation of previous postdocs of the group, Sebastian Heron and Peinan Ni. You both were very helpful during the initial days of my Ph.D. Thank you for teaching me various techniques especially with the nanofabrication process and helping me out when I was stuck in my work. I've learned a lot from the current postdocs Qinghua Song and Renato from our discussions and

collaborative work. I will cherish your friendly company and the skills that I have learned from you. I would like to extend my gratitude to Dr. Konstantin Dorfman for helping me to explore the field of Quantum Optics by collaborating with us. Also, thanks to the researchers at CRHEA with whom I had fruitful discussions; Dr. Jean-Yves Duboz and Dr. Stephanie Rennesson during the preparation of my thesis, Dr. Fabrice Semond during the thesis committee meetings and Dr. Jesus Zuniga Perez for general discussions on Optics.

My colleagues at the 'Open space' office have played a major positive role in my Ph.D. life. It has been a great pleasure for me to have your company. Working always seemed easy and less stressful with all you delightful people. The former students of the office, Roy, Mario, Victor, Ramy, Gauthier, Samuel, thank you guys for making me feel not far away from home when I arrived in France. I will dearly cherish all the house parties, trips and going to the beach at the weekend. I will fondly remember the food that I got to taste from your countries and the things that I got to learn from you all. The current members of the open space, Philip, Sandeep, Colin, Max, Renato, Farsane, Valeria, Huong, Reda, Masoud, you folks were really cool to hang out with. Thank you for keeping the atmosphere light and friendly in the office which made it so easy to work. I will fondly remember all the conversations during lunch and the dinner parties we had, especially the Indian one. Special thanks to Colin 'bhai' for giving me French haircuts that too for free! Sandeep bhai, I cannot thank you enough for your moral support during my Ph.D. You never let me miss India with your Indian dishes and conversations in Hindi. All the philosophical and spiritual discussions we had, did have an impact on me and we will continue our collaboration. Also, thanks to my Indian friends from IISER in Europe for organizing memorable trips in these 3 years.

I would like to express my deep-felt gratitude to my parents, my father for inspiring me to take up higher studies and my mother for being a huge moral support. You have given the best things to me and have been the best parents. I dedicate this little success to you. My brother Kishan has been the best friend and great support to me. Even though you are younger than me, I have learned many things from you. I would like to convey my thanks to my extended family, my Grandparents, Aunts, Uncles and cousins. You all have encouraged and supported me since my childhood. I consider myself privileged for having the opportunity to follow my passion. I am indebted to all the teachers and friends who have made it possible. I must thank the almighty for giving me the strength to keep moving ahead even during the tough times. I hope that with the education and training I have received, I will be able to give back to society.

Contents

List of Figures

Introduction

This thesis was carried out in CRHEA, a CNRS laboratory that specializes in growth of semiconductor materials. The work was carried out in the Flatlight team in CRHEA and also in collaboration with other research groups from Harvard University, USA and Chalmers University, Sweden. The aim of this thesis was to realize the potential of planar optical components called metasurface for classical and quantum optics applications. As the phase and polarization of a light wave can be locally controlled using metasurfaces, they render novel optical functionalities compared to conventional refractive components. A particular arrangement of metaunits results in a phase gradient along the surface of the metasurface. By controlling this gradient the outgoing wavevector can be controlled. This property is utilized extensively in this work considering dielectric metasurfaces. In this work, they are used in combination with refractive optical components known as hybrid components to design achromatic devices and mitigate lens aberrations. Also, novel optical components were designed for applications in single photon experiments. For each of these applications, electromagnetic simulations were carried out, Nanofabrication of metasurfaces were performed and thorough optical characterization was done. To discuss these works in detail, this thesis is divided into 4 chapters. First, the concept of metamaterial and metasurface are introduced by giving a general theoretical discussion and presenting the standard equations associated with them. Metasurfaces made of different materials are introduced and the mechanism by which abrupt phase and polarization can be achieved is discussed in detail. Some of the interesting applications are also presented in this chapter.

Second chapter describes the design of a hybrid optical component of prism and phase gradient metasurface combination to achieve dispersion-free devices. Metasurfaces are simulated, nanofabricated and are experimentally studied by utilizing Fourier space spectroscopy technique to measure small magnitudes of dispersion. An interesting application of achro-

matic beam compressor is also presented. The same idea is extended to lens-metasurface combination in the third chapter to correct lens aberrations. Detailed analytical calculations for chromatic and spherical aberration correction are presented. For experimental demonstration, large area metasurfaces of centimeter scale are fabricated by employing a recent technique. Detailed experimental characterization is carried out to study the aberrations both quantitatively and qualitatively. Interesting techniques of phase measurement, Point spread function measurement and Zernike analysis are demonstrated.

In the last chapter, a novel device called Dual phase gradient metasurface is discussed for quantum optics applications. It is designed to replace beam splitter in a standard Hong Ou Mandel experiment which demonstrates two-photon interference. It is shown that metasurfaces can be designed to have interesting functionalities owing to their flexibility. The nanofabrication and classical optics characterization for dual gradient metasurface are also carried out.

Chapter 1

Introduction to metasurfaces

Electromagnetic waves observed in nature have a wide range of wavelengths varying from picometres to few kilometers. Visible light is made up of a narrow bandwidth whose wavelength is of the order of hundreds of nanometers. One can find many components to manipulate light such as lenses for focusing, prisms for dispersion, polarizers for polarizing light, diffraction gratings etc. Motivation for coming up with such components in the first place is perhaps found in the nature such as dispersion in rainbow, polarization in certain natural crystals etc. Nature never seizes to amaze us. Certain butterfly species called Morpho butterflies are known to exhibit a phenomenon called as iridescence through which they exhibit different shades of blue color at different angles of view as shown in figure 1.1. Reason behind it is not the commonly found pigmented coloration but arrangements of micro and nano sized ridges in their wings in a periodic fashion which causes constructive interference of particular wavelengths[1]. These phenomena raised questions such as can these effects be mimicked in laboratory? Taking a step ahead, is it possible to engineer exotic photonic effects never seen in nature? Perhaps this gave rise to the field of Nano-photonics. The term for such engineered materials is the well known Metamaterials. The term explains itself that its functionality is not so much dependent on its constituent material but the arrangement of its smallest units.

Biomimicking has been for many years a successful technique in engineering new devices. Same ideas were also applied in the field of metamaterials. Taking a step ahead, in 2006, a revolutionary idea was proposed by John B Pendry that theoretically a Metamaterial could

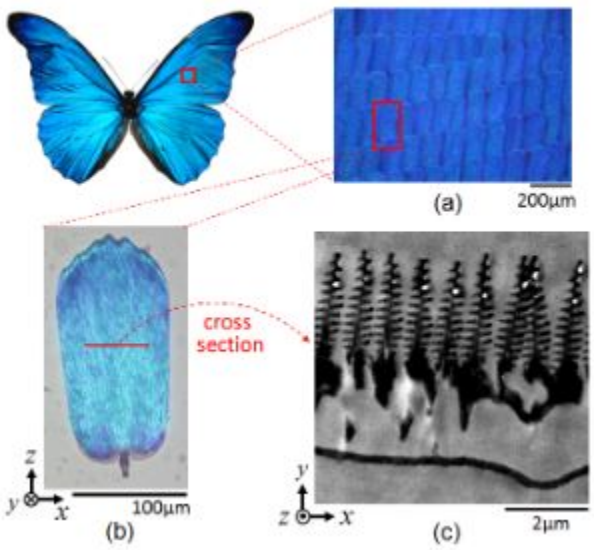

Figure 1.1: Nanostructures in Morpho butterfly wings [1]

be designed to work as an invisibility cloak[2]! This could be achieved by independently controlling permittivity and permeability, both the magnitude and sign, as a function of coordinates of the Metamaterial interface. This opened up a new field called Transformation Optics and Cloaking was demonstrated experimentally in the microwave region of spectrum. This work was a shining example of the extent of control one can have over light with metamaterials. Metamaterials provide the flexibility in design which is absent in the conventional bulk materials.

1.1 Metamaterials and metasurface

Metamaterials can be defined as a particular arrangement of antennas with size of unit cell comparable to the wavelength of incident electromagnetic waves to achieve a particular functionality. Electromagnetic metamaterials can be divided into 4 major categories namely Double Positive materials (DPS), Epsilon Negative materials (ENG), Mu Negative materials (MNG), Double Negative materials (DNG).

Double Negative materials, also called as left handed materials, are not found in nature but physically realizable with metamaterials. Thus it encompasses all ranges of epsilon and

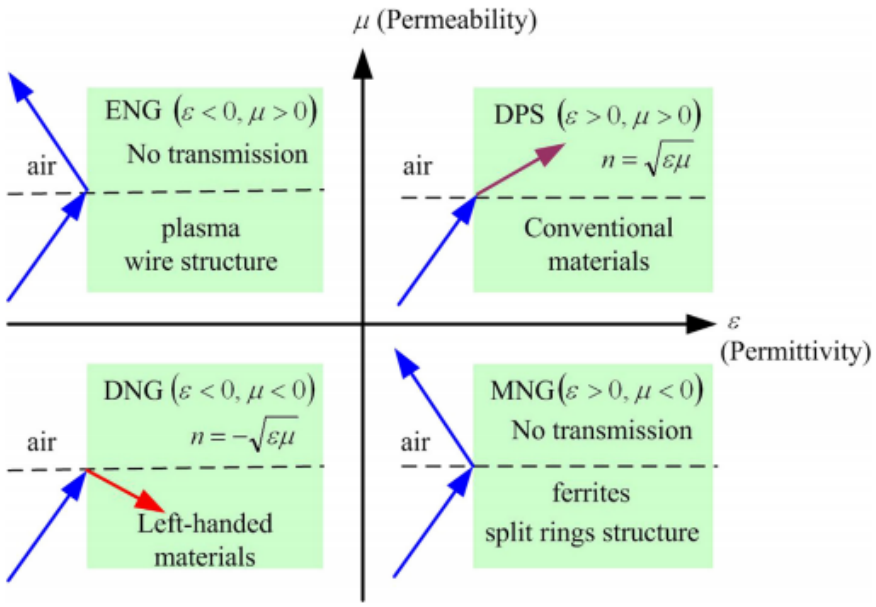

Figure 1.2: Types of Metamaterials that can be realized based on permittivity and permiability values [3]

mu which has enabled the realization of exotic phenomenon such as optical cloaking. By precisely controlling the shape, size, geometry and the arrangement of the antennas one can achieve complete control over the reflection, absorption, refraction of the electromagnetic wave. Other than for electromagnetic waves, metamaterials are also realized for sound waves called acoustic and elastic metamaterials. Hence metamaterials have become quite a general term. Starting from the seminal work by Kock to locally delay the phase of light using subwavelength metallic patches [4] followed by the work of Stork et al. and Farn to realize grating structures with a period small compared with the wavelength of light [5][6], the concept of high-contrast subwavelength (HCG) dielectric structures has led to the development of ultrathin optical components. Designing the diffracting properties at the subwavelength scale using spatially varying nanostructures, Lalanne et al. had reported blazed gratings with high efficiencies [7][8].

Metasurfaces are two dimensional counterparts of Metamaterials, generally made with sub wavelength scale optical components and perceived as sheet like material obeying specific boundary conditions. It can also be defined as an interface causing discontinuity in electromagnetic fields or imparting abrupt phase, polarization and amplitude shift in incident light. The equation to describe the trajectory of the incident light on metasurface is

called Generalized laws of refraction and reflection [9]. Generalized law of refraction (as shown in figure 1.3):

$$n_t Sin(\theta_t) - n_i Sin(\theta_i) = \frac{\lambda}{2\pi}\frac{d\phi}{dx} \tag{1.1}$$

Generalized law reflection

$$Sin(\theta_r) - Sin(\theta_i) = \frac{\lambda}{2\pi n_i}\frac{d\phi}{dx} \tag{1.2}$$

where n_i and n_t are the refractive indicies of incident medium and refracted medium respectively. Angles θ_i and θ_t are incident angle and refracted angle respectively, θ_r is the reflected angle, λ is the wavelength of incident light and $\frac{d\phi}{dx}$ is the phase gradient of the meatsurface along x-direction.

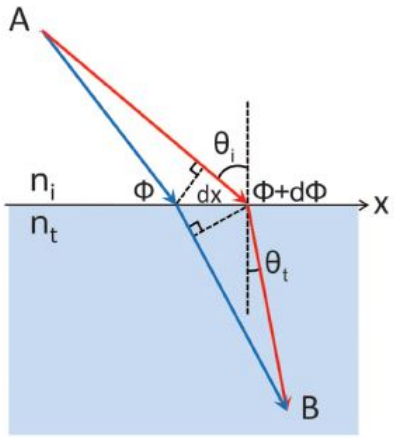

Figure 1.3: Generalized law of refraction [9]

This expression can be explained by Principle of stationary phase which is another form of Fermat's least action principle. It states that "The derivative of phase accumulated along the actual light path between point A and B is zero with respect to infinitesimal variation in the path". In other words, between points A and B, in the vicinity of actual path taken by light, phase variation is negligible. When this is compared to other paths between the same points, the phase variation is large even with a slight change in trajectory. One can also note that the equation is another form of linear momentum conservation in tangential direction [10]. It can be seen that the equation is exactly the Snell's law just with an added term of phase gradient of the metasurface. It is important to note that this treatment is justified for metasurface as long as they can be considered as sub wavelength thick surface.

If one achieves control over phasefront and polarization of the electromagnetic fields it is possible to achieve several optical functionalities such as lensing, vortex beams, holograms etc. Diffractive optical elements such as metasurface offer this control and great flexibility. Naturally, the question arises how this 'pixelwise' phase can be realized in a metasurface. In the next section, a theoretical framework stemming from electromagnetic theory is provided for subwavelength thick metasurface.

1.2 Metasurface Electromagnetic theory

The following is the macroscopic description of metasurface to characterize their optical properties in terms of permittivity ε and permeability μ [11]. By applying Maxwell's equations for the following boundary conditions for TE and TM polarizations, phase and amplitude of both reflected and transmitted rays are calculated. As shown in fig 1.4(b), metasurface is considered to be a slab of thickness 'h', permittivity ϵ_2 and permeability μ_2.

For both TE and TM polarization, the boundary conditions can be written as

$$r + 1 = t \quad ; \quad Y_1(1 - r) = Y_2 t,$$

where $r = E_{yr}/E_{yi}$ and $t = E_{yt}/E_{yi}$ for TE polarization. $r = E_{xr}/E_{xi}$ and $t = E_{xt}/E_{xi}$ for TM polarization. The horizontal admittance for each medium is given by $Y_i = H_{xi}/E_{yi}$ for TE polarization and $Y_i = H_{yi}/E_{xi}$ for TM polarization. Here 'i' represents index of layer. The following relations are obtained from Maxwell's equation.

$$\nabla X E = -\mu\mu_0 \frac{\partial H}{\partial t} \quad ; \quad \nabla X H = \epsilon\epsilon_0 \frac{\partial E}{\partial t}$$

Applying Maxwell's equation in boundary condition equation, we get,

$$Y_i = \begin{cases} \frac{k_{zi}}{\mu_i\mu_0\omega} = \frac{\sqrt{\epsilon_i\mu_i k_0^2 - k_x^2}}{\mu_i\mu_0\omega}, for TE \\ \frac{\epsilon_i\epsilon_0\omega}{k_{zi}} = \frac{\epsilon_i\epsilon_0\omega}{\sqrt{\epsilon_i\mu_i k_0^2 - k_x^2}}, for TM \end{cases} \tag{1.3}$$

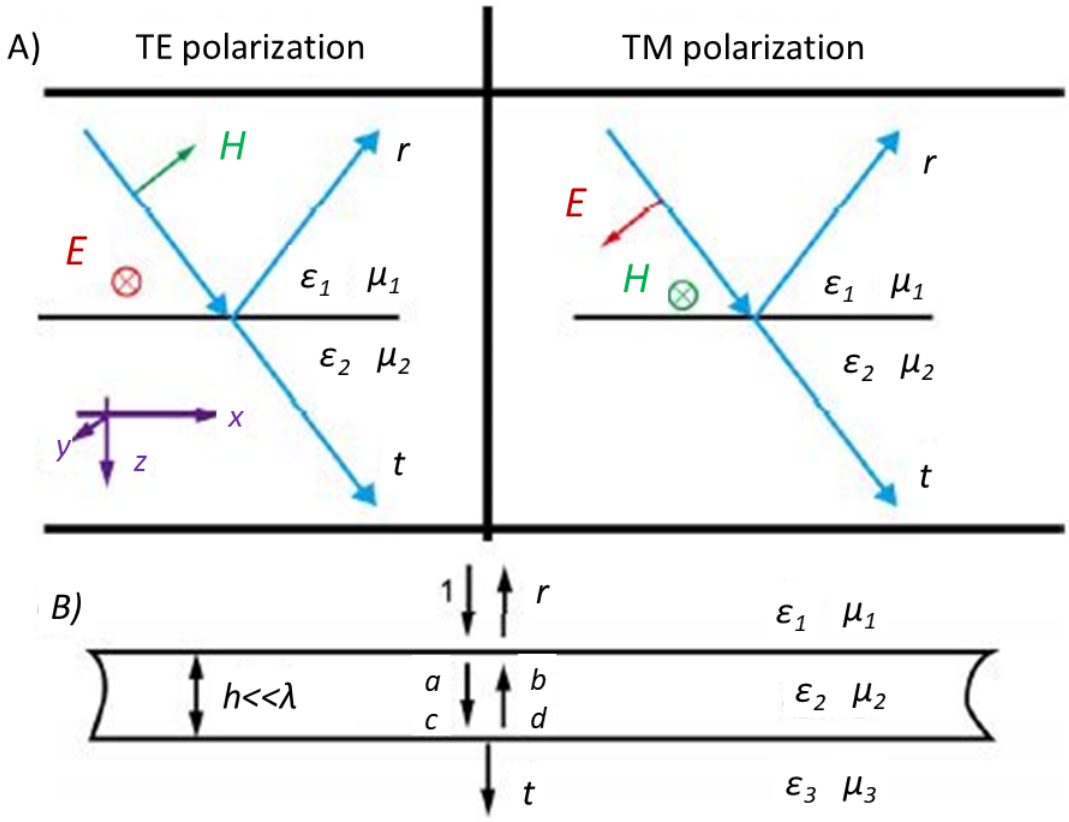

Figure 1.4: A) Electromagnetic theory of metasurface modelled as a thin slab for TE and TM polarization incidence B) Subwavelength thick slab is shown with permittivity ϵ_2 and permiability μ_2. The transmission and reflection co-efficients are indicated for each of the 3 media [11]

Here k_x is the horizontal wavevector as shown in figure 1.4. From boundary condition equation and admittance equation, the following relation for reflection and transmission co-efficient can be written.

$$t = \frac{2Y_1}{Y_1+Y_2} \ , \ r = \frac{Y_1-Y_2}{Y_1+Y_2}$$

They are very similar to the well known Fresnel equations, a minor difference is that they are expressed in terms of horizontal wavevectors. Consider a thin slab sandwiched between two different media as shown in figure 1.4 b). 1, 2, 3 represent 3 layers and a, b, c, d are the co-efficients for counter propagating waves in the slab. The boundary condition for the thin slab can be written as follows.

$$1 + r = a + b \ ; \ Y_1(1 - r) = Y_2(a - b)$$

$$c + d = t \ ; \ Y_2(c - d) = Y_3 t$$

The co-efficients by definition are given by

$$a = ce^{-ik_{z2}h}$$
$$b = de^{ik_{z2}h}$$

For extremely thin metasurface for $\mid k_z h \mid << 1$

$$a = c(1 - ik_{z2}h),$$
$$b = d(1 + ik_{z2}h)$$

From the above equation one can derive the following,

$$a + b = (c + d) + ik_{z2}h(c - d)$$
$$a - b = (c - d) - ik_{z2}h(c + d)$$

Considering that the middle layer has permittivity and/or permeability larger than the surrounding medium, we get $Y_2 >> Y_3$ and $c + d >> c - d$. This yields,

$$a + b = c + d$$
$$a - b = \frac{Y_3 t}{Y_2} - ik_{z2}ht$$

Inserting these equations into the boundary conditions equations, we get,

$$1 + r = t$$
$$Y_1(1 - r) = Y_3 t - iY_2 k_z ht$$

Comparing it with electric impedence boundary conditions,

$$1 + r = t$$
$$Y_1(1 - r) = Y_3 t + Y_e t$$

One can obtain the electric admittance for the slab as following,

$$Y_e = -iY_2 k_z ht = -i\frac{\epsilon_2 k_0^2 - k_z^2}{\mu_0 \omega} h \approx -i\omega\epsilon_0\epsilon_2 h$$

When the permiability μ is much larger than ϵ, $Y_2 << Y_3$ resulting in $c - d >> c + d$. This leads to the approximation,

$$a + b = c + d - ik_{z2}h(c - d)$$
$$a - b = c - d$$

This results in,

$$1 + r = t - ik_{z2}h\frac{Y_3}{Y_2}t$$
$$Y_1(1 - r) = Y_3 t$$

Comparing above equations with magnetic impedence boundary conditions,

$$1 + r = t + Z_m Y_3 t$$
$$Y_1(1 - r) = Y_3 t$$

Finally, the magnetic impedence can be obtained as follows,

$$Z_m = -i\frac{k_{z2}h}{Y_2} = -i\frac{\epsilon_2\mu_2 k_0^2 - k_z^2}{\epsilon_0\epsilon_2\omega} h \approx -i\omega\mu_0\mu_2 h$$

The obtained electric admittance and magnetic impedence equations are valid for homogenous materials. For metamaterials, effective imepedence can be obtained by applying boundary conditions in a similar way [12].

The most important feature of a metasurface is imparting abrupt phase. If the impedence of the metasurface is purely imaginary, meaning that the ohmic losses are absent, the phase can be changed arbitrarily. The reflection and transmission co-efficient when the magnetic impedence is taken into account become,

$$r = \frac{1}{2}\left(\frac{2Y_0 - Y_e}{2Y_0 + Y_e} + \frac{Z_m - 2Z_0}{Z_m + 2Z_0}\right)$$
$$t = \frac{1}{2}\left(\frac{2Y_0 - Y_e}{2Y_0 + Y_e} - \frac{Z_m - 2Z_0}{Z_m + 2Z_0}\right)$$

Here Y_0 and Z_0 are admittance and impedence respectively of the surrounding medium. By taking the argument function of the above complex co-efficients one can retrieve abrupt phase shift imparted by the metasurface.

It would be interesting to look in detail the phenomenon of abrupt phase and polarization change at antenna level. A few ways to achieve this is by utilizing Pancharatnam-Berry phase(PB phase) and Propagation phase which is discussed in subsequent sections. Even though the objective is to achieve abrupt phase and polarization, the approach to realize it is different with plasmonic and dielectric metasurfaces owing to the different material properties. Therefore, plasmonic and dielectric metasurfaces are discussed separately in the next section.

1.3 Plasmonic metasurface

One of the first ways to realize subwavelength thick metasurface was to use gold nanorods. As discussed in [9], plasmonic resonance of V shaped nanorods was exploited to achieve full phase range from 0 to 2π. Two modes of resonance 'Symmetric' and 'Antisymmetric' can be seen acting together. This gives the freedom over phase in 2 dimensions. By placing constantly incremented phase elements from 0 to 2π at equal distance from each other, beam deflector was realized. One can imagine that with control on phase and amplitude in 2 dimensional polarization plane, arbitrary wavefront is realizable, be it a lens, vortex beams or holograms.

In plasmonic antennas, the resonance in play is called Localized Surface Plasmon Resonance (LSPR). This can be mathematically described as a simple harmonic oscillator with a damping force and an external field imparting energy into the system [13]. Consider 'q' to be a charge on the surface of a plasmonic structure of mass 'm' located at position 'x (t)' at time t. One can model the Simple harmonic oscillator by assuming that the particle is attached to a spring with spring constant 'k' driven by a harmonic incident electric field with frequency 'ω'. The Ohmic losses lead to charges experiencing internal damping with damping co-efficient 'γ'. We obtain the following equation with this model,

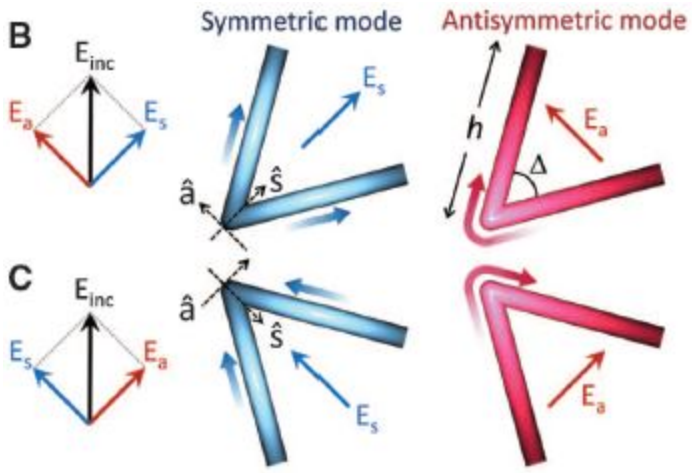

Figure 1.5: V shaped plasmonic antennas for metasurface [9]

$$\frac{d^2x}{dt^2} + \frac{\gamma}{m}\frac{dx}{dt} + \frac{k}{m}x = \frac{q}{m}E_0 e^{i\omega t} + \frac{2q^2}{3mc^3}\frac{d^3x}{dt^3} \tag{1.4}$$

The $\frac{dx}{dt}$ term is the damping force, $\frac{d^3x}{dt^3}$ is the radiation reaction force which describes the recoil that the charge experiences when it emits radiation. From the above treatment, it can be realized that the maximum phase shift that can be obtained from a plasmonic antenna is π. In other words, for the construction of a metasurface, phase coverage of 0 to 2π in antennas is required but plasmonic structures offer only 0 to π phase range which is a limitation. Moreover poor forward scattering and high damping losses in visible region decreases the efficiency of the final device. The above plasmonic metasurface was designed using hybrid phase which will be discussed in the next section.

1.4 Dielectric metasurface: Huygen's metasurface

Realizing that plasmonic materials are not the ideal candidates for efficient metasurfaces, the focus was shifted towards dielectric antennas. Making use of dielectric resonances, Huygen's metasurface was proposed. Dielectric nanoparticles with size comparable to the incident wavelength of light behave as Mie scatterers. Following the exact Mie calculations it is possible to calculate both internal and radiating fields. Analytical expression of radiating fields can be compared to experimental data and contribution of each mode can be extracted. This

treatment is particularly useful in ascertaining the mechanism of transmission or reflection at a particular wavelength.

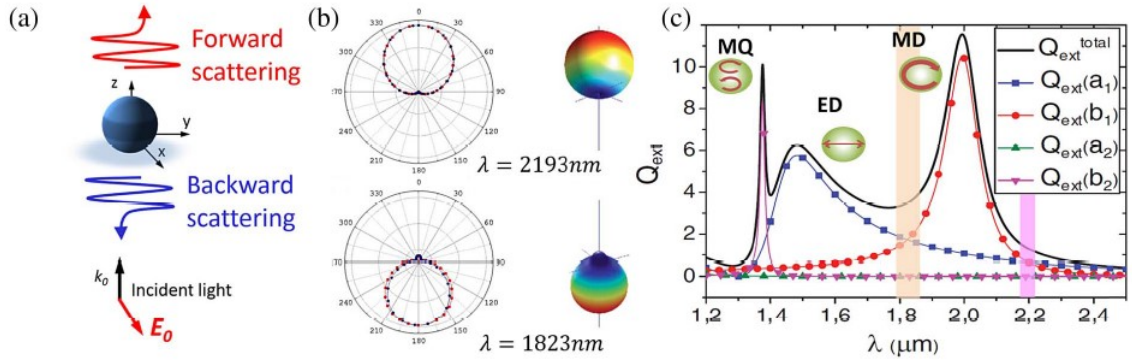

Figure 1.6: Huygens metasurface using first Kerker's condition. In (c), red line corresponds to magnetic dipole contribution and blue line to electric dipole contribution. [14] [15]

In a Mie resonator typically the first resonance that occurs is the magnetic dipole mode approximately when the effective wavelength is of the order of particle diameter. This is followed by the electric dipole mode. Given that the particle's size is small and is of the order of incident wavelength, the particle can be treated as a dipole where only dipolar modes contribute to the scattered field. The same principle can be extrapolated to cylindrical pillars or rectangular resonators to use them as building blocks of a metasurface. The idea here is to utilize high contrast grating structures which have high refractive index compared to the substrate and surrounding medium to construct metasurfaces. To achieve maximum transmission/reflection, Kerker's first condition is utilized. This condition states that when relative permittivity of the particle is equal to relative permeability, zero backscattering and maximum forward scattering can be observed. This is because the electric and magnetic dipole coefficients in the Mie scattering expansion become equal in this condition which leads to destructive interference in the backward direction. Similarly, when electric and magnetic dipole resonances overlap out of phase, constructive interference occurs in backward direction. The illustration of the Kerker condition for 240 nm Germanium sphere can be seen in figure 1.6 [14]. It can be seen that at wavelengths when electric and magnetic dipole contributions are equal, zero backward (Kerker's first condition) or forward scattering (Kerker's second condition) is achieved as as shown in figure 1.6 (b) and (c).

Finally using this property of impedance matching, Huygen's metasurface can be designed which will have spatially varying phase delay and minimum backward scattering.

1.5 Types of Dielectric metasurface

Approaches discussed so far to construct metasurface are based on resonances of the nanoantennas. More convenient non-resonant mechanisms are discussed in the present section. As in this thesis dielectric metasurfaces are extensively used, different approaches to realize abrupt phase and polarization with dielectric metasurface is discussed in detail here.

1.5.1 As waveguides

One way to achieve full phase coverage using dielectric nanopillars is to employ the wave guiding property of tall nanopillars of high refractive index materials. The height of the pillars are not necessarily sub-wavelength but as long as the incident light is close to normal incidence, generalized law of reflection and refraction can still be applied. For oblique incidence, the polarization component along the height of the pillar might excite other modes in them which will affect transmission and reflection of the metasurface. The pillar height of a particular material is chosen such that it can give full phase coverage of 0 to 2π by changing nanopillar diameter. The lower limit for the diameter is set by the fabrication limitation and the upper limit is decided by the length of each period for achieving a particular functionality. To have a better understanding of the mechanism, phase contribution just by waveguiding effect was studied in [16].

$$\phi_{wg} = \frac{2\pi}{\lambda} n_{eff} H \tag{1.5}$$

where n_{eff} is the fundamental mode of the waveguide and 'H' is the height of the nanopillar.

Following this model, the phase shift as a function of diameter of nanopillar was plotted and compared with FDTD simulation for the same on a glass substrate as shown in figure 1.7. It can be seen that they agree with each other with a small error in phase. Larger the diameter better the field confinement of the fundamental mode hence lower the deviation from FDTD plot. Also the field confinement along the propagation direction is neglected which occurs due to the standing wave formation by reflections from opposite facets of nanopillars. Hence the claim that waveguiding is the dominant mechanism for phase shift generation is verified.

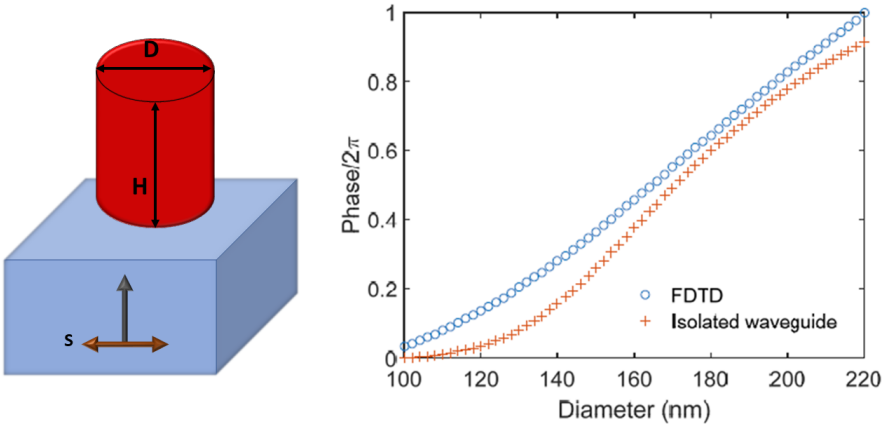

Figure 1.7: Waveguiding phenomenon in nanopillars. Left: TiO_2 nanopillar of height H=600nm on SiO_2 substrate and source of S of wavelength 532 nm. Right: Comparison of Phase shift vs diameter of pillar obtained from FDTD simulation and that calculated from HE_{11} fundamental mode at wavelength of 532 nm. [16]

In [16] , FDTD simulation for phase map with varying nanopillar diameter for different incident wavelength is studied. Similarly, one can also compute transmission map to identify the parameter space of high transmission. To achieve desired functionality of a device by constructing spatially varying meta-units, appropriate phase element can be picked from the map to construct a metasurface. In the same work, it was demonstrated how a Metalens can be designed using the same technique. Consider 'r' to be the radial distance of a point on the metasurface from its center. If 'f' is the focal distance of the metalens anf point f as the focus, then the distance between focal point and the metasurface co-ordinate is $\sqrt{r^2+f^2}$. In the case without metasurface, the wavefront would have travelled distance 'f' to reach point F. Therefore the shift in the wave the metasurface has to impart is $\sqrt{r^2+f^2}$–f . Denoting metasurface plane as x-y plane r co-ordinate can be written as (x,y). Calculating the corresponding phase shift for design wavelength λ_d considering the fact that nanopillars impart a phase delay we get,

$$\Phi_t(x,y) = 2\pi - \frac{2\pi}{\lambda_d}(\sqrt{x^2+y^2+f^2} - f) \tag{1.6}$$

The diameter of the nanopillar corresponding to a particular phase can be picked from

the phase map and arranged in an array to realize a metalens. This proves that one can have tremendous control over propagation phasefront with a proper design of metasurface. However, the phase delay imparted by the pillars is quite sensitive to its dimension. And it is difficult to have a complete control over the nanopillar dimensions owing to the inaccuracies in nanofabrication. Therefore to obtain an accurate phase profile one needs to take into account the difference between the actual and expected size of the nanopillar which is a limitation of this approach.

1.5.2 Pancharatnam Berry phase metasurface

Another interesting mechanism by which abrupt phase shift can be realized in a metasurface is by utilizing Pancharatnam Berry phase (PB) metasurface. Before discussing about the PB metasurface it is crucial to understand the origin of the PB phase which is a Geometric phase. Generally, geometric phase can be defined as the phase shift resulting from the geometric properties of the parameter space of the Hamiltonian when the system is subjected to cyclic, adiabatic process. [17]. When at least two parameters are involved to characterize the system and both of them are varied simultaneously over the course of a cycle then this phase can be observed. In optics, when polarization state of light is taken along a closed circle in the Poincaré sphere, light acquires geometric phase along with dynamic phase because of its path length [18].

S. Pancharatnam, in 1956, had theorized this effect and M. Berry had given a general theory including quantum systems in 1984, hence the name Pancharatnam-Berry phase. It is given by negative of half the solid angle subtended by the closed contour traced on the Poincaré sphere. It is best realized using a half wave plate. Half Wave Plate (HWP) is a birefringent material which induces a relative phase retardation of half the wavelength along its slow axis compared to the fast axis. When a linearly polarized beam is incident on the waveplate, the resulting beam is linearly polarized with its polarization axis making 2θ with respect to the incident polarization direction. Here 'θ' is the angle between incident polarization axis and the fast axis of HWP. In the case of an incident circularly polarized beam, after passing through HWP it gets converted into the opposite handed circular polarized light. Consider that Right circular polarized (RCP) light is incident and irrespective of rotation angle of HWP, LCP is obtained as output. But depending on θ the light starting from RCP can take different trajectory on Poincare sphere to reach LCP as shown in figure

1.8 a). Therefore the beam acquires a global phase of 2θ which is precisely the PB phase. It has to be noted that the PB phase can be controlled by changing the rotation angle of HWP.

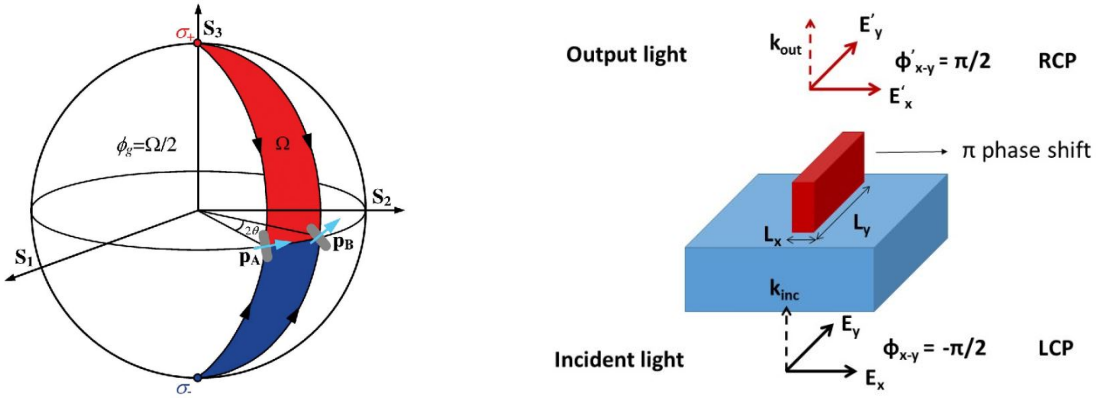

(a) (b)

Figure 1.8: Pancharatnam berry metasurface description using Poincaré sphere[19]

Similar effects can be realized using a metasurface. As described in the previous section that desired phase can be obtained using dielectric nanopillars utilizing their waveguiding property. Extending the same idea, in asymmetric (rectangular or elliptical cross section) nanopillars it is possible to have 2 modes simultaneously each along the length and the width of the pillar. The length and width are chosen such that the path length difference between the 2 modes is $\frac{\lambda}{2}$ or phase difference of π imitating birefringent crystals as shown in figure 1.8 b). It also has to be made sure that the transmission amplitudes are same for both the modes for the output to be circularly polarized.

Now, since we have a HWP equivalent at nanoscale, it should be possible to obtain different PB phase by rotating nanopillars along the vertical axis (Nanopillar height axis). Therefore α rotation of nanopillar will result in 2α PB phase added to the output beam as shown in the figure 1.9.

To control phase at nanoscale using metasurface, PB phase is a very reliable technique. One of the advantages it offers is that the 'signal' with PB phase information has opposite circular polarization compared to the input polarization. Therefore, it is convenient to filter out the incident light and extract the signal using a set of Half wave plate and Quarter wave plate. Another obvious benefit is that the phase can be precisely controlled by controlling the rotation of pillars. Whereas in other methods, one has to rely on effective refractive

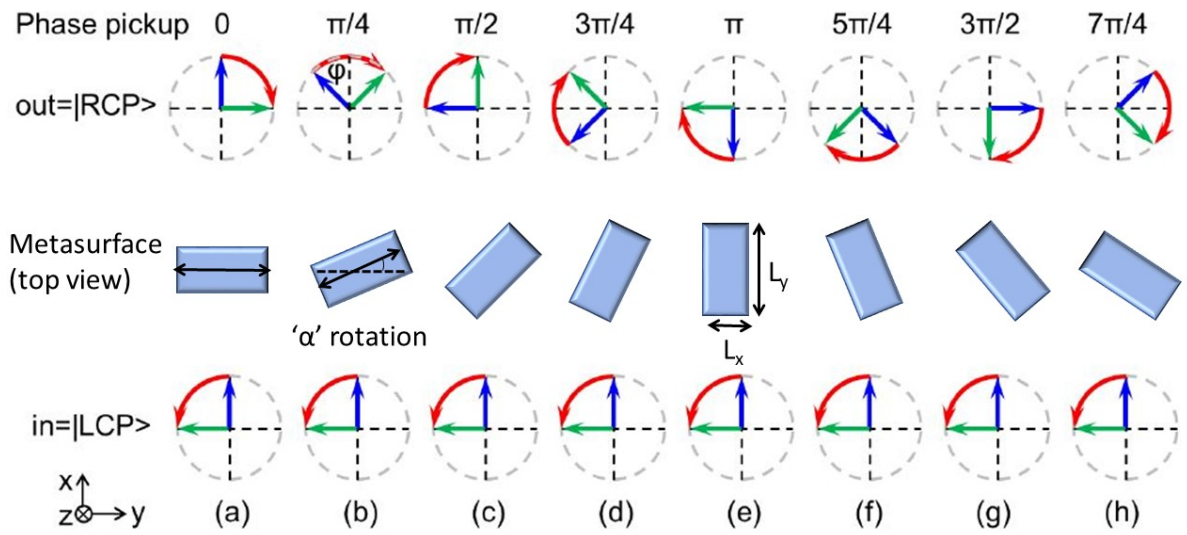

Figure 1.9: PB phase generation by rotation of nanopillars [20]

index of the pillars which is strongly dependent on the dimension of the pillars.

Jones matrix treatment

A birefringent nanopillar is represented in Jones matrix as follows assuming that pillar cross section is in x-y plane and transmission along x and y are equal. ϕ_x and ϕ_y are phase retardation along x and y axis because of birefringence. [21][22]

$$J_0 = \begin{bmatrix} e^{i\phi_x} & 1 \\ 1 & e^{i\phi_y} \end{bmatrix} \tag{1.7}$$

Applying optical rotation matrix to denote the pillar rotation along its height axis by α. New transfer matrix can be calculated as follows.

$$M = R(-\alpha) \begin{bmatrix} e^{i\phi_x} & 0 \\ 0 & e^{i\phi_y} \end{bmatrix} R(\alpha) \tag{1.8}$$

Rotation matrix R for α rotation can be written as

$$R(\alpha) = \begin{bmatrix} cos(\alpha) & sin(\alpha) \\ -sin(\alpha) & cos(\alpha) \end{bmatrix} \tag{1.9}$$

Assuming that the incident polarization is LCP, the transfer matrix can be applied on E_{LCP}. Few steps of simplification lead to the final transmission expression.

$$E_T = \hat{M}.E_{LCP}, E_T = \frac{(e^{i\phi_x} + e^{i\phi_y})}{2}.E_{LCP} + \frac{(e^{i\phi_x} - e^{i\phi_y})}{2}.e^{im2\alpha}.E_{RCP} \tag{1.10}$$

In the case of $\delta\phi_x - \delta\phi_y = \pi$, it can be seen that LCP input is completely converted to RCP. By varying the phase retardation difference between x and y, one can tune the ratio of transmission between 0 order and 1st order. The term $e^{im2\alpha}$ associated with the converted circular polarization represents PB phase. Therefore α rotation of the pillars results in 2α PB phase. Implying that rotation of nanopillars from 0 to π yields full phase coverage of 0 to 2π! A general expression for output fields can be written as follows [23]

$$|E_{out}\rangle = \sqrt{\eta_E}\,|E_{in}\rangle + \sqrt{\eta_R}e^{i2\alpha(x,y)}\,|R\rangle + \sqrt{\eta_L}e^{-i2\alpha(x,y)}\,|L\rangle \tag{1.11}$$

where

$$\eta_E = |\frac{1}{2}(t_x + t_y e^{i\phi})|^2; \eta_R = |\frac{1}{2}(t_x - t_y e^{i\phi})\,\langle E_{in}\,|L\rangle|^2\,; \eta_L = |\frac{1}{2}(t_x - t_y e^{i\phi})\,\langle E_{in}\,|R\rangle|^2 \tag{1.12}$$

Here t_x and t_y are the transmission along x and y axis. It can be noticed that there is quite a lot of freedom to tune the output polarization and phase which is not offered by other approaches of phase generation. This effect can also be realized using plasmonic structures. But in this section the focus is only on dielectric metasurfaces as they are extensively used

in this thesis work. The following is an example of a PB phase based beamsplitter [21] Here in one period, the pillars are rotated from 0 to π with the intervals of $\pi/6$ placed at equal distance from each other. This is an example of constant phase gradient which works as a beam deflector. The deflection depends on the length of the period given by generalized law of refraction. Incident circular polarization is almost completely converted to opposite circular polarization deflecting at an angle with respect to the zero order.

The metasurface will show dispersion when the incident light is away from the design wavelength. The phase retardation difference along x and y axis may not be π in that case. In order to achieve PB phase in visible region, Titanium dioxide (TiO_2) or Gallium Nitride (GaN) are popular materials. They are high refractive index materials and birefringence with π phase difference can be achieved with reasonable height of nanopillars. Also they exhibit quite good transmission in visible region. Exactly similar to above, metasurfaces which work in reflection mode can also be designed employing generalized law of reflection. There is also possibility of realizing hybrid phase by utilizing both PB phase and propagation phase (from waveguiding) which offers an extra dimension of freedom. Similarly, in [22], hybrid of PB phase and resonant phase of coupled metallic nanorods is used to realized braodband achromatic metasurface.

1.6 Applications

With the control on phase and polarization of a metaunit one can realize various functionalities such as lens, beam splitter etc by imparting appropriate phase delay at each point on metasurface. Apart from these, two unique applications that can be realized from abrupt phase and polarization of metasurface are generation of vortex beams and holograms. Both of them are discussed in this section.

1.6.1 Spin Orbit coupling

One of the major advantages of Pancharatnam Berry phase structures is that it is possible to have control over phase and polarization of the outgoing light simultaneously. This brings us to the discussion of optical vortices generation using PB phase metasurface. Angular

momentum can be classified into two types broadly, Orbital Angular Momentum (OAM) and Spin Angular Momentum (SAM). OAM further can be divided into External and Internal OAM. External OAM is given by cross product of displacement vector of a particle from a point of reference and its momentum vector. Internal OAM is defined for particles in circular orbit with respect to the center of the orbit. SAM refers to the intrinsic spin of the particle spinning along the axis passing through its center. Similar to the conservation of linear momentum, it is also required that in a closed system, Angular momentum is always conserved.

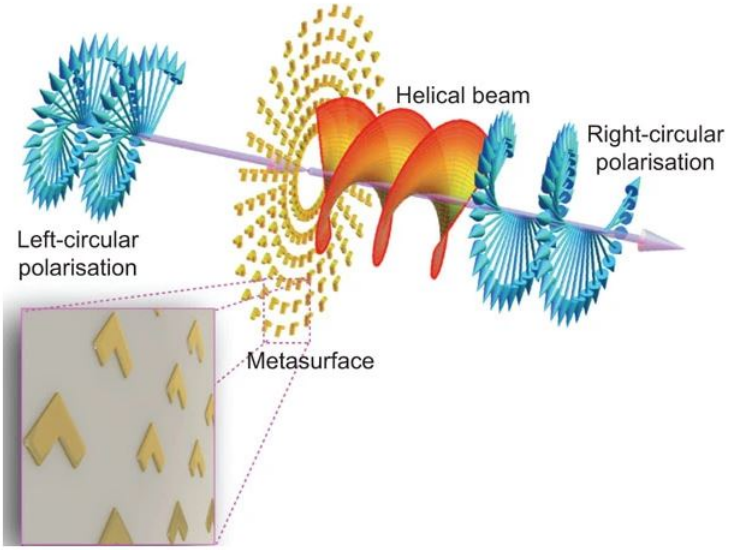

Figure 1.10: Spin Orbit coupling and Vortex beams generation using metasurface [24]

In the case of PB phase metasurface, when the incident circular polarization is converted into opposite circular polarization, there is an abrupt change in angular momentum of the system. Assuming that the incoming light is RCP, it has SAM of $\hbar$ in the propagation direction. After transmitting through PB metasurface, polarization converted LCP light will have $-\hbar$ SAM along the same direction. Consider a particular case that nanoantennas are arranged in a cylindrically symmetrical fashion along the metasurface center as shown in figure 1.10. Because the metasurface is rotationally invariant, it doesn't exchange angular momentum with the metasurface. But since the difference between SAM outgoing and incoming is $2\hbar$, conservation of angular momentum dictates that this should appear as OAM. Here V shaped plasmonic antennas are utilized to demonstrate this phenomenon. This would produce OAM of $l = \pm 2(q = 1)$. If higher order OAM is required, additional angular

momentum has to be provided by appropriate rotation of nanoantennas. The general relation for rotation angle of antennas is given by $\alpha = q\phi + \alpha_0$. The azimuthal angle with respect to origin is given by ϕ, 'q' is the order of OAM required and α_0 is the rotation of pillar at $\phi = 0$.[25]

As explained before, PB phase term $e^{im2\alpha}$ appears with the cross polarization term. Now by rotating azimuthally rotating antennas according to the above equation, creates azimuthally varying phase which results in vortex beams [26].

1.6.2 Holograms

A hologram is an encoding of light field as an interference pattern to reconstruct full wave information of a certain object. The conventional techniques have drawbacks such as large pixel size, limited bandwidth, small field of view which limits their application for 3-dimensional holograms, large data encoding etc. Metasurface based holograms offer many advantages such as low noise, high precision of reconstructed images as phase and amplitude can be encoded in ultra thin holograms [27]. Reduced pixel size also significantly improves holographic images and eliminate undesirable diffraction orders. In order to realize a hologram using a metasurface, the steps shown in figure 1.11 are usually followed. First, mathematically formulating the object of hologram which is followed by numerically calculating the complex amplitude and phase of each point on the holographic plane. This phase and amplitude information is encoded in the metasurface which translates to size and shape of nanoantennas at each point on metasurface. This is followed by nanofabricating the corresponding metasurface and optically reconstructing the holographic image with an appropriate optical setup.

The relation between scattered fields Γ over an arbitrary surface with co ordinates ξ, η, ζ and an object wave A_{obj} can be described by a wave propagation integral over the object surface S_{obj} as

$$\Gamma(\xi, \eta, \zeta) = \iiint_{S_{obj}} A_{obj}(x, y, z) T(x, y, z; \xi, \eta, \zeta) dx dy dz \tag{1.13}$$

The wave propagation integral kernel $T(x, y, z; \xi, \eta, \zeta)$ depends on object's spatial dispo-

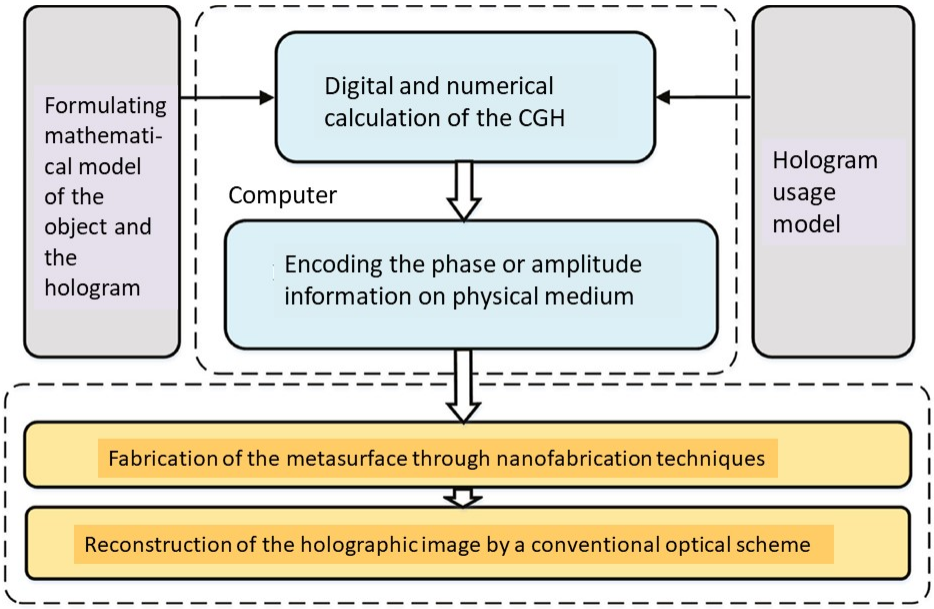

Figure 1.11: Method for Hologram generation [27]

sition and the observation surface. Object reconstruction can be calculated by back propagation integral over the observation surface as

$$A'_{obj}(x,y,z) = \iiint_{S_{obj}} \Gamma(\xi,\eta,\zeta)T(\xi,\eta,\zeta;x,y,z)d\xi d\eta d\zeta \tag{1.14}$$

Thus the hologram construction requires computation of Γ from the first equation through A_{obj} from the object description and illumination conditions. From the computed $\Gamma(\xi,\eta,\zeta)$, the information is encoded on a metasurface which enables the reconstruction of A_{obj} according to the above equation. At the same time angular co-ordinates of the reconstructed image is given by the following relation

$$\theta_x = \frac{2\pi\lambda}{\Delta\xi}; \theta_y = \frac{2\pi\lambda}{\Delta\eta} \tag{1.15}$$

where $\Delta\xi$ and $\Delta\eta$ represent period of the lattice in the orthogonal directions. Holography

realization using metasurface can be classified into 3 categories: Phase only, Amplitude only, Phase-Amplitude combined holography.

It is popular to realize phase only hologram using an iterative or point source algorithm to optimize the uniformity of intensity. By neglecting the amplitude information one can calculate phase only Computer Generated Holograms (CGH). In [28] a 3D phase only hologram is realized using PB metasurface. Each gold nanorod acts as a pixel and accurate phase control is possible because of geometric nature of phase generation. In fig 2, Hologram operating for large bandwidth is designed with TiO_2 nanopillars is shown [29]. Subwavelength pixel size enables the realization of holograms with high resolution and free of multiple order diffraction.

Enormous space-bandwidth available in metasurface is a huge motivation for multiplexing in holography for maximizing information storage. Various different types of multiplexing is possible with PB metasurface such as Color multiplexing, Polarization multiplexing, OAM multiplexing etc. A common strategy is to use a sub array of antennas as a pixel of the hologram metasurface. For color multiplexing, one of the methods used is to calculate the dimensions of the antenna such that the polarization conversion is maximized for a particular range of wavelengths. This was realized using Silicon nanopillars as shown in the paper [30]. To encode the hologram into phase information, Gerchberg-Saxton (GS) algorithm was utilized.

1.7 Conclusion

Metasurfaces seem to be extremely promising in the field of nanophotonics especially to engineer the phasefront of light. They provide unprecedented control over phase, polarization and intensity of the outgoing light.In this work, I have utilized phase gradient metasurfaces for various applications such as for mitigating prism dispersion, correcting lens aberrations and also for Quantum optics applications. The concepts of propogation phase and Pancharatnam-Berry phase discussed in this section are extensively used to design these metasurfaces.

Because of tremendous flexibility metasurfaces offer, I would like to call it the 'Magic surface' as things never imagined before in Optics are achievable in miniaturized form us-

ing metasurfaces. This thesis is about my journey of mastering this art of magic called Metasurface!

Bibliography

[1] Naoki Okada, Dong Zhu, Dongsheng Cai, James B Cole, Makoto Kambe, and Shuichi Kinoshita. Rendering Morpho butterflies based on high accuracy nano-optical simulation. *Journal of Optics*, 42(1):25–36, 2013.

[2] J B Pendry, D Schurig, and D R Smith. Controlling Electromagnetic Fields. *Science*, 312(5781):1780–1782, 2006.

[3] Zhongsheng Chen, Bin Guo, Yongmin Yang, and Congcong Cheng. Metamaterials-based enhanced energy harvesting: A review. *Physica B: Condensed Matter*, 438:1–8, 2014.

[4] Winston E Kock. Metallic Delay Lenses. *Bell System Technical Journal*, 27(1):58–82, 1948.

[5] W Stork, N Streibl, H Haidner, and P Kipfer. Artificial distributed-index media fabricated by zero-order gratings. *Opt. Lett.*, 16(24):1921–1923, dec 1991.

[6] Michael W Farn. Binary gratings with increased efficiency. *Appl. Opt.*, 31(22):4453–4458, aug 1992.

[7] Philippe Lalanne, Simion Astilean, Pierre Chavel, Edmond Cambril, and Huguette Launois. Blazed binary subwavelength gratings with efficiencies larger than those of conventional échelette gratings. *Opt. Lett.*, 23(14):1081–1083, jul 1998.

[8] Philippe Lalanne. Waveguiding in blazed-binary diffractive elements. *J. Opt. Soc. Am. A*, 16(10):2517–2520, oct 1999.

[9] Nanfang Yu, Patrice Genevet, Mikhail a Kats, Francesco Aieta, Jean-Philippe Tetienne, Federico Capasso, and Zeno Gaburro. Light Propagation with Phase Discontinuities Reflection and Refraction. *Science*, 334(October):333–337, 2011.

[10] Stéphane Larouche and David R Smith. Reconciliation of generalized refraction with diffraction theory. *Opt. Lett.*, 37(12):2391–2393, jun 2012.

[11] Xian Gang Luo. Principles of electromagnetic waves in metasurfaces. *Science China: Physics, Mechanics and Astronomy*, 58(9):1–18, 2015.

[12] Mingbo Pu, Chenggang Hu, Cheng Huang, Changtao Wang, Zeyu Zhao, Yanqin Wang, and Xiangang Luo. Investigation of Fano resonance in planar metamaterial with perturbed periodicity. *Opt. Express*, 21(1):992–1001, jan 2013.

[13] Mikhail A Kats, Nanfang Yu, Patrice Genevet, Zeno Gaburro, and Federico Capasso. Effect of radiation damping on the spectral response of plasmonic components. *Opt. Express*, 19(22):21748–21753, oct 2011.

[14] Raquel Gomez-Medina, Braulio Garcia-Camara, Irene Suarez-Lacalle, Francisco González, Fernando Moreno, Manuel Nieto-Vesperinas, and Juan Jose Saenz. Electric and magnetic dipolar response of germanium nanospheres: interference effects, scattering anisotropy, and optical forces. *Journal of Nanophotonics*, 5(1):1–10, jan 2011.

[15] Patrice Genevet, Federico Capasso, Francesco Aieta, Mohammadreza Khorasaninejad, and Robert Devlin. Recent advances in planar optics: from plasmonic to dielectric metasurfaces. *Optica*, 4(1):139, 2017.

[16] M. Khorasaninejad, A. Y. Zhu, C. Roques-Carmes, W. T. Chen, J. Oh, I. Mishra, R. C. Devlin, and F. Capasso. Polarization-Insensitive Metalenses at Visible Wavelengths. *Nano Letters*, 16(11):7229–7234, 2016.

[17] J C Solem and L C Biedenharn. Understanding geometrical phases in quantum mechanics: An elementary example. *Foundations of Physics*, 23(2):185–195, 1993.

[18] Julio C. Gutiérrez-Vega. Pancharatnam–Berry phase of optical systems. *Optics Letters*, 36(7):1143, 2011.

[19] Nir Shitrit, Shai Maayani, Dekel Veksler, Vladimir Kleiner, and Erez Hasman. Rashba-type plasmonic metasurface. *Optics Letters*, 38(21):4358–4361, 2013.

[20] Dianmin Lin, Pengyu Fan, Erez Hasman, and Mark L. Brongersma. Dielectric gradient metasurface optical elements. *Science*, 345(6194):298–302, 2014.

[21] Mohammadreza Khorasaninejad and Kenneth B Crozier. Silicon nanofin grating as a miniature chirality-distinguishing beam-splitter. *Nature Communications*, 5(1):5386, 2014.

[22] Daopeng Wang, Qingbin Fan, Jiaxing Wang, Zijie Zhang, Yuzhang Liang, and Ting Xu. All-dielectric metasurface beam deflector at the visible frequencies. *Guangdian Gongcheng/Opto-Electronic Engineering*, 44(1):103–107, 2017.

[23] Erez Hasman, Vladimir Kleiner, Gabriel Biener, and Avi Niv. Polarization dependent focusing lens by use of quantized Pancharatnam–Berry phase diffractive optics. *Applied Physics Letters*, 82(3):328–330, jan 2003.

[24] Ebrahim Karimi, Sebastian A. Schulz, Israel De Leon, Hammam Qassim, Jeremy Upham, and Robert W. Boyd. Generating optical orbital angular momentum at visible wavelengths using a plasmonic metasurface. *Light: Science and Applications*, 3(November), 2014.

[25] Robert Charles Devlin, Antonio Ambrosio, Daniel Wintz, Stefano Luigi Oscurato, Alexander Yutong Zhu, Mohammadreza Khorasaninejad, Jaewon Oh, Pasqualino Maddalena, and Federico Capasso. Spin-to-orbital angular momentum conversion in dielectric metasurfaces: erratum. *Optics Express*, 25(4):4239, 2017.

[26] Ming Kang, Jing Chen, Xi-Lin Wang, and Hui-Tian Wang. Twisted vector field from an inhomogeneous and anisotropic metamaterial. *Journal of the Optical Society of America B*, 29(4):572, 2012.

[27] Lingling Huang, Shuang Zhang, and Thomas Zentgraf. Metasurface holography: From fundamentals to applications. *Nanophotonics*, 7(6):1169–1190, 2018.

[28] Lingling Huang, Xianzhong Chen, Holger Mühlenbernd, Hao Zhang, Shumei Chen, Benfeng Bai, Qiaofeng Tan, Guofan Jin, Kok Wai Cheah, Cheng Wei Qiu, Jensen Li, Thomas Zentgraf, and Shuang Zhang. Three-dimensional optical holography using a plasmonic metasurface. *Nature Communications*, 4(May):1–8, 2013.

[29] Robert C Devlin, Mohammadreza Khorasaninejad, Wei Ting Chen, Jaewon Oh, and Federico Capasso. Broadband high-efficiency dielectric metasurfaces for the visible spectrum. *Proceedings of the National Academy of Sciences*, 113(38):10473 LP – 10478, sep 2016.

[30] Bo Wang, Fengliang Dong, Qi-Tong Li, Dong Yang, Chengwei Sun, Jianjun Chen, Zhiwei Song, Lihua Xu, Weiguo Chu, Yun-Feng Xiao, Qihuang Gong, and Yan Li. Visible-Frequency Dielectric Metasurfaces for Multiwavelength Achromatic and Highly Dispersive Holograms. *Nano Letters*, 16(8):5235–5240, aug 2016.

Chapter 2

Prism dispersion compensation

Dispersion is quite a general term used in the field of Optics, Condensed matter physics, Signal processing. General definition is given by 'dependence of phase velocity of a wave on its frequency'. But in Optics, material dispersion is defined as variation of refractive index of a medium as a function of wavelength of the light passing through it. To get a general picture of the refractive index dependence on the frequency of incident light, Lorentz oscillator model for a dielectric material is discussed as follows. It considers classical light matter interaction to study the frequency dependent polarization in the material.

This model, as discussed in [1], considers electrons in the dielectric material to be bound to the nucleus by a spring like force which has a natural frequency of ω_0. Assuming that there is also a damping force in action, the relations for permittivity and complex refractive index as a function of incident light frequency ω can be obtained as shown in figure 2.1. The behavior of the material across the spectrum is divided into different regions as T, A, R which stands for Transmission, Absorption, Reflection respectively. One can notice that in the transmission region, real part of refractive index is always increasing as a function of frequency which is termed as the normal dispersion. Whereas the anomalous dispersion (opposite trend) can be seen in the Absorption and the Reflection region, when ω is around the resonant frequency. Therefore, it is observed that the materials which have their transmission band in the visible region, such as different types of glasses, show normal dispersion. For materials with normal dispersion and $\kappa = 0$, Cauchy proposed an empirical relation for refractive index as a function of wavelength which is popularly known as Cauchy's equation.

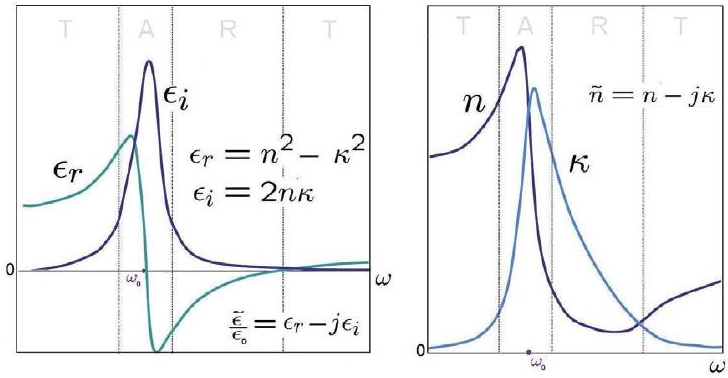

Figure 2.1: Lorentzian model to describe susceptibilty and refractive index as a function of frequency of light [1]

$$n(\lambda) = A + \frac{B}{\lambda^2} + \frac{C}{\lambda^4} + ... \tag{2.1}$$

A, B, C are called as Cauchy's coefficients and λ is the vacuum wavelength. Major drawbacks of this model is that it is not a general relation as it is applicable to only a particular region of spectrum. And Cauchy's coefficients have no physical meaning as it is an empirical equation. Even though there are other quite accurate models for refractive index, simplicity of Cauchy's relation is appealing and works quite well for glass in the visible region of the spectrum. Figure 2.2 shows the plots of refractive index for different types of glasses.

It can be seen that in the visible region, different glasses show normal dispersion. It is also found that for these materials only first two terms in Cauchy's equation are sufficient to calculate their refractive index. Therefore, Cauchy's equations are very convenient to deal with the materials that are conventionally used in optics. There are other optical components that exhibit negative dispersion and high transmission, for example Transmission gratings. The diffracting angle in a particular order of diffraction is proportional to the wavelength of the outgoing light. The sense of dispersion is opposite in the case of grating compared to that of prism, hence it is called negative dispersion. A type of grating, blazed gratings transmits at one particular order of diffraction. Therefore, it is easy to see that combining both refractive and diffractive devices, as they have opposite sense of dispersion, one can realize achromatic optical components. This idea is not new and has been prevalent in the community for some time. In [2], plano convex lens-diffractive lens hybrid component is

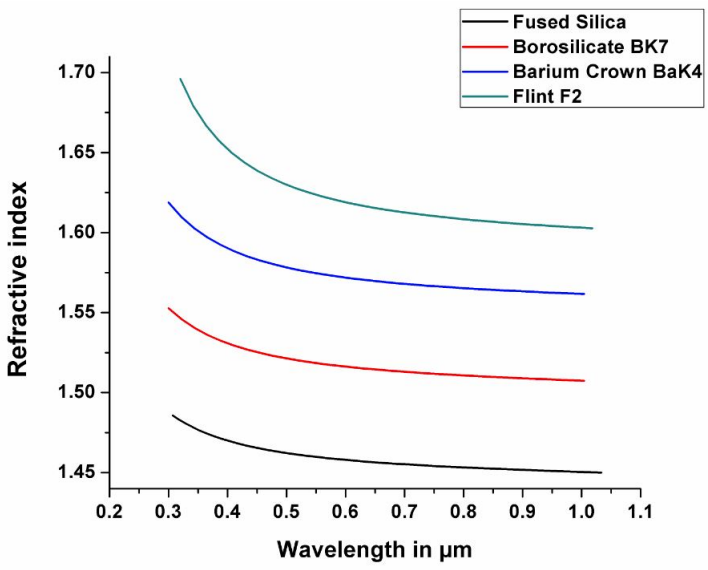

Figure 2.2: Normal dispersion of various types of glasses in visible region of spectrum

used to tune the dispersion. Achromatic lens is designed as well as dispersion of lenses made of different glasses is imitated. Utilizing similar hybrid device, reduction of chromatic and spherical aberration is shown analytically in [3]. In [4], diffractive-refarctive hybrid corrector is proposed for achro- and apochromatic corrections of optical systems. In this work, a compound triplet system is proposed with diffractive lens as one of its components.

In the context of metasurface, the discussion on controlling the sign of dispersion using metasurface in [5] is quite interesting. In this work it is shown that by controlling both phase and antenna dispersion it is possible to realize normal, zero and negative dispersion using metasurface. This again emphasizes the flexibility and range of functionalities that can be achieved using metasurfaces. In [6], it is shown that to suppress chromatic aberrations one needs to address both group delay $\frac{\partial\phi}{\partial\omega}$ and group delay dispersion $\frac{\partial^2\phi}{\partial\omega^2}$. Here ϕ is the phase shift from each nanoantenna of the metasurface and ω is the frequency of light. This has been realized by considering the dispersive nature of the resonances of nanostructures forming the metasurfaces. This approach is discussed in detail in the next chapter for lens chromatic aberration correction. Such a level of refinement is necessary to obtain fully achromatic devices but is beyond the scope of this thesis work. Here, we have followed a different approach of imitating a blazed grating using metasurface to obtain negative dispersion. It is nothing but a beam deflector and one can tune the amount of dispersion of deflected

beam by tuning the period of the metasurface. Here, we use diffraction of metasurface to generate dispersion instead of addressing dispersion of each meta-unit. However, normal and zero dispersion cannot be achieved using this approach which upholds the generality of the method used in [5].

The objective here is to compensate normal dispersion of conventional optical components such as a prism, lens etc with the negative dispersion of metasurface. This can be realized using metasurfaces which can be tuned to produce exactly equal magnitude of dispersion as of a refractive component but with opposite sense. Recalling the discussion in the introduction chapter (equation 1.1), generalized law of refraction for normal incidence on metasurface can be written as

$$n_{medium} Sin(\theta_t) = \frac{\lambda}{2\pi} \frac{d\phi}{dx} \tag{2.2}$$

Here phase gradient $\frac{d\phi}{dx}$ controls the angle of deflection θ_t. Assuming that phase gradient is a constant term along the metasurface, we obtain a beam deflector with λ factor denoting the dispersion from the metasurface. This is exactly opposite to the case of a prism where the refracting angle increases with decreasing wavelength. The aim of this chapter particularly is to demonstrate that a phase gradient metasurface can mitigate, if not completely compensate for, prism dispersion. Naturally the question arises that why a prism, which is typically used to reveal dispersion, is being used to show exactly the opposite. However, our final objective is to mitigate chromatic dispersion of a lens with metasurface which would have practical implications. Before jumping into the case of lens, our approach is tested on prism which is a simpler case and is shown as a proof of concept.

2.1 Prism dispersion

Consider a glass prism whose dispersion behavior is discussed in the previous section. Metasurface dispersion term varies as λ whereas glass dispersion follows Cauchy's relation which goes as λ^{-2}. To compensate it with metasurface, an approximation is required over Cauchy's equation. Using Cauchy's equation for glass,

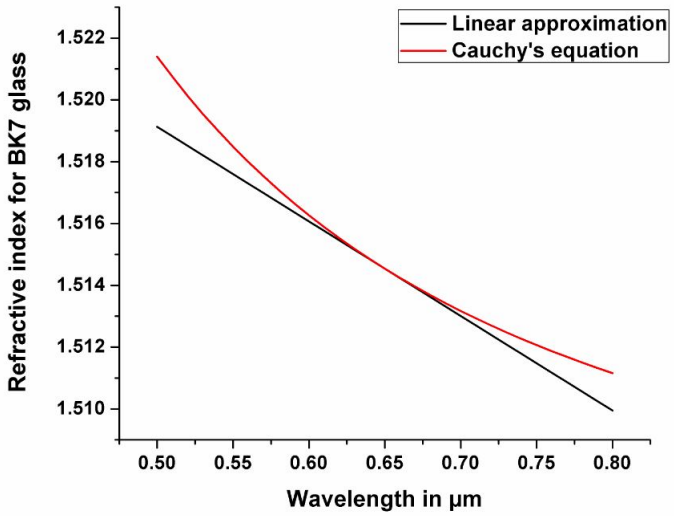

Figure 2.3: Linear fitting of BK7 glass dispersion from Cauchy's equation in visible region

$$n(\lambda) = A + \frac{B}{\lambda^2} \tag{2.3}$$

The refractive index can also be written as Taylor expansion around λ_0 as,

$$n(\lambda) = n(\lambda_0) + \frac{dn}{d\lambda}\Big|_{\lambda=\lambda_0}(\lambda - \lambda_0) + \frac{d^2n}{d\lambda^2}\Big|_{\lambda=\lambda_0}\frac{(\lambda - \lambda_0)^2}{2!} + ... \tag{2.4}$$

From the plots in Figure 2.2, one can notice that the curve is approximately linear in the visible region. Substituting Cauchy's relation in the above equation and neglecting higher order terms, we get,

$$n(\lambda) = A + \frac{3B}{\lambda_0^2} - \frac{2B}{\lambda_0^3}\lambda \tag{2.5}$$

Figure 2.3 includes the plot for linear approximation for BK7 glass with $\lambda_0 = 650nm$ which results in R^2 value around 0.92. For smaller wavelengths, the deviation is greater because of increasing curvature in the trend. The value λ_0 can be used as a parameter to optimize the linear approximation over the chosen range of wavelengths.

2.2 Prism – Metasurface combination

The work discussed in this chapter especially from this section can be found in [7] .A Borosilicate glass (N-BK7) prism with prism angle of 30° was chosen. The phase gradient metasurface is glued to one of the sides of the prism using index matching oil as shown in the figure 2.4. Light ray enters the prism at the first interface at normal incidence and encounters the second surface which is the prism-metasurface interface. The refraction at this point is given by generalized law of refraction written for prism-metasurface-air interface.

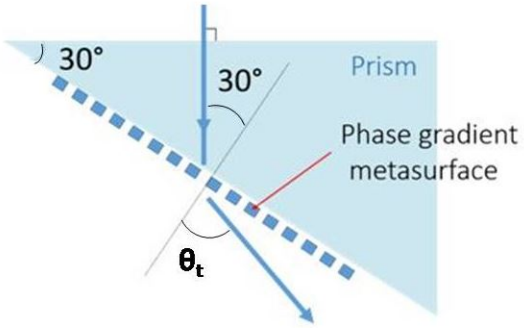

(a)

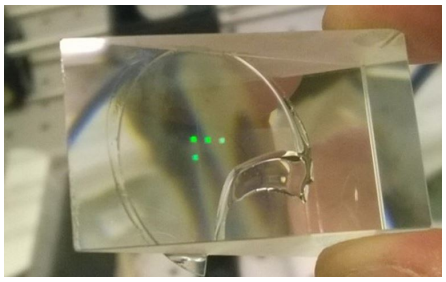

(b)

Figure 2.4: A)Phase gradient metasurface and prism combination, B)Image of metasurface glued to a side of prism

$$n_{air}\sin(\theta_t) - n_{prism}\sin(\theta_i) = \frac{\lambda}{2\pi}\frac{d\phi}{dx} \tag{2.6}$$

With prism angle of 30° and normal incidence at interface 1, $\theta_i = 30°$

$$Sin(\theta_t) - \frac{n_{prism}}{2} = \frac{\lambda}{2\pi}\frac{d\phi}{dx} \tag{2.7}$$

In the range of 500-800 nm, applying linear approximation on refractive index of glass by substituting equation 2.5 we get

$$Sin(\theta_t) = \frac{\lambda}{2\pi}\frac{d\phi}{dx} + \frac{A}{2} + \frac{3B}{2\lambda_0^2} - \frac{2B}{2\lambda_0^3}\lambda \tag{2.8}$$

Imposing the condition that the refracted beam is dispersion free, all the terms with λ are grouped and equated to zero. We get the following relation for phase gradient.

$$\frac{d\phi}{dx} = \frac{2\pi B}{\lambda_0^3} \tag{2.9}$$

By substituting corresponding values one can determine the metasurface phase gradient for dispersion compensation. Although, it has to be noted that here λ_0 is a parameter for design. Just to be safe, we designed 3 different phase gradients $4, 6, 8 \times 10^{-5} rad/nm$ which is the range of values one gets from the above relation.

2.3 FDTD simulation

The simulation and nanofabrication were performed by Prof. Federico Capasso's group, our collaborators at Harvard university. The ability to realize high-efficiency dielectric metasurfaces is critically dependent on the optical properties of the constituent material which is characterized by the complex refractive index, $\tilde{n} = n + i\kappa$. The material should have negligible absorption loss $\kappa \approx 0$ with relatively high refractive index ($n > 2$) at visible wavelengths. Low absorption is necessary for high transmission efficiency. Along with it, high refractive index ensures strong confinement of the light, which ultimately allows full control over the phase of the outgoing wavefront (phase shift range from 0 to 2π).

The material should be optically smooth, having a surface roughness that is much smaller than the wavelength of light. High surface roughness introduces extraneous light scattering, which is a significant source of loss. To minimize roughness, the material must be amorphous or single-crystalline, as the grain boundaries in polycrystalline materials increase roughness and act as light-scattering centers. We chose amorphous TiO_2 as our constituent material for nanopillars. [8]. The amplitude and phase responses are related to the radius of nanopillar meta-atoms. To quantify the phase delay from a nanopillar of given dimension, electromagnetic FDTD (Finite-Difference Time-Domain) simulation of nanopillar arranged in a square lattice were performed using Lumerical. The simulation was done for nanopillars of constant height 600 nm but for varying pillar diameter and wavelengths of incident light. Since the pillars have circular cross section, they are insensitive to incident polarization. As shown

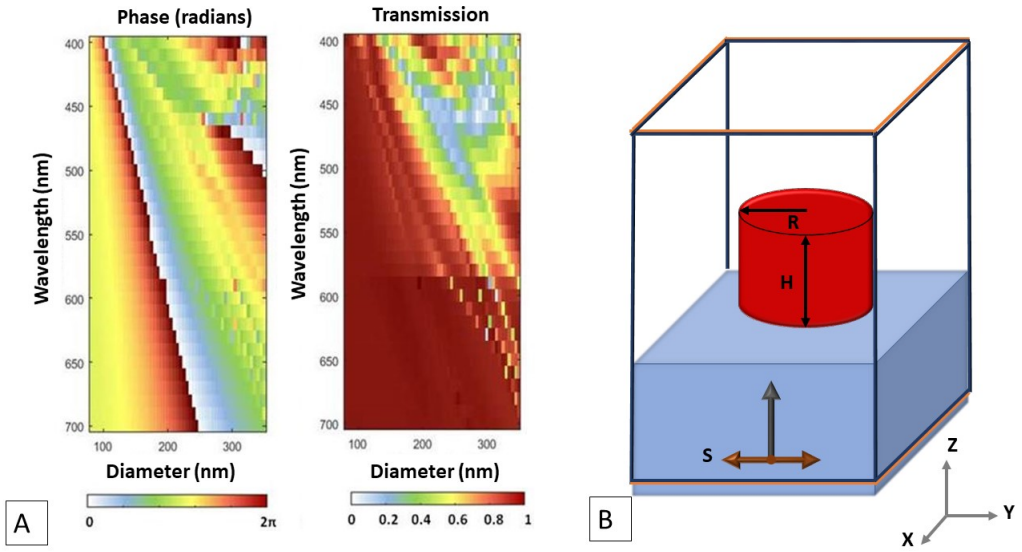

Figure 2.5: A) Phase and transmission maps B) FDTD Simulation setup of a unit cell. TiO_2 nanopillar placed on SiO_2 substrate illuminated by plane wave source S. Constant height H of 600 nm and varying radius R is used. Planes closed by blues lines represent Periodic boundary condition and orange lines Perfectly Matched Layer (PML). Phase and Transmission values are obtained after projecting the fields to a farfield plane.

in figure 2.5 B), for the FDTD simulation, Perfectly Matched Layer (PML) conditions in the direction of light propagation (2 faces) and periodic boundary conditions along all the in-plane directions (4 faces) were used. Dimensions of one unit cell along both x and y axes were around 285 nm. The use of PML boundary conditions in the propagation direction results in an open space simulation while in-plane periodic boundary conditions mimic a subwavelength array of identical nanostructures. We obtain the phase and transmission map as shown in figure 2.5 (A). From the phase map, phase shift elements ranging from 0 to 2π are chosen to arrange in a period of metasurface equivalent to one period of a grating. Phase elements are arranged such that the phase shift imparted by the nanopillars increases linearly with the distance in a period. The periodicity determines the constant phase gradient value of the metasurface. From the transmission map, pillars with highest transmission are chosen.

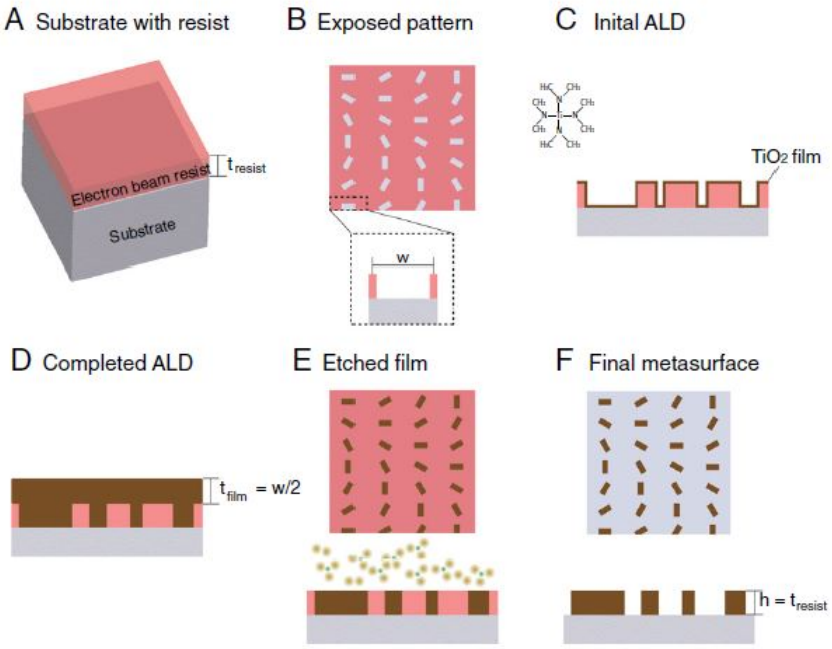

Figure 2.6: Fabrication steps followed to realize the metasurface. A)Electron Beam Resist (EBR) on fused silica with thickness t_{resist} that ultimately sets the height of the final structure (perspective view) B) Inverse of the final metasurface pattern imprinted into the EBR by electron beam lithography and subsequent development of the pattern (top view). The boxed area is an expanded cross-section of the maximum feature width, w C) Initial TiO_2 deposition via ALD conformally coats sidewalls and top of the EBR and exposed substrate (side view). TDMAT molecule used for ALD is also shown D) Completed deposition of the TiO_2 yields a film thickness greater than half the width of the maximum feature size. E) Exposed tops of the TiO_2 metasurface and residual EBR after reactive ion etching with a mixture of Cl_2 and BCl_3 ions (top and side view) F) Final Metasurface after removal of remaining EBR.[8]

2.4 Nanofabrication

As discussed in [8], to achieve highly efficient metasurface devices while preserving the optical properties of ALD (Atomic Layer Deposition)-prepared TiO_2, we used the fabrication process as shown in Figure 2.6. First step being spin coating of Electron Beam Resist (EBR) onto a fused silica substrate to produce a layer with thickness, t_{resist} (Figure 2.6 A). It has to be noted that t_{resist} sets the height of the final nanopillars. The resist was patterned using electron beam lithography and subsequently developing in solution to remove the exposed EBR. The exposed sample was transferred to an Atomic Layer Deposition (ALD) chamber set to 90 ℃. During the deposition, the gaseous TiO_2 precursor Tetrakis (dimethylamino) Titanium(TDMAT) coated all exposed surfaces, producing a conformal film on the top and side of the EBR as well as on the exposed fused silica substrate (Figure 2.6 C). The ALD process was allowed to reach a specific thickness so that all features had been completely filled with TiO_2. The residual TiO_2 film that coats the top surface of the resist was removed by reactive-ion-etching with the mixture of BCl_3 and Cl_2 gas (8:2). The etch depth was equal to t_{film} so that the etching process exposes the underlying resist and the top of the nanostructures (Figure 2.6 E). We removed the remaining resist and left only the nanostructures that make up our metasurface (Figure 2.6 F). Even though the figure 2.6 shows nanopillar with rectangular cross-section, we have fabricated pillars with circular cross section in our metasurface.

Figure 2.7 A) shows the SEM(Scanning Electron Microscopy) image of fabricated metasurface. Nanopillars ranging from diameter of 100 to 280 nm are included in the metasurface. Since the phase gradient required is small (of the order of $10^{-5} rad/nm$), the diameter variation in the SEM image is minute. Figure 2.7 B) describes the expected diffracting properties of phase gradient metasurface with two prominent orders of diffraction. Fabricated metasurface was glued to a face of Borosilicate glass right angle prism as shown above. Several phase gradient metasurfaces were fabricated, out of which the value expected to give desired result was $4 \times 10^{-5} rad/nm$. The experimental challenge was to measure angles as small as 0.10 degrees to characterize dispersion. For this, we chose Fourier plane spectroscopy technique which gives information about the directionality of different wavelength light.

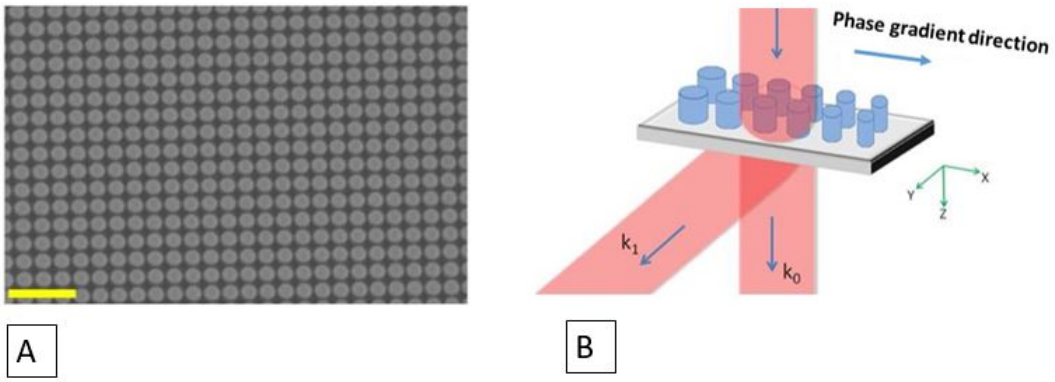

Figure 2.7: A) SEM image of fabricated metasurface. The yellow scale bar corresponds to 1 µm B) Phase gradient metasurface functionality

2.5 Fourier Plane imaging and spectroscopy

Light emanating from sample plane can be thought of as superposition of plane waves along directions θs. When light passes through a microscope objective, different plane wave components get separated. A 2-dimensional equivalent of figure 2.8 a) is light emanating from (θ_x, θ_y) is mapping onto $(f\theta_x, f\theta_y)$ in the back focal plane. It is also called Fourier plane or k-space as 'θ' stands for directionality of the beam which represents momentum of light. Since it is not very convenient to capture the Fourier plane, it is relayed to a distant plane using external optics. The most widely used setup is 4F configuration, which offers an added advantage of being able to tune the magnification. As described in figure 2.8 b), objective lens and tube lens are part of microscope setup and produces image at the plane IP. Lens L1 with focal length 'f' is placed at 'f' distance from IP, resulting in back focal plane image at the plane BFP. Bertrand lens of focal length f/2 is placed at f distance both from BFP and from the Camera. Thus, we obtain the relayed Fourier plane image of IP. Magnification can be adjusted by choosing the appropriate focal length of F1 and BL lenses.

Considering that the input light contains a distribution of wavevector, i.e. the incident light exiting from a dispersive component, it would be interesting to investigate k-space distribution with respect to wavelength. To obtain the spectra, a narrow slit is placed in the back focal plane and the resulting cross-section of back focal plane image is fed to a spectrometer(Figure 2.9). The resolution of back focal plane spectra depends on the width of the slit. [11]

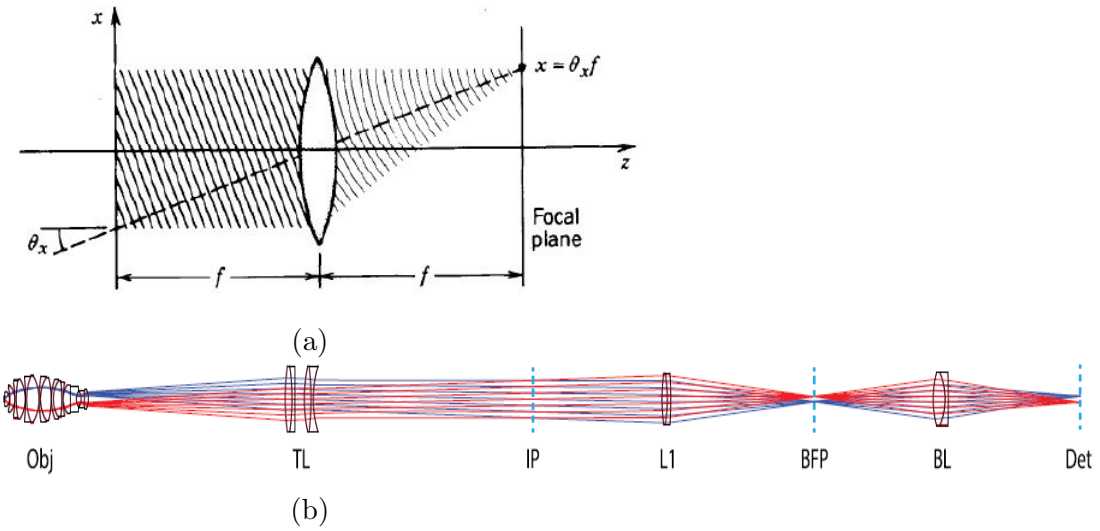

Figure 2.8: Fourier plane imaging a) From a lens [9] b) Using 4F configuration. Obj-Objective lens, TL-Tube lens, IP-Image plane, L1 -Focusing lens, BFP-Back focal plane, BL-Bertrand lens. [10]

The setup built to study the prism-metasurface dispersion is shown in figure 2.9. A Super continuum laser source is utilized to span the wavelength range of 500 to 800 nm. As discussed in the calculations in the previous section, prism is placed such that the light is incident normally at the first interface. This is chosen to avoid chromatic splitting of the light due to dispersion inside the prism before encountering the metasurface at the second interface. The size of the beam spot, about 1mm in diameter, is incident on the metasurface with a size sufficiently large to illuminate the metasurface and the surrounding bare interface. Prism-metasurface combination is imaged using a 0.2NA, 4X objective. Combination of tube lens T (focal length f=10cm), L1 (f=10 cm), L2 (f=5cm) are used to achieve the 4F configuration for Fourier plane imaging. The tube lens reproduces the image from the objective at its focal plane. Lens L1 placed at d=10 cm from the image results in back focal place image at a distance of 10 cm on the image side. Lens L2, placed at a distance of 20 cm from L1, collects the back focal plane image and relays it to a distance of twice its focal length (d= 10 cm) which is at the plane of the slit. The spectrometer used is Andor Shamrock 500i spectrograph (500mm focal distance). The diffraction grating placed after the slit generates the Fourier plane spectra on the intensified Istar CCD camera giving the plot of y component of k-vector vs wavelength.

It is easy to see that for a dispersionless device, the plot of $\frac{k_y}{k_0}$ vs λ would render zero

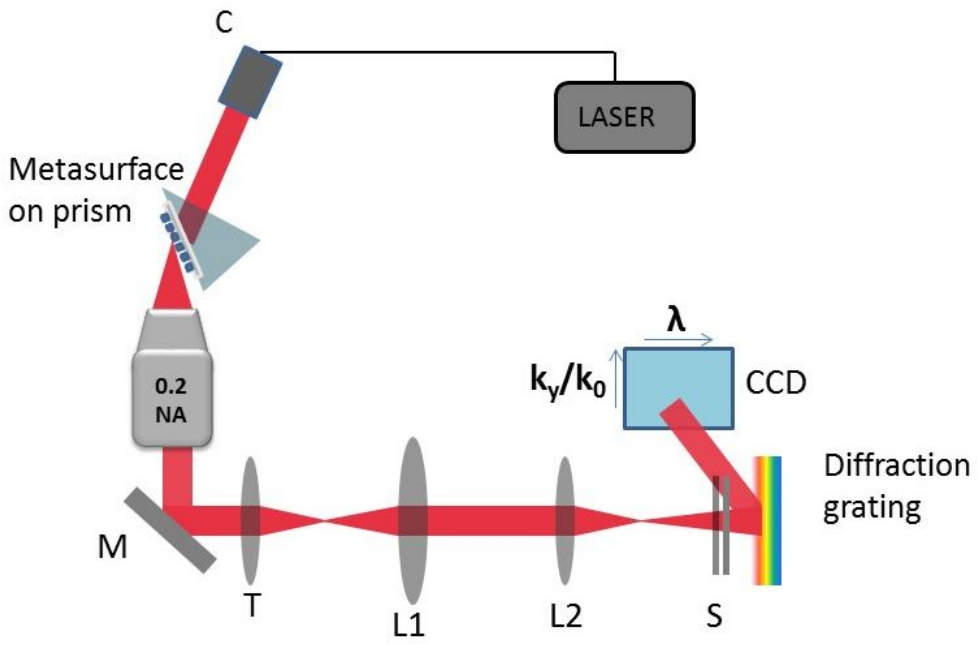

Figure 2.9: Home built Fourier plane spectroscopy setup. C- Collimator, M-Mirror, T-Tube lens, L1,L2- convex lenses, S-Spectrometer slit, CCD-Charge Coupled Device

slope. Hence, the Fourier plane spectra was taken for prism-metasurface combination and then compared it with the case of bare prism. As discussed earlier, metasurface with 4 phase gradients were fabricated (Figure 2.4) and the performance of each of them were studied.

2.6 Experimental results

2.6.1 Calibration

Before jumping into studying prism and metasurface, it is necessary to calibrate the setup for k-space. This is to determine the magnitude of 'k' vector each pixel of CCD corresponds to. For this purpose, a silicon substrate was used in reflection mode with a bright light source to obtain a Fourier plane image. In figure 2.10(a), a general setup for 4F configuration for back focal plane imaging is shown. It produces same result as our setup in figure 2.9. Because of uniform reflection along all k-vectors from the sample one can see a uniform pattern in k-space as shown in figure 2.10(b). The boundary of the k-space pattern is defined by

Numerical Aperture(NA) of the objective as light reflected above this k-vector is not collected by the objective. The upper limit of the pattern marked by blue dashed lines in the figure is given by the circle ($|\frac{k_x}{k_0}, \frac{k_y}{k_0}| = 0.2$). The diameter joining the points (0,-0.2) and (0,0.2) in the image occupies 546 pixels on the CCD camera. Generally, k values follow $Sin(\theta)$ trend to go from k_{min} to k_{max}. Since relatively low NA objective is used, small angle approximation can be considered which results in $Sin(\theta) \approx \theta$. Encashing this, it can be safely assumed that $\frac{k_y}{k_0}$ increases linearly from -0.2 to 0.2. Hence each pixel corresponds to $\frac{k_y}{k_0}$ value of 7.3×10^{-4} units.

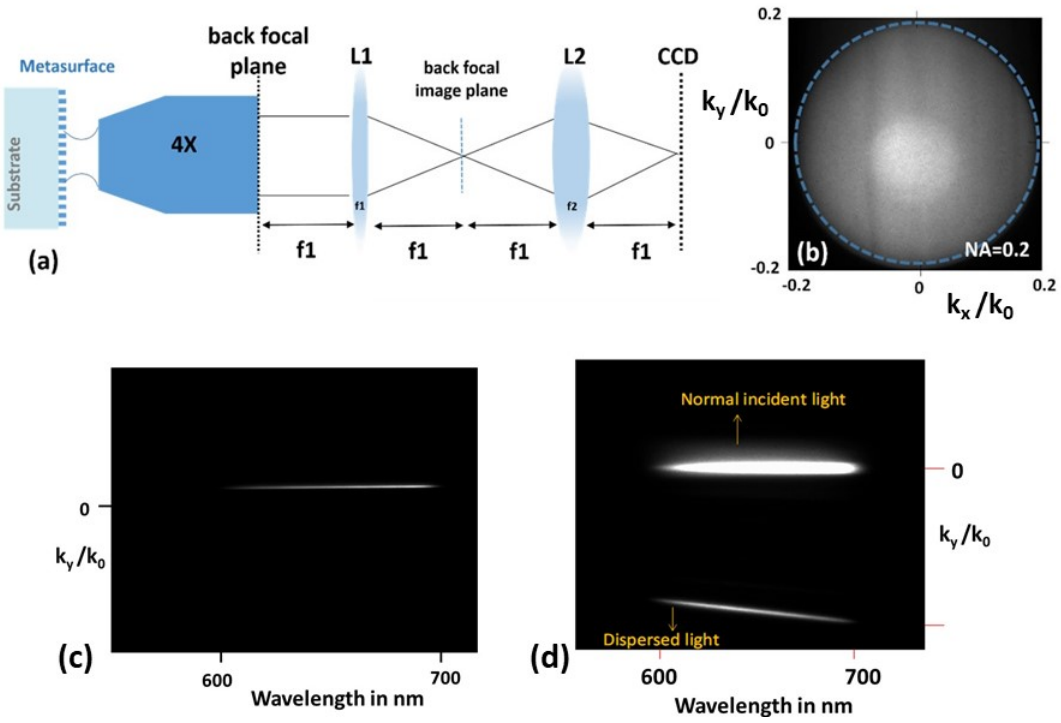

Figure 2.10: a)Fourier plane spectroscopy calibration setup b) Calibration result c) K-space spectra from bare prism d) K-space spectra from metasurface of phase gradient $5 \times 10^{-3} rad/nm$. Table- Comparison of measured and calculated slopes of k-space spectra of a prism for different wavelength range

Wavelength in nm	Measured slopes k_y/k_0 per nm (e-5)	Calculated slopes k_y/k_0 per nm (e-5)	Percentage deviation
500-600	-4.2	-4.3	2.3
600-700	-2.8	-2.9	3.5
700-800	-1.4	-1.4	0

To validate the calibration, prism dispersion was measured using this technique as shown in 2.10 (c)(only 600-700nm wavelength range is shown) and compared with the calculated values. Using refractive index data for BK7 glass prism and small angle approximation, prism dispersion was calculated. As discussed earlier, slope of k-space spectra correspond to dispersion and a good agreement between measured and calculated dispersion can be found from the table (Figure 2.10) with a small deviation in the wavelength range of 500 to 800 nm. This study verifies that the calibration calculation is reliable and contributes negligible error to the actual measurement. Figure 2.10 (d) is the measured k-space spectra for a metasurface with a phase gradient of $5 \times 10^{-3} rad/nm$. The zero order (Normal incident light) and first order of diffraction (Dispersed light) are indicated. Zeroth order is unaffected light from the metasurface, hence no dispersion. Whereas, first order diffraction line shows significant slope indicating negative dispersion as the magnitude of k-vector is increasing with wavelength of light. Also, the sign of the slope is a matter of convention, for instance if the metasurface is aligned such that the first diffraction order is above zeroth order in the k-space spectra then we would have a positive slope. It is also important to note that prism dispersion slope is tiny compared to that of metasurface. Hence, to compensate for prism dispersion it is required to utilize a metasurface with much lower phase gradient (of the order of magnitude $10^{-5} rad/nm$).

2.6.2 Dispersion compensation results

Figure 2.11 is the k-space spectra for prism-metasurface combination as shown in figure 2.4. Phase gradient with the best compensation $4 \times 10^{-5} rad/nm$ was used in the experiments. As indicated in figure 2.11 (a), the upper curve contains dispersion compensated information. Since the slope of the spectra line is very close to zero, it is calculated from the pixel information. As metasurface transmission is not very high from 500 to 540 nm, this region is not included in the discussion. To control the bandwidth and central wavelength of the

light, the broadband signal from the super continuum is coupled to a spectral filter. The maximum available bandwidth which is controllable with the system is around 100 nm around the central wavelength. To obtain larger spectra, several measurements have to be realized. The Super continuum source used in the experiments has maximum bandwidth of 100 nm, hence the spectra was taken in 3 parts. The spectra in figure 2.11 a)-c) show two intensity dispersion curves representing the zero-order transmission (lower line) and corrected first-order diffraction of the dispersive device with the metasurface (upper line). It is important to note that since the metasurface adds an additional transverse momentum to the refracted light, the achromatic refraction occurs at an angle of 49.59° which is different from the normal refraction at an angle of 49.22° for the central wavelength. To simultaneously observe and compare the dispersive properties of the rectified first order with respect to the zero order, it is necessary that the spot size of the incident light to be larger than metasurface, i.e. part of the light is interacting with metasurface and part of it is normally refracted by the prism only. Spectra collected with the bare prism is not shown but the dispersion slopes of prism and that of prism-metasurface is compared in the table. It can be seen that the dispersion compensation is effective in the wavelength range of 600 to 800 nm. It is expected as the prism dispersion tends to show linear behaviour at higher wavelengths which matches well with the metasurface dispersion.

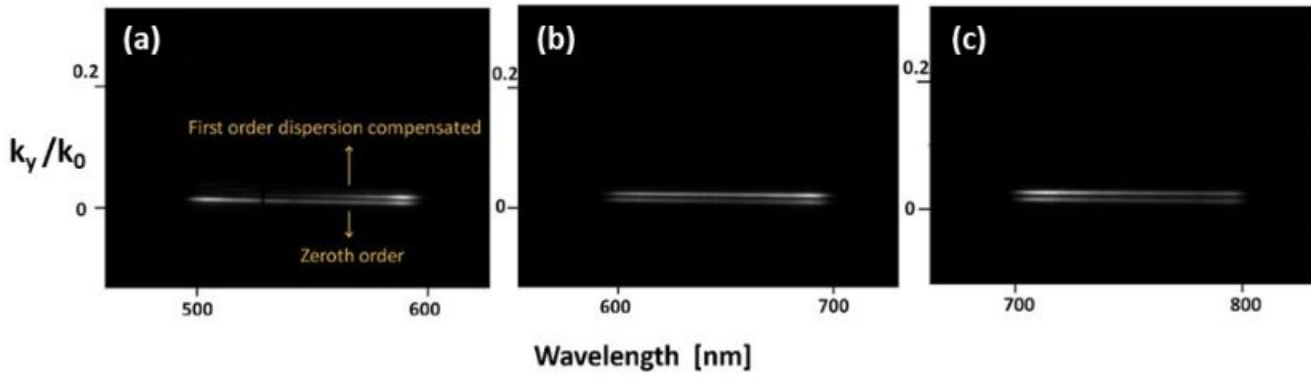

Figure 2.11: Fourier plane spectroscopy experimental results shown as k_y/k_0 as a function of wavelength. Table- Comparison of slopes of k-space spectra of bare prism and first order dispersion compensated line of Prism-metasurface combination for different wavelength range.

Wavelength in nm	Prism k_y/k_0 per nm (e-5)	Prism + metasurface k_y/k_0 per nm (e-5)	Percentage compensation (mean value)
540-600	-4.2 ± 0.1	-2.0 ± 0.5	52
600-700	-2.8 ± 0.1	-0.5 ± 0.9	82
700-800	-1.4 ± 0.1	0.2 ± 0.6	114

2.6.3 Error calculation

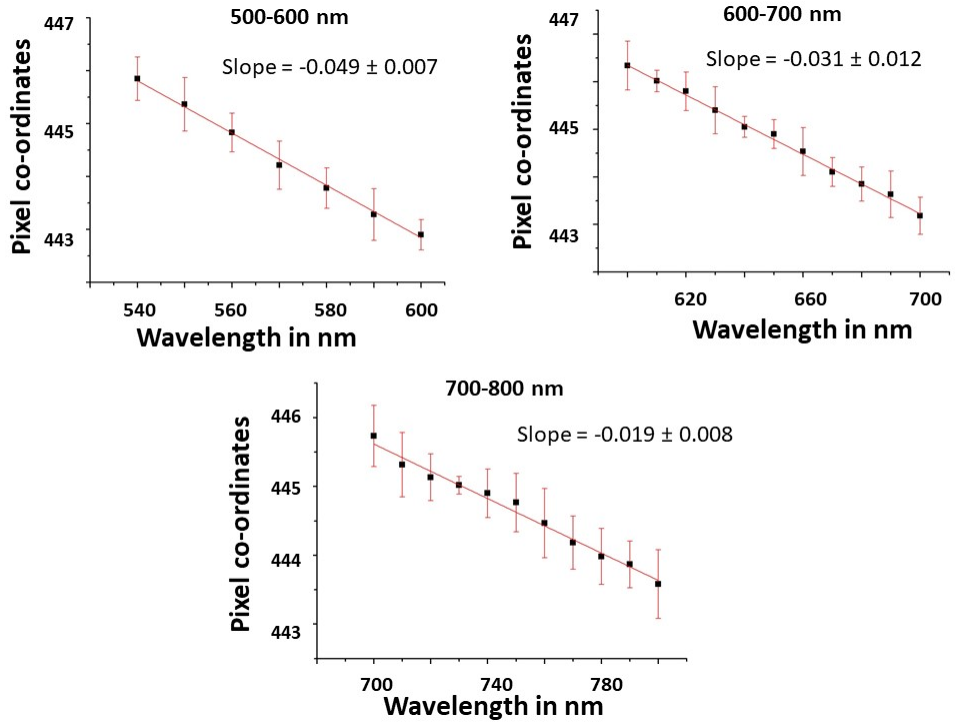

Figure 2.12: Error bars from raw data of fourier plane spectra of prism-metasurface combination

Quantifying error in the discussed experiments is crucial as we are dealing with extremely small amounts of dispersion. In figure 2.12, the calculation of slope and error is discussed for prism-metasurface combination. The k-space spectra line has considerable thickness owing to the width of the slit which adds to the uncertainty. Also, size of one pixel sets the lower limit for dispersion measurement. Therefore, for a given wavelength highest intensity pixel is noted and for every 10 nm interval this value is averaged. The mean value is plotted as shown in figure 2.11 with the computed standard error within the interval as error bars.

By fitting the points to a straight line one obtains the slope which quantifies dispersion. Minimum and maximum slope can be calculated by fitting different lines to the plot which gives error around the mean slope. The values plotted are raw data and the net slope is calculated (table of figure 2.11) after deducting the zero error obtained from the control (blank) experiment. Therefore, in conclusion the uncertainty in measurement is determined by the slit width and pixel size. Fabrication imperfections, misalignment in the experimental setup, deviation of prism dispersion from linear behaviour are other sources of error.

2.7 Achromatic compression

A possible application of our hybrid optical components is the achromatic beam compressor. The objective of the device is as shown in figure 2.13. The purpose of such optical device is to collect optical signal using a large aperture, thus high photon flux, and compressing it to improve the signal going to a detector or an imaging optical system. Therefore, it is designed to deflect the rays arriving from infinity in the perpendicular direction with the compressed beam width and rendering the deflection chromatic dispersion free. This device could be useful in compact zoom lens system. We have proposed here a solution based on prism metasurface combination to make the compression achromatic.

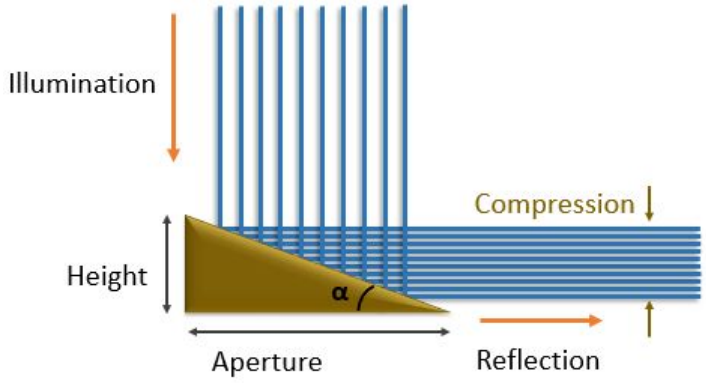

Figure 2.13: Compression of reflected beam

Compression factor 'C' is defined as the ratio of beam width of incident light to that of reflected light. Consider a mirror instead of the wedge, to deflect beam by 90° the mirror has to be placed at $\alpha = 45$ which would result in no compression of reflected beam. It has

to be noted that 'C' is the ratio of aperture size and height of the wedge for a perpendicular reflection. The aim is to achieve compression factor of around 2. But from the triangle formed by the wedge, cot(α)=aperture/height. Therefore, C=cot(α) and for the design it is required that C¿2 which implies $\alpha < \cot^{-1}(2)$. From this, the upper limit for wedge angle α is considered to be 27°. Instead of a mirror one can also think of using a beam deflecting metasurface in reflection mode to achieve compression. This solution works for monochromatic light but with broadband light metasurface produces significant dispersion which is not convenient for practical application. Hence we have proposed a simple and effective design to satisfy the constraints of compression and achromaticity in figure 2.14.

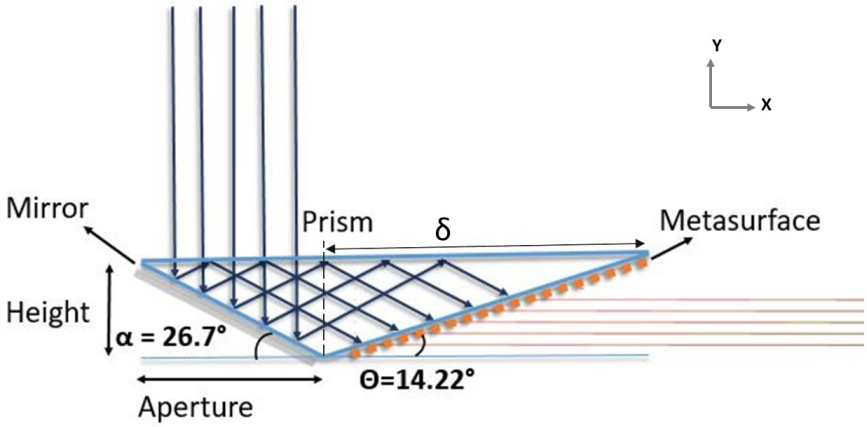

Figure 2.14: Device design for achromatic compression using a mirror, a prism and a metasurface. The rays exiting from the metasurface are obtained from ray tracing analysis with 3 wavelengths of incident light 450nm, 550nm, 650nm.

The idea is to use a mirror for reflection, a prism for Total Internal Reflection and a phase gradient metasurface for dispersion compensation as shown in the figure 2.14. The angle α is chosen such that compression is achieved and enables Total Internal Reflection (TIR) at the next reflection. For TIR to occur at the top surface of the prism, α should satisfy the condition, $\alpha > \frac{\theta_c}{2}$ where θ_c is the critical angle of the prism material. Therefore, it sets the lower limit for α where as compression factor determines the upper limit. For example, for the setup in figure 2.14, with prism material as BK7 and compression factor around 2, the allowed range for α is $20.66° < \alpha < 27°$. Also, it has to be made sure that the reflected rays from the mirror reaches the top surface instead of directly reaching the metasurface. For this, the slope of rays reflected from the mirror should be more than that of the face of prism

to which metasurface is attached ($\tan(\theta)$). This gives the condition on the angles of prism as $\theta < 90 - 2\alpha$ where angles are in degrees. Angle θ is the parameter for ensuring achromatic refraction and perpendicular deflection with respect to the incident beam. Generalized law of refraction at metasurface can be written as,

$$Sin(\theta_t) - nSin(2\alpha - \theta) = \frac{\lambda}{2\pi}\frac{d\phi}{dr} \tag{2.10}$$

Here θ_t is the angle of refraction, $2\alpha - \theta$ is the incident angle obtained from prism angles, $\frac{d\phi}{dr}$ is the phase gradient of the metasurface. Refractive index of prism 'n' is linearized as obtained from equation 2.5. For condition of achromaticity, grouping terms containing λ and equating to zero we get,

$$\frac{2B}{\lambda_0^3}Sin(2\alpha - \theta) = \frac{1}{2\pi}\frac{d\phi}{dr} \tag{2.11}$$

Here λ_0 is the design wavelength. From equation 2.10, we obtain another equation to calculate angle θ.

$$Sin(\theta_t) = (A + \frac{3B}{\lambda_0^2})Sin(2\alpha - \theta) \tag{2.12}$$

By design, the refracted light from the metasurface is supposed to be parallel to the x-axis, which gives $\theta_t = 90° - \theta$. Substituting $\sin(\theta_t)$ with $\cos(\theta)$ and considering $\alpha = 26.7°$ and BK7 glass as prism material with $\lambda_0 = 650nm$, from equation 2.11 and 2.12 we get $\theta = 14.22°$ and metasurface phase gradient to be 0.1214 rad/µm. With these parameters, ray tracing was done using Matlab codes for 3 wavelengths 450 nm, 550 nm, 650 nm to represent broadband light. In figure 2.14, rays refracted from the metasurface is obtained from ray tracing results. One can see that the 3 wavelengths are almost superimposed on each other indicating negligible dispersion. Compression factor achieved with this design was 1.99.

In the figure 2.15, dispersion from prism with and without metasurface in our design is discussed. In the range of 450 nm to 750 nm wavelength, prism-metasurface combination dispersion is 2.5 times less than that of bare prism. Again, the dispersion compensation is

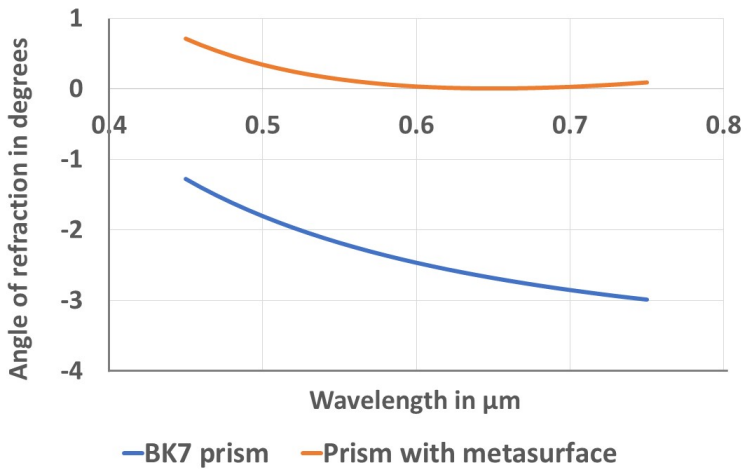

Figure 2.15: Dispersion comparison of prism and prism-metasurface combination. Here the angle of refraction refers to angle made by the refracted ray with the x-axis.

better at higher wavelengths because of better linear approximation of glass dispersion for $\lambda > 600nm$.

The limitation in this setup is the large size of prism. The quantity δ shown in figure 2.14 is dependent on θ angle of prism. In the above case for aperture = 5mm and height of prism = 2.51 mm and $\theta = 14.22°$, δ turns out to be 9.65 mm. This is large compared to height of the prism and aperture and renders the whole device bulky. It can be seen that δ depends on θ and this has to be minimized. From equation 2.11 and 2.12, θ depends on refractive index of prism and α. Since the allowed range of α is limited, material of prism can be chosen such that δ is relatively small. Here instead of BK7 glass, we study with Gallium Nitride (GaN) as the material of prism. For crystalline GaN, the refractive index is referred from [12]. In the range of 500-700 nm the refractive index is plotted and fit to a linear curve given by the relation, n=$2.652 - 0.421\lambda$. The critical angle for this prism for 650 nm (n=2.378) is $\theta_c =$ is 24.8°. So, the lower limit for α is $\theta_c/2 = 12.4°$ and the upper limit governed by 'C' is the same as for glass as 27°. Therefore, a wider range of angles is available for GaN compared to BK7 glass.

The quantity δ is written as a function α and compared for BK7 glass and GaN. From equation 2.12, by considering the refracted ray to be parallel to x-axis we have $\sin(\theta_t) = \cos(\theta)$ and by solving for θ we get $\tan(\theta) = \tan(2\alpha) - \frac{1}{\cos(2\alpha)(A+\frac{3B}{\lambda_0^2})}$. Also from the prism angles

$\tan(\theta) = \frac{h}{\delta}$ where h=height of the prism. By considering $a = A + \frac{3B}{\lambda_0^2}$) we get

$$\delta = \frac{h}{\tan(2\alpha) - \frac{1}{\cos(2\alpha)a}} \tag{2.13}$$

Employing this, the comparison of size between BK7 glass prism and GaN prism is shown in figure 2.16 for specific parameters. One can see that with higher refractive index material, the prism can be made less bulky. Also there is a trade-off between compression factor 'C' and δ which represents the size of the prism. Therefore, by tuning design parameters, α and material of prism one can realize optimized achromatic beam compressors.

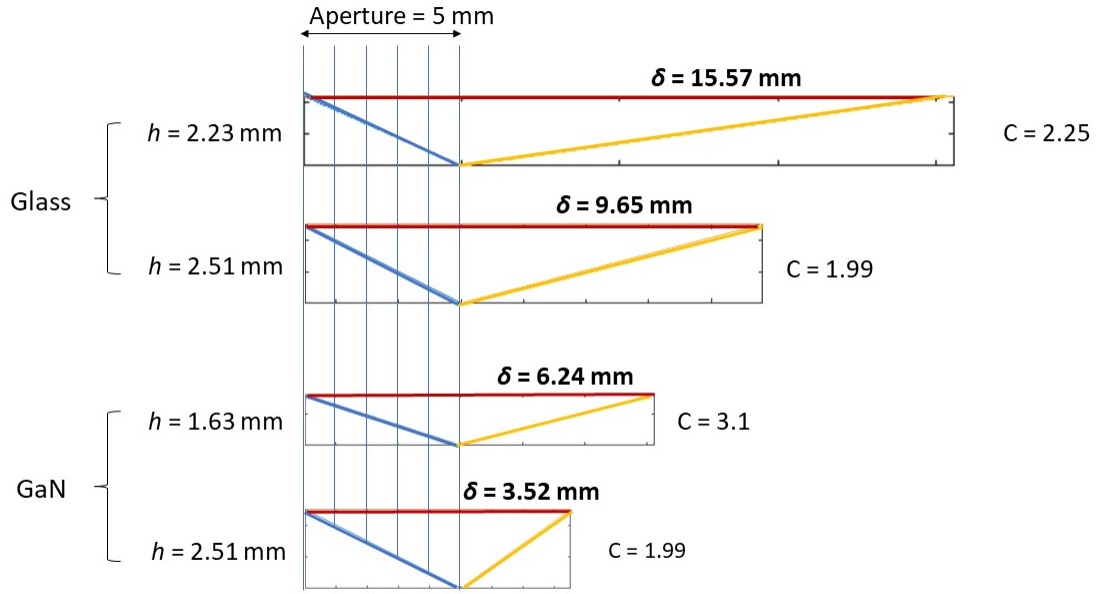

Figure 2.16: The size of the prism represented by δ is shown for 4 different cases by varying height of prism and material of prism as BK7 glass and GaN

2.8 Conclusion

In this chapter, we have shown that to obtain achromatic devices one can combine refractive and diffractive optical components. The tunability of metasurface dispersion by varying its phase gradient is of great advantage. Moreover, approximately linear dispersion of glass in visible region favors the design. Extending the same idea to other optical components like lenses would be very beneficial as chromatic aberration is a major hurdle in imaging systems. This is discussed in the next chapter. All in all, we demonstrate a method by which hybrid optical components can be realized, which have the advantage of both refractive and diffractive components. They reduce the need to polish and grind material, to manufacture large curvature lens and can render larger apertures for an optical device. They also reduce the need for exotic, expensive refractive materials or unusual dispersion glasses. This could be particularly interesting for compact multilayer/cascaded optical systems.

Bibliography

[1] I F Almog, M S Bradley, and V Bulovi. Lorentz model. *MIT OpenCourseWare*, pages 1–34.

[2] Thomas Stone and Nicholas George. Hybrid diffractive-refractive lenses and achromats. *Appl. Opt.*, 27(14):2960–2971, jul 1988.

[3] N Davidson, A A Friesem, and E Hasman. Analytic design of hybrid diffractive–refractive achromats. *Appl. Opt.*, 32(25):4770–4774, sep 1993.

[4] Grigoriy I Greisukh, Evgeniy G Ezhov, and Sergei A Stepanov. Diffractive-refractive hybrid corrector for achro- and apochromatic corrections of optical systems. *Appl. Opt.*, 45(24):6137–6141, aug 2006.

[5] Ehsan Arbabi, Amir Arbabi, Seyedeh Mahsa Kamali, Yu Horie, and Andrei Faraon. Controlling the sign of chromatic dispersion in diffractive optics with dielectric metasurfaces. 4(6), 2017.

[6] Wei Ting Chen, Alexander Y. Zhu, Vyshakh Sanjeev, Mohammadreza Khorasaninejad, Zhujun Shi, Eric Lee, and Federico Capasso. A broadband achromatic metalens for focusing and imaging in the visible. *Nature Nanotechnology*, 13(3):220–226, 2018.

[7] Rajath Sawant, Purva Bhumkar, Alexander Y Zhu, Peinan Ni, Federico Capasso, and Patrice Genevet. Mitigating Chromatic Dispersion with Hybrid Optical Metasurfaces. *Advanced Materials*, 31(3):1805555, jan 2019.

[8] Robert C. Devlin, Mohammadreza Khorasaninejad, Wei Ting Chen, Jaewon Oh, and Federico Capasso. Broadband high-efficiency dielectric metasurfaces for the visible spectrum. *Proceedings of the National Academy of Sciences of the United States of America*, 113(38):10473–10478, 2016.

[9] Bahaa E A Saleh and Malvin Carl Teich. *Fundamentals of photonics*. Wiley-Interscience, Hoboken, N.J., 2007.

[10] Jonathan A. Kurvits, Mingming Jiang, and Rashid Zia. Comparative analysis of imaging configurations and objectives for Fourier microscopy. 32(11):2082–2092, 2015.

[11] Adarsh B Vasista, Deepak K Sharma, and G V Pavan Kumar. Fourier Plane Optical Microscopy and Spectroscopy, feb 2019.

[12] S Pezzagna, J Brault, M Leroux, J Massies, and M de Micheli. Refractive indices and elasto-optic coefficients of GaN studied by optical waveguiding. *Journal of Applied Physics*, 103(12):123112, jun 2008.

Chapter 3

Lens aberration correction

Making lenses has been known to mankind for many centuries. Even today, combination of lenses are used to construct microscopes and telescopes which have brought significant advances in various fields of science. However, lenses come with limitations in the form of aberrations. In addition to it, they are bulky which is a hurdle for realizing compact devices. In recent years, the idea of using metasurfaces as an alternative for conventional optical components, especially lenses, has attracted tremendous attention.

Recalling the phase delay profile for a metalens from introduction chapter for a single frequency ω_0,

$$\phi(r, \omega_0) = -\frac{\omega_0}{c}(\sqrt{r^2 + f^2} - f) \tag{3.1}$$

Based on this, metalenses have been extensively demonstrated in visible- infrared region of spectrum. However, considering the fact that metasurfaces are diffractive devices, chromatic aberration can be seen in these metalenses. The most well known technique to achieve chromatic aberration free metalens is to address phase, group delay and group delay dispersion as discussed in [1] [2]. This can be realized by tuning the dispersion of each nanoantenna to compensate for the overall diffractive dispersion of the metalens. In [1], this is demonstrated by considering the first order Taylor approximation of the phase profile of

a nanoantenna ($\phi(r,\omega)$) with respect to the frequency (ω).

$$\phi(\omega, r) = \phi(\omega_0, r) + \frac{\partial \phi}{\partial \omega}\Big|_{\omega=\omega_0}(\omega - \omega_0) \tag{3.2}$$

Therefore, at a given position 'r' and for central frequency ω_0 in the bandwidth $\Delta\omega$, the metaunit can be described by two parameters $\phi(\omega_0, r)$ and the dispersive term $\frac{\partial \phi}{\partial \omega}(r)$. For these parameters, meta unit library is constructed for nanopillars of different geometry for a given material. The range of phase dispersion values $\Delta\Phi' = (\frac{\partial \phi}{\partial \omega}|_{max} - \frac{\partial \phi}{\partial \omega}|_{min})\Delta\omega$ of the library limits the maximum radius of the achromatic metalens R_{max} that can be achieved. This limit for a metalens of Numerical Aperture NA is given by ('c'-speed of light in vacuum)[1]

$$R_{max} \leq \frac{\Delta\Phi'.NA.c}{\Delta\omega(1 - \sqrt{1 - NA^2})} \tag{3.3}$$

Similarly, the higher order terms in the Taylor expansion of phase correspond to the spread of the wavepacket arrived at the focus. Lesser the spread higher the bandwidth in which achromatic focusing is achievable. In [2], control over the group delay ($\frac{\partial \phi}{\partial \omega}$) and group delay dispersion ($\frac{\partial^2 \phi}{\partial \omega^2}$) terms is demonstrated using coupled nanopillars. Again, this is done by creating a library of particles and performing a systematic parameter search for appropriate dimensions at a given frequency. This method is quite cumbersome. Moreover, it is not convenient for large area metasurfaces (centimeter scale) as the size of the device is limited by the library size as discussed. As mentioned in [3], to design an achromatic metalens of 1.5 mm diameter and numerical aperture of 0.075, one requires a group delay of 95 femtoseconds from the center to edge of a metalens. This would requite TiO_2 nanopillars of height around 12 µm with an aspect ratio of 200. Such high aspect ratio is quite difficult to achieve with current fabrication technologies.

Recently, there have been several works on utilizing metasurface as corrector for lens aberration. In [3], same approach as in [2] of addressing group delay is followed. Chromatic aberration correction of high numerical aperture (NA=1.4) oil immersion microscope objective over the entire visible region was reported. Again, the diameter of the metasurface was of millimeter scale. It is clear that the strict constraint of group delay and group delay dispersion limits the overall size of the metasurface. Therefore we neglect these terms to show that appropriate phase gradient of the metasurface is sufficient to address chromatic as well as spherical aberration in a conventional lens. Metasurfaces for wide angle imaging

have been discussed in [4][5]. But in this chapter we discuss a general strategy for designing a large area metacorrector and the experimental results.

3.1 Lens aberration corrector design

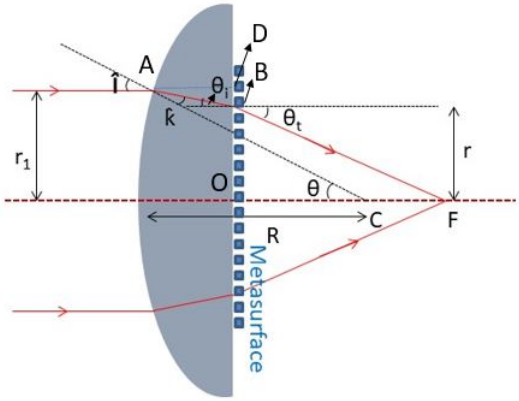

Figure 3.1: Ray diagram for lens-metasurface combination[6]

The schematic for aberration correction of a plano convex lens is shown in figure 3.1. A phase gradient metasurface is glued to the planar side of the lens. Here the paraxial rays are incident on the lens. They encounter two interfaces, curved surface of the lens and lens-metasurface interface. In the figure 3.1, 'R' and 'C' correspond to radius of spherical surface of the lens and its center of curvature respectively. The central thickness of the lens is d_0. 'C' is chosen as the origin for the calculations and the optical axis (red dotted lines) is considered as z-axis. An arbitrary point 'A' on the spherical surface has the co-ordinates $(-Rcos(\theta), Rsin(\theta))$. The refractive index of the glass lens is 'n'.

3.1.1 For chromatic aberration

The following analytical calculation for chromatic aberration correction is discussed in our recent work [6]. At the first interface which is the spherical face of the lens, the rays are incident at an angle 'l' denoted in the figure as $\hat{l}$. From the figure, $l = \theta$ which is given by,

$$Sin(\theta) = Sin(l) = \frac{r_1}{R} \tag{3.4}$$

Refraction at this interface follows the well known Snell's law. Angle of refraction 'k' shown in figure as $\hat{k}$ is given by

$$Sin(k) = \frac{Sin(l)}{n} \tag{3.5}$$

Let the thickness of the lens at any point 'A' (length AD) be 'd' and at the center of the lens be d_0. Then $d = d_0 - R + Rcos(\theta)$. From triangle ABD, the angle formed at A is $l - k$ which is given by,

$$\begin{aligned} Tan(l-k) &= \frac{r_1 - r}{d} \\ r &= r_1 - d(Tan(l-k)) \end{aligned} \tag{3.6}$$

Since d and l-k are small quantities, one can make an approximation that $r1 \approx r$. This simplifies further calculation as it connects the height of a ray 'r1' to the metasurface co-ordinate 'r'. Normal drawn to the planar interface (black dotted lines at point B) and the optical axis are parallel to each other. Therefore, the refracted angle at lens-metasurface interface θ_t is equal to the angle $\angle OFB$. From the triangle OFB, we obtain,

$$f = \frac{r}{Tan(\theta_t)} \tag{3.7}$$

Generalized law of refraction at lens-metasurface interface is written as,

$$Sin(\theta_t) - nSin(\theta_i) = \frac{\lambda}{2\pi}\frac{d\phi}{dr} \tag{3.8}$$

where $d\phi/dr$ is the phase gradient of the metasurface and θ_i which is the incident angle is equal to $l - k$. Assuming that $R >> r$, 'l' and 'k' can be considered as small angles. Therefore, $Sin(l) \approx l$, $Sin(k) \approx k$ and $Sin(l - k) \approx l - k$. Substituting these terms in the generalized law of refraction ie from equation 3.4 and 3.5, we get

$$Sin(\theta_t) - n\frac{r}{R}(1 - \frac{1}{n}) = \frac{\lambda}{2\pi}\frac{d\phi}{dr} \tag{3.9}$$

From the linear approximation of Cauchy's equation as obtained in the previous chapter in equation 2.5, we get

$$Sin(\theta_t) = \frac{r}{R}(A + \frac{3B}{\lambda_0^2} - \frac{2B}{\lambda_0^3}\lambda - 1) + \frac{\lambda}{2\pi}\frac{d\phi}{dr} \tag{3.10}$$

For achromatic focusing, the refraction angle is independent of wavelength. Therefore, grouping together λ terms and equating them to zero, we get

$$\frac{1}{2\pi}\frac{d\phi}{dr} = \frac{2B}{\lambda_0^3}\frac{r}{R} \tag{3.11}$$

Integrating with respect to 'r', we get

$$\phi = \frac{2\pi B}{\lambda_0^3}\frac{r^2}{R} + constant \tag{3.12}$$

Equation 3.12 gives the phase profile of metasurface required to correct chromatic aberration of a plano-convex lens. Even though the calculation is done for one dimensional radial co-ordinate 'r', it is also applicable to two dimensional metasurface. It has to be noted that this phase profile is applicable only for the case when incident angle 'l' is small. For instance, for the case when 'R' is comparable to the height of the ray (r1), approximations considered doesn't hold true. Hence from the exact calculations one would get a different phase profile. Therefore it is also dependent on the dimensions of the lens considered.

To test the calculations, we utilized ray tracing codes in Matlab. The codes for lens was obtained from [7] and was later modified for metasurface. A plano convex lens made of Borosilicate glass (BK7) is considered. Its radius of curvature 'R' and central thickness equal to 2 cm and 2 mm respectively. The ray tracing is performed in the wavelength range of 600 to 800 nm with an interval of 50 nm. The central wavelength λ_0 is equal to 700 nm. By considering these parameters for the setup as in figure 3.1, the raytracing codes were run for the cases of with and without metasurface. The metasurface had phase gradient equal

to that obtained from equation 3.11.

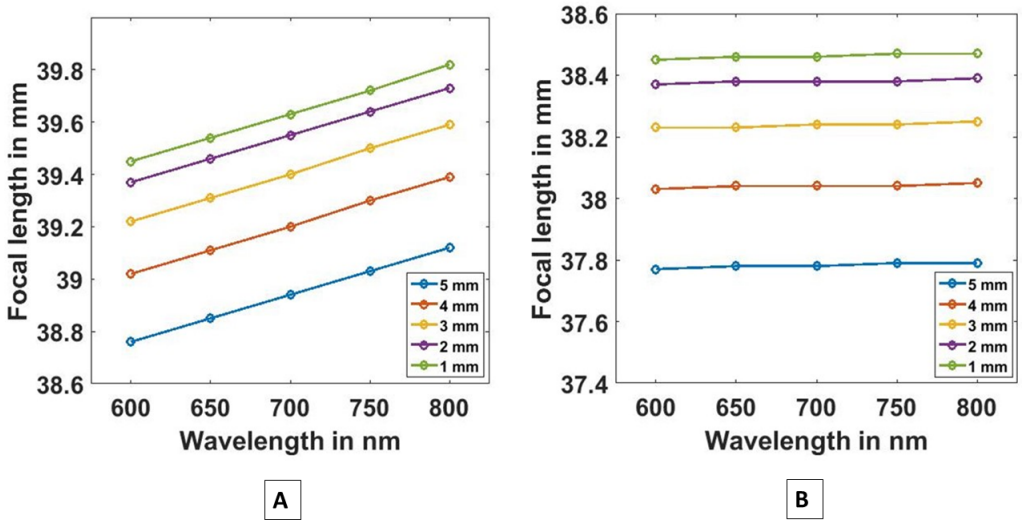

Figure 3.2: Ray tracing results of focal length vs wavelength for A) Plano-convex lens B) Lens-metasurface combination. Different colored plots correspond to different distance of the rays (r1) from the optic axis as given in the legend [6]

Figure 3.2 is the ray tracing results for focal length as a function of incident wavelength for different height of ray from the optics axis (r1). It is evident from figure 3.2 B) that with metasurface, the focal length of the lens is almost constant as a function of wavelength for a given height of ray. By comparing the slopes of plots A) and B), it can be said that the dispersion mitigation is as high as 90% in the wavelength range of 600–800 nm for all 'r1's. However, strong monochromatic aberrations are still present in both the cases. Variation of focal length as a function of 'r1' is the signature of spherical aberration.

3.1.2 Spherical aberration calculation

Spherical aberration is associated with optical components which have spherical surfaces. In the case of a convex lens, considering that the incident rays are parallel to the optic axis, it is seen that the marginal rays converge more compared to the paraxial rays. This implies that the focal length of the lens depends on the distance of the incident ray from the optic axis, this is known as spherical aberration. It is one of the reasons why a smaller aperture on a camera lens produces sharper images.

Here, we calculate the phase gradient of metasurface required to correct lens spherical aberration. The schematic shown in figure 3.1 is followed also in this case. Compared to the previous case, one major difference is that the calculation is done for a single wavelength instead of broadband light. Equations from 3.4 to 3.8, are applicable also for spherical aberration case. But approximating Sin(l) to l and Sin(k) to k doesn't give accurate results, hence accurate values are taken. Therefore,

$$\sin(\theta_i) = \sin(l-k) = \sin(l)\cos(k) - \cos(l)\sin(k) \tag{3.13}$$

Utilizing Snell's law from equation 3.5 and substituting equation 3.4 we get,

$$\sin(l-k) = \frac{r_1}{R}\sqrt{1-\frac{r_1^2}{n^2R^2}} - \frac{r_1}{nR}\sqrt{1-\frac{r_1^2}{R^2}} \tag{3.14}$$

Following equation 3.7, we get $\sin(\theta_t) = \frac{r}{\sqrt{r^2+f^2}}$. The condition for spherical aberration correction is denoted by this equation as the focal length 'f' is taken as constant for any 'r'. Substituting this relation and equation 3.14 into the generalized law of refraction equation 3.8, we obtain,

$$\frac{\lambda}{2\pi}\frac{d\phi}{dr} = \frac{r}{\sqrt{r^2+f^2}} - \frac{r_1}{R^2}(\sqrt{n^2R^2-r_1^2} - \sqrt{R^2-r_1^2}) \tag{3.15}$$

By integrating the above equation, phase delay profile can be calculated. But, one can notice that the equation contains two variables r and r_1. The previous approximation of r and r_1 being equal to each other doesn't give accurate results for spherical aberration case. To experimentally demonstrate this fact, metasurfaces with both approximated and precise values of r was designed. Since r is the metasurface co-ordinate, r_1 which is the lens co-ordinate has to be expressed in terms of r. Revisiting equation 3.6, we had $r_1 = r + d(Tan(l-k))$. From the curvature of lens the thickness d can be written in terms of central thickness d_0 as $d = d_0 - R + \sqrt{R^2 - r_1^2}$.

From the above expressions, $r_1 - r$ is represented by a correction factor 'c'. The idea is to write 'c' in terms of 'r' so that 'r1' can be substituted in equation 3.15 as 'r+c'. In the following calculations, it is attempted to obtain a simple expression for 'c'. Therefore, here

we make a few approximations to calculate the correction factor.

$$\tan(l-k) \approx l-k \approx \sin(l) - \sin(k) = \frac{r_1}{R} - \frac{r_1}{nR} \tag{3.16}$$

Again from equation 3.6, $c = d(Tan(l-k)) = (d_0 - R + \sqrt{R^2 - r_1^2})(\frac{r_1}{R} - \frac{r_1}{nR})$. It is quite cumbersome to solve for r_1. Therefore, we change all r_1 to r in the expression for correction factor c. This approximation is justified by the fact that with respect to a quantity as small as 'c', r_1 and r are approximately equal. From this we get the best estimation of 'c' as,

$$r_1 - r = c = (d_o - R + \sqrt{R^2 - r^2})(\frac{(n-1)r}{nR}) \tag{3.17}$$

Approximating $r^2 << R^2$,

$$r_1 - r = c = (d_o - \frac{R^2}{2r})(\frac{(n-1)r}{nR}) \tag{3.18}$$

Even though many approximations are applied on 'c', we have made an attempt to keep it as close to the real value as possible. This ensures that the results obtained are better than that for c=0 case. Substituting it in equation 3.15 and integrating with respect to 'r' we get,

$$\begin{aligned}\phi(r) = \frac{-2\pi}{\lambda}[\sqrt{f^2+r^2} + \frac{1}{R^2}[(n^2R^2 - (r+c)^2)^{\frac{3}{2}} - (R^2 - (r+c)^2)^{\frac{3}{2}}) \\ \times\frac{1}{3}(1 - \frac{d_0(n-1)}{nR} + \frac{3(r+c)^2(n-1)}{2nR^2}) + \\ \frac{(n-1)}{5nR^2}((n^2R^2 - (r+c)^2)^{\frac{5}{2}} - (R^2 - (r+c)^2)^{\frac{5}{2}})]]\end{aligned} \tag{3.19}$$

Considering another scenario where the correction term 'c' is considered to be zero, ie $r_1 \approx r$, then the integration turns out to be relatively simple and gives the following expression

$$\phi(r) = \frac{-2\pi}{\lambda}[\sqrt{f^2+r^2} + \frac{1}{3R^2}((n^2R^2 - r^2)^{\frac{3}{2}} - (R^2 - r^2)^{\frac{3}{2}})] \tag{3.20}$$

Both the phase profiles in equation 3.19 and 3.20 are considered for spherical aberration correction. They are called as case with 'c' correction and case without 'c' correction. The experimental results of both the cases are compared to stress the importance of accurate calculations.

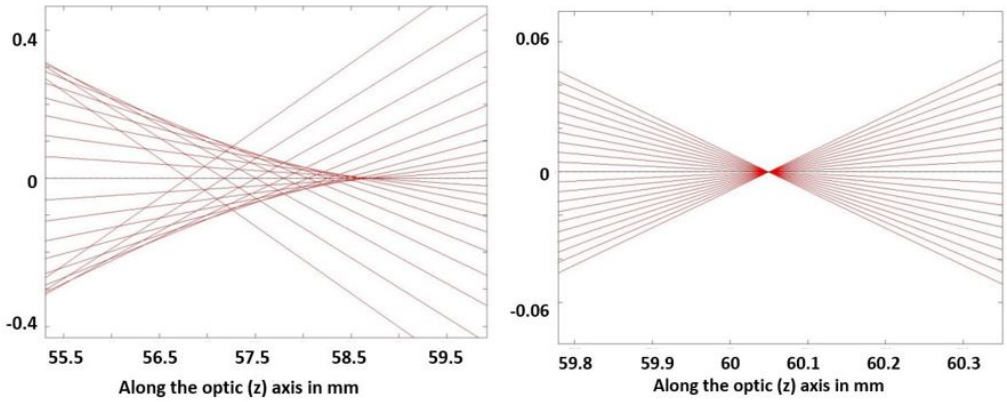

Figure 3.3: Ray tracing results at focal point of A) Plano-convex lens B) Lens-metasurface combination with 'c' correction.

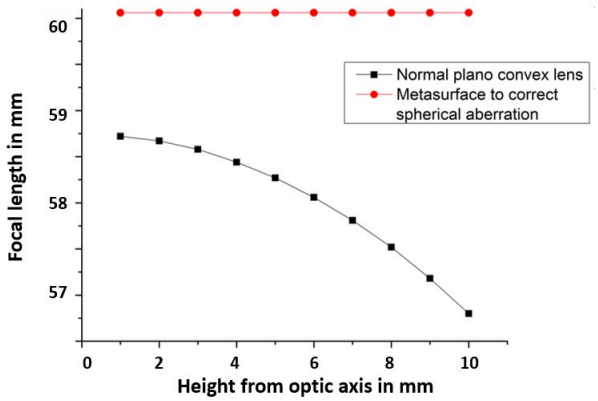

Figure 3.4: Focal point shift comparison for Plano-convex lens and Lens-metasurface combination

Ray tracing analysis is carried out to simulate spherical aberration correction. Again the setup of figure 3.1 is considered with and without metasurface. Here, the metasurface has the phase gradient equal to that calculated from equation 3.15. For the metasurface case, accurate calculation with 'c' correction is considered. Here the lens parameters are radius of curvature of 3 cm, central thickness of 3 mm and focal length f of 60mm. Ray tracing results are shown in figure 3.3 and 3.4. In Figure 3.3, the difference between the focal plane

of lens and lens-metasurface combination case is shown. More sharper focal point can be seen with metasurface depicting the correction of spherical aberration. The quantitative analysis is shown in figure 3.4. By comparing the focal length shifts for both the cases (red and black plots), it can be inferred that the focal length of lens-metasurface combination is nearly constant with respect to the height of the ray which implies mitigation of spherical aberration. It can be noted that the focal length of lens-metasurface combination is higher than the bare lens. This is expected as the phase delay imparted by the metasurface increases with 'r', therefore acts as a diverging lens.

3.2 Large area metasurface fabrication

Typically, dielectric metasurface fabrication is done using electron beam lithography and subsequent steps of development, metal deposition, etching etc. But it is only suitable for micrometer to millimeter scale fabrication and not larger dimensions. Hence, a novel large area fabrication technique was proposed in [8]. Instead of using a dielectric material, a negative resist is used as a constituent material of metasurface. A negative resist is hardened by electron beam lithography and when properly patterned can form the metasurface itself. This significantly reduces the fabrication time as it is effectively a single step process.

In [8], EBL resist maN-2410 (Microresist technology, GmbH) is used for fabrication. It has relatively high refractive index ranging from 1.63 to 1.68 in the visible region. The resist is spin coated on glass substrate and then patterned by single EBL exposure to yield high exposure ratio nanofins functioning as Pancharatnam Berry (PB) phase metasurface. This is described in figure 3.5 where 1 centimeter diameter metalens is fabricated.

For higher aspect ratio nanostructures, a problem was encountered. After development and nitrogen drying, nanofins collapsed onto each other due to surface tension forces. This was avoided by utilizing critical point drying technique by using surfactant-modified hexane as intermediary liquid in the process [9]. With this, it was possible to achieve height to width aspect ratio of 20.

Employing this technique, our collaborators at Chalmer's university from Prof. Michael Kall's group had fabricated 3 different metasurfaces for lens aberration correction. Figure 3.6 shows the PB phase nanopillar dimensions which are optimized for different range of

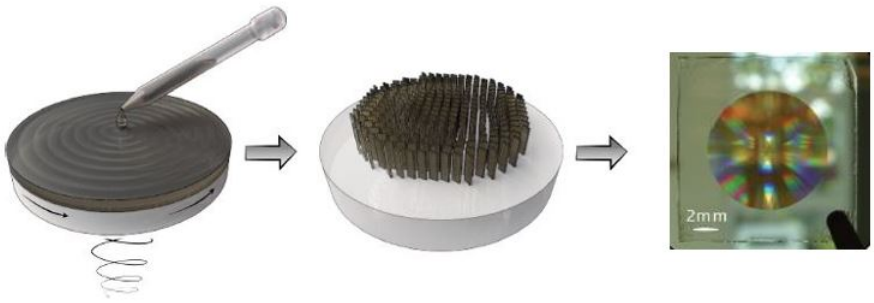

Figure 3.5: Large area metasurface fabrication [8]

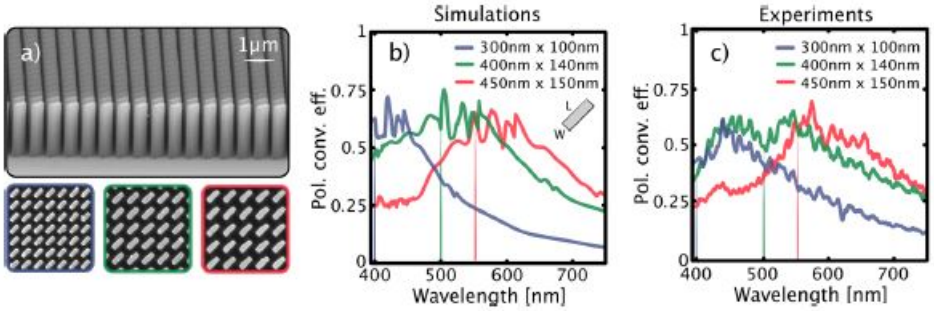

Figure 3.6: a) Scanning Electron Microscopy (SEM) images of fabricated large area metasurface. Polarization conversion efficiency plot of PB metasurface by b) FDTD simulation c) experiment [8]

wavelengths from 400 to 750 nm. Figure a) shows the SEM images of the pillars. Figure b) and c) are the plots from FDTD (Finite Difference Time Domain) simulation and experiment respectively for polarization conversion efficiency as a function of wavelengths for 3 optimized dimensions of nanopillars. Optimization of PB nanopillar dimensions by simulation is discussed in detail in the next chapter for the fabrication of our metasurface.

The fabricated metasurfaces were 1 cm in diameter designed for a plano-convex lens made of fused silica having radius of curvature R=23 mm. Phase delay profile for each of the metasurface is as follows. For Chromatic aberration correction, parameters R, $\lambda_0 = 650nm$, $B = 0.00354m^2$ is substituted in equation 3.12 to obtain,

$$\phi(r) = -3.521 \times r^2 \tag{3.21}$$

where 'r' is in millimeters. The negative sign in the phase delay profile indicates that the phase gradient is pointing away from the center of the metasurface. It is acting as a converging lens compensating for chromatic dispersion of a convex lens, analogous to the case of prism in the previous chapter.

For the case of spherical aberration, the same parameters are followed as that for chromatic aberration. They are substituted in equations 3.19 and 3.20. Here, metasurface is designed for the wavelength $650nm$. The corresponding focal length 'f' and refractive index 'n' for fused silica at this wavelength are 50.3833 mm and 1.4565 respectively. The plano-convex lens used had a central thickness of 2.7 mm and the metasurface substrate thickness was around 0.5 mm. Therefore, the sum of these 2 quantities gives the total central thickness $d_0 = 3.200mm$. We noticed that the phase profile is considerably depended on the precision of quantities R, n, f and d_0. Therefore, the precision of these values was fixed to be 4 decimal places and all lengths were expressed in millimeters. The final phase profile after substituting these values are not shown here as these expressions are quite long. But it has to be noted that we fabricate 2 separate metasurfaces for spherical aberration correction, one for precise values of 'r' (c-correction) and another for approximated values (no c-correction) as shown in equation 3.19 and 3.20.

3.3 Phase measurement

After fabricating large area PB phase metasurfaces as discussed in previous section, spatially varying phase shift along the metasurface was measured. This can be a handy tool to verify the phase and intensity profile of the metasurface. For this purpose, we used SiD4 device from Phasics which works on the principle of Quadriwave Lateral Sheering Interferometry (QWLI) [10]. This device includes Modified Hartmann Grating (MHG) placed infront of a regular CCD camera which generates interferometric pattern.

As the name QWLI suggests, MHG uses 2 dimensional periodic array of square apertures to obtain 4 orders of diffraction which are identical waves[11]. After a few millimeters of propogation, these 4 orders create an interferogram on the detector. From this pattern, phase and amplitude information can be retrieved [12][13]. Phase measurement setup used for our metasurface characterization is as shown in figure 3.7. The box with dotted line represents the Phasics camera in which grating stands for MHG which is placed right infont of a regular

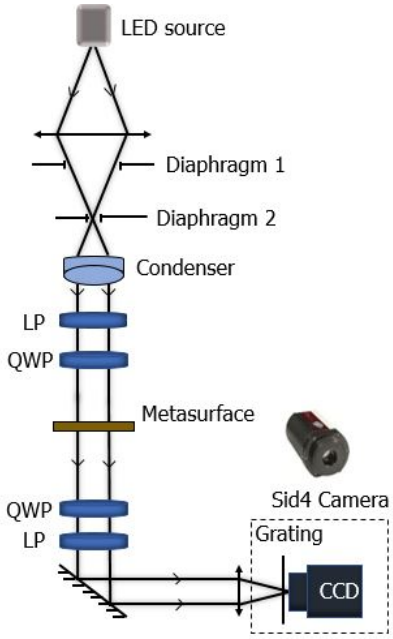

Figure 3.7: Phase measurement setup used for characterizing the metasurfaces. LP-Linear Polarizer, QWP- Quarter Wave Polarizer [10]

CCD. These components are already integrated into Sid4 device. It has a spatial resolution of 29.6 µm (pixel size) and phase (optical path difference) resolution of less than 2 nm. As PB phase metasurfaces are to be characterized, 2 sets of Linear polarizers and Quarter wave plates are used. One pair to obtain incident circular polarization and another at the output to let only cross circular polarization component. The desired PB phase is encoded in the cross polarization term as explained in the equation 1.10 of introduction chapter.

The sample is illuminated using a LED source of 617 nm as coherent light causes speckles which is not convenient for measurement. First, optical path for a clean substrate is measured which serves as the background for actual measurement. After this, the substrate is replaced with the metasurface and it is made sure that whole of the metasurface is illuminated. The waveplates are set to be in cross polarization configuration. The phase and intensity characterization of chromatic aberration metasurface is shown in Figure 3.8 and 3.9. The experimental phase profile was compared with that obtained from equation 3.12 in figure 3.8. The Phasics software shows the phase information as optical thickness which can be converted to phase delay by multiplying with the factor $2\pi/\lambda$. The red curve is the smoothened curve of the phase information along the diameter (radially averaged) of 2 dimensional phase profile

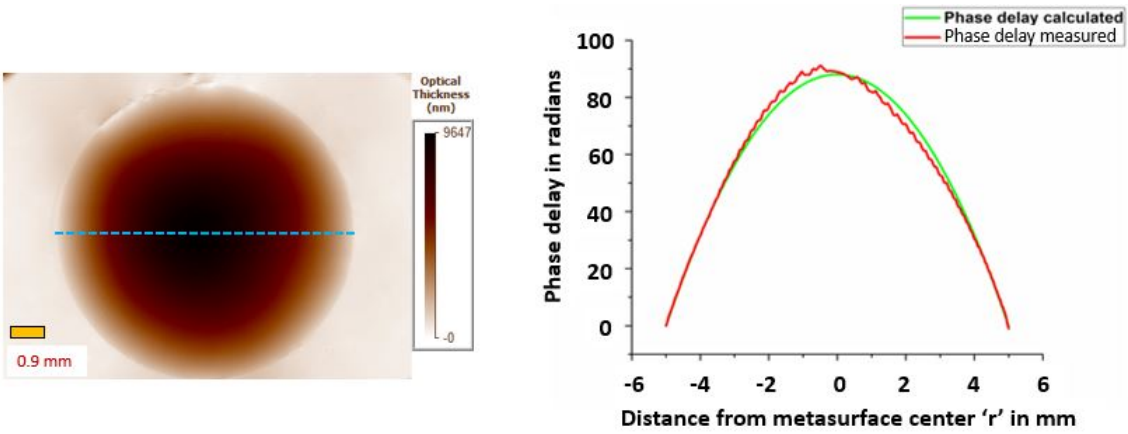

Figure 3.8: Left - Phase delay profile of chromatic aberration correction metasurface. Right - Comparison of cross-section along the blue dotted line in the phase profile. The calculated phase delay profile and measured data are compared.

in figure 3.8. The 2 curves match well with each other confirming that the metasurface fabrication is as desired. In figure 3.9, intensity profile of the metasurface is shown. The profile is supposed to be uniform as the transmission is independent of nanopillar rotation. But from the cross-section profile, it can be noticed as one moves away from the metasurface center, the intensity is varying rapidly as function of variation of phase gradient. This intensity modulation can be attributed to the near field interaction between the pillars of different rotation.

Similarly, phase characterization results of spherical aberration metasurface is shown figure 3.10. Compared to 3.10 B), the phase profile is quite different in A) both qualitatively and quantitatively owing to the approximation of $r \approx r_1$ written as no 'c' correction case. Again a cross section is taken along a diameter of the phase delay profile and plotted. This is compared with the profile calculated from equations 3.19 and 3.20 with 'c' corrected and no 'c' corrected cases respectively. They too agree quite well with the calculated phase profile. It is quite interesting that for chromatic aberration case, the phase profile resembles that of a converging lens whereas for spherical aberration case, it is similar to a diverging lens behaviour. This is also revealed in ray tracing results (figure 3.4) by shift of focal length for each case. The same study is done for other incident wavelengths. As expected we obtain the same phase profile in all the cases but the polarization conversion efficiency varies with the wavelength. In figure 3.11, the intensity profile of both c-corrected and no c-corrected spherical aberration correction metasurface is shown.The cross section of the intensity profile

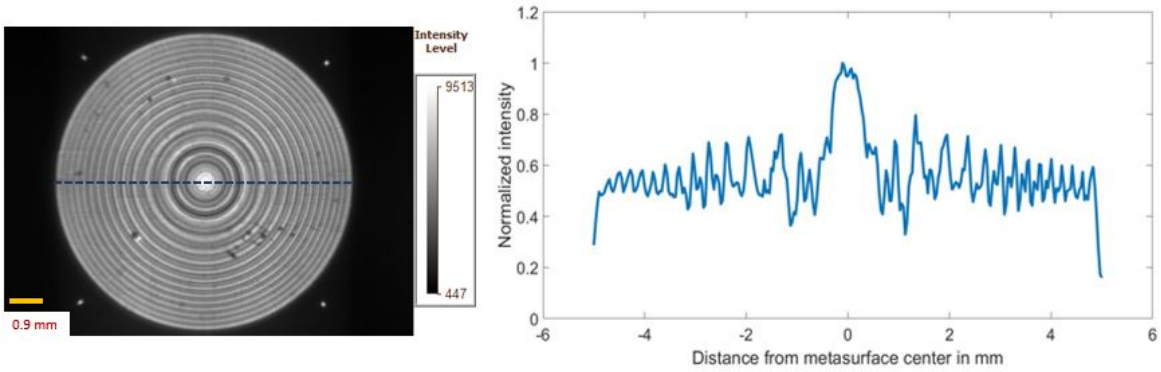

Figure 3.9: Left - Intensity profile of chromatic aberration correction metasurface. Right - The cross-section intensity along the blue dotted line in the intensity profile. It is normalized with respect to the maximum intensity value.

again reveals the presence of near field interaction between the nanopillars.

3.4 Point Spread Function measurement

Consider an infinitely small point source. When it is imaged through an imaging system, at the focal point it is not possible to reproduce the point source. Instead, light waves converge and interfere at the focus to form a 3-dimensional diffraction pattern of concentric rings with central bright spot. The pattern is also called Airy disk and when intensity is plotted as a function of focal plane co-ordinates we get the Point Spread Function (PSF). The resolving power of the imaging system is evaluated by measuring radius of the central bright spot. For example, a higher Numerical Aperture (NA) objective has better resolution as it produces PSF with central bright spot having lower width compared to that from lower NA objective. Even for a perfect imaging system (without aberrations), there is a fundamental limit of resolution set by non-zero width of diffraction peaks known as diffraction limit and such imaging systems are said to be diffraction limited. For example, in the case of microscopes, Abbe's diffraction limit or minimum resolvable distance is given by $\lambda/2NA$, where NA is the Numerical Aperture of the objective lens. Therefore, the obtained image of an object is the convolution of function of true object and the PSF of the imaging system. Conversely, if one knows the PSF of an imaging system, by deconvolution it is possible to mathematically create high resolution image from the captured low resolution image.

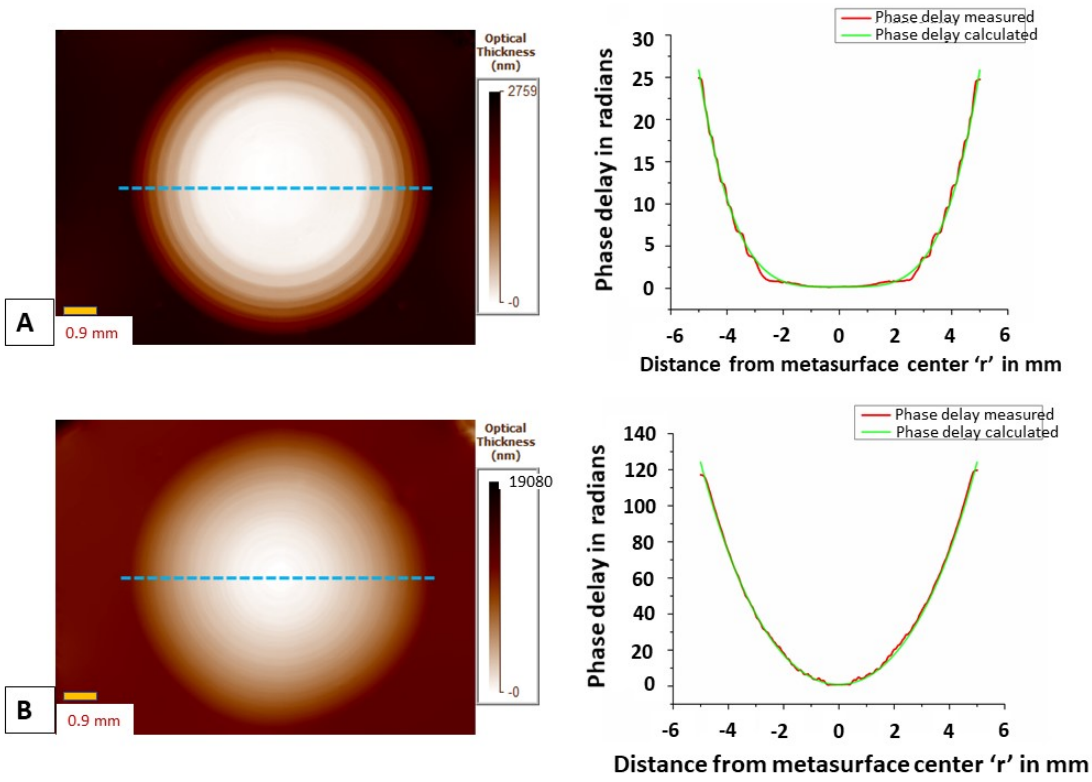

Figure 3.10: Spherical aberration metasurface phase profile for A) No 'c' correction case and B) 'c' correction case. Right - Comparison of cross-section along the blue dotted line in the phase profile. The calculated phase delay profile and measured data are compared.

Consider (x_O, y_O) and (x_I, y_I) to be object and image plane co-ordinates. If 'M' is the magnification due to the imaging system, then they are related as (x_I, y_I)=(Mx_O, My_O). The object plane field can be expressed as weighted Dirac delta function as,

$$O(x_O, y_O) = \int\int O(u, v)\delta(x_O - u, y_O - v)du.dv \tag{3.22}$$

Therefore image plane convolution is calculated as,

$$I(x_O, y_O) = \int\int O(u, v)PSF(x_I/M - u, y_I/M - v)du.dv \tag{3.23}$$

Here PSF is the image when object is a dirac delta function or a point object.

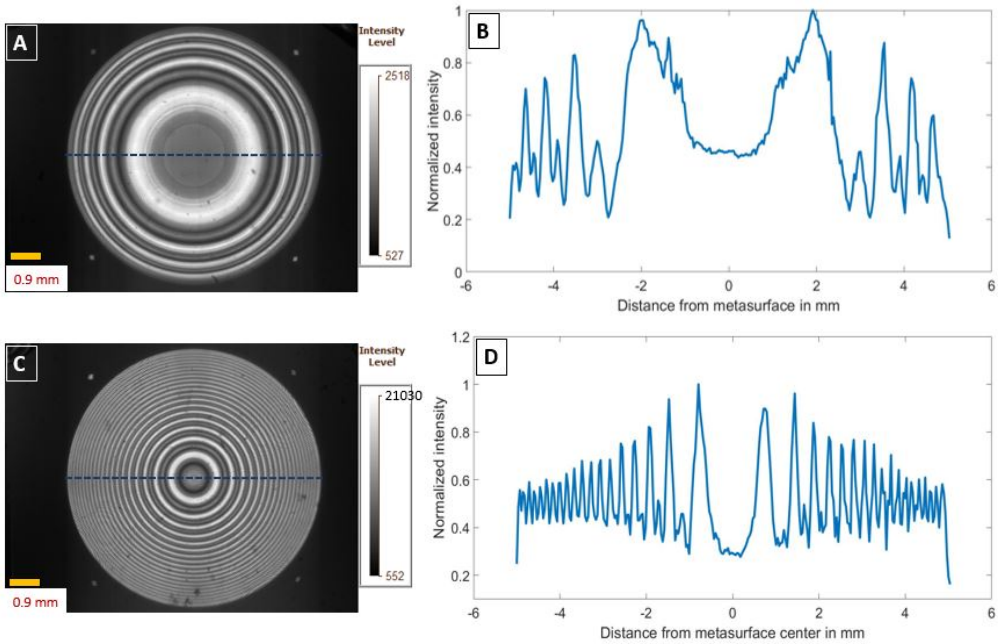

Figure 3.11: A) and C)- Intensity profile of spherical aberration correction metasurface for no k-correction and k-correction case respectively. B) and D) - The cross-section intensity along the blue dotted line in the intensity profileof A) and C) respectively. It is normalized with respect to the maximum intensity value.

Since PSF is an useful tool for measuring aberration in the system, we employed it to characterize the lens-metasurface combination. The home-bulit setup to capture PSF and perform Z-scan is shown in figure 3.12. Here, a pinhole of 5 µm is approximated to be point source for measurements. A convex lens is used to imitate object at infinity condition by placing the pinhole at the lens focus. Since the metasurfaces are PB phase based, again 2 sets of Linear Polarizer (LP) and Quarter Wave Plate (QWP) are used to obtain circularly polarized light at incidence and another to let only cross circular polarized light on to the detector. The focal plane of the lens-metasurface combination is studied using a 40X microscope objective and the image is relayed on to a CCD camera using a tube lens. A tunable super continuum laser used as the source. Desired wavelength was chosen using this but with a minimum possible bandwidth of 10 nm.

Motorized stage with lower limit of translation of a few microns was used to obtain Z-scans of PSF around focal plane controlled by a Labview program. As shown in figure 3.13 a), PSF is plotted in x-y plane for lens-metasurface combination for 650 nm incident light. In this nearly symmetric image, a radial average profile is taken to obtain intensity profile along

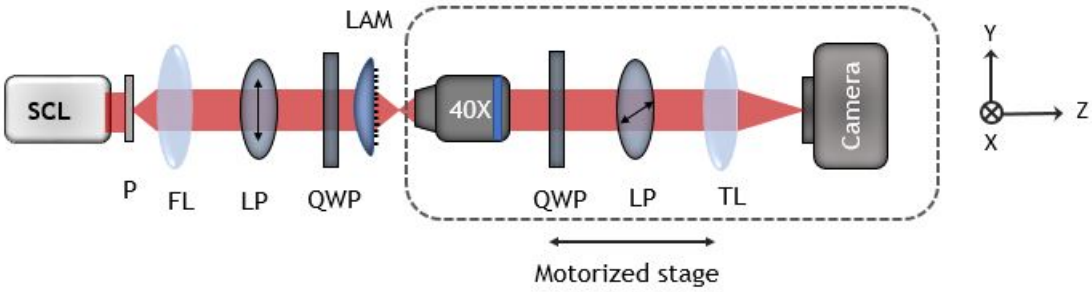

Figure 3.12: Setup to measure PSF and perform Z-scan. The expanded form of each component: SCL-Super Continuum Laser, P-Pinhole, FL-Focusing convex lens, TL -Tube lens, LP-Linear polarizer, QWP-Quarter Wave Plate, LAM-Large Area Metasurface (placed on plano-convex lens)

only one axis instead of x-y plane. This is repeated for PSFs at different z co-ordinates and stacked together to realize z-scan as shown in figure 3.13 b). This profile is quite effective to obtain a qualitative picture of how well the light is confined around the focus.

3.4.1 For Chromatic aberration

We characterize Chromatic aberration of Lens-Chromatic Aberration correction Metasurface(LCAM) combination utilizing the above discussed technique. The z-scans are performed for various incident wavelengths ranging from 600 to 800 nm with intervals of 20 nm. The area around the center of z-scan, as shown in figure 3.13 b) by red dotted line, is chosen and stacked as a function of incident wavelengths. Figure 3.13 c) and d) depicts the characterization for plano-convex lens and LCAM combination respectively. It has to be noted that higher the value along z-axis, more closer is the stage to the lens-metasurface setup. In the case of lens, as expected it exhibits normal chromatic aberration where higher wavelengths have higher focal lengths. As the metasurface is not 100% efficient, it produces many orders of diffraction, most prominent of which are zero and first order. Therefore, there are many foci and one has to carefully identify the first order in which PB phase is encoded. For Chromatic Aberration correction Metasurface (CAM), the first order focal length is lower than the zero order focus by design. When z-scans were performed around this focus, contrary to the lens case, LCAM combination shows quite constant focal length as a function of wavelength indicating mitigation of lens chromatic aberration. By comparing the focal

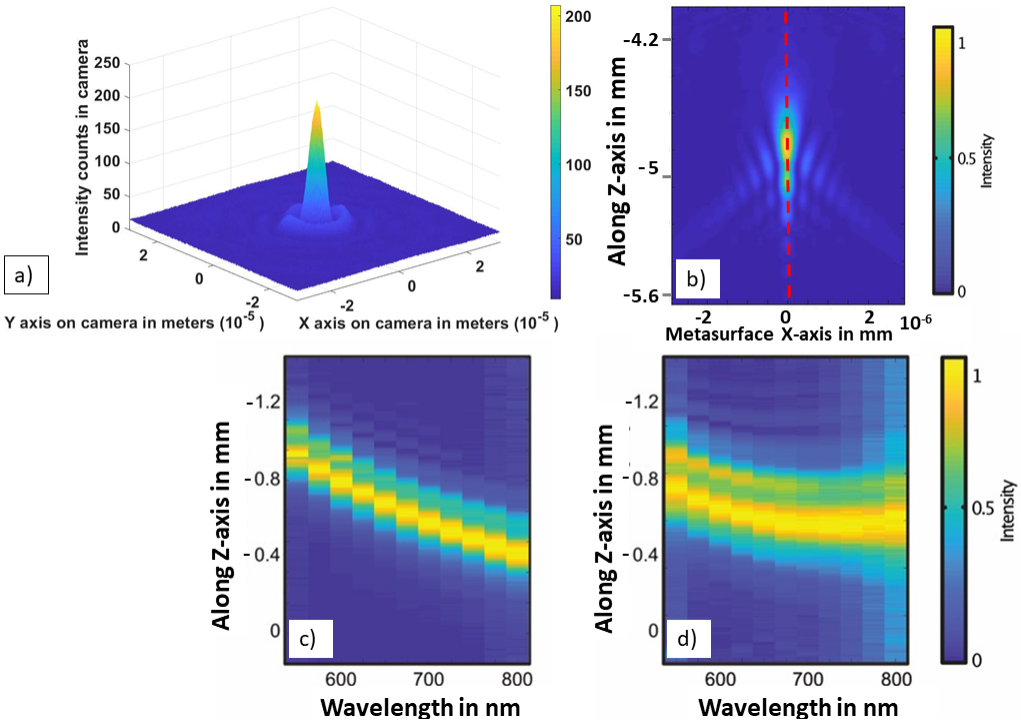

Figure 3.13: PSF and Z-scan results for lens-metasurface combination a) PSF with 650 nm incident light at the focus b) Z-scan measurement for the obtained PSF around the focal plane c) Chromatic aberration characterization of the plano-convex lens by stacking z-scans for different wavelengths ranging from 600 to 800 nm with intervals of 20 nm. The area around red dotted line in b) is chosen for stacking. Intensity is normalized for each wavelength. d) The same study for lens-metasurface combination.

length shifts of both the cases it is inferred that quantitatively around 80% of chromatic aberration is compensated in the range of 600 to 800 nm.

3.4.2 For Spherical aberration

Similar to the previous case, z-scans were performed for Lens-Spherical Aberration correction Metasurface(LSAM) combination. Incident wavelength of 650 nm was used as the metasurface was designed to function at this specific wavelength. For spherical aberration case the first order focal length is higher than the zero order focus by design which is exactly opposite compared to the chromatic aberration correction metasurface.

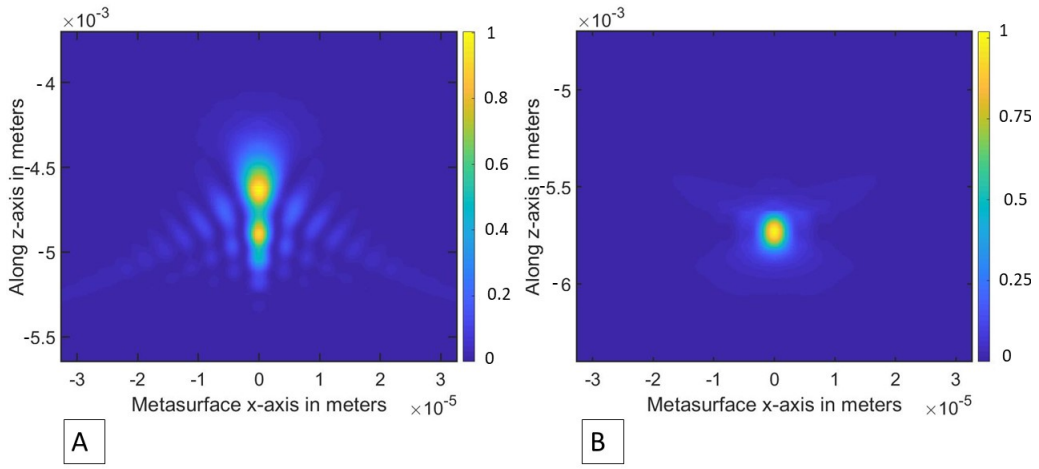

Figure 3.14: Z-scan at 650 nm wavelength for a) Plano-convex lens b) Lens-Spherical aberration correction Metasurface combination

The comparison between z-scans of lens and LSAM combination is shown in figure 3.14. For the case of lens in a), one can notice that the focal point is quite spread out and the intensity profile around the focal plane is quite asymmetric. This pattern indicates positive spherical aberration where rays around the periphery of the lens are bent more compared to rays around the center. Whereas for LSAM in b), the focus is well confined and the profile is relatively symmetric which is a signature of a less aberrated focus. It is not easy to quantify aberration using this study. Therefore, we also calculate Modulation Transfer Function and perform Zernike analysis as discussed in the subsequent sections.

3.5 Modulation Transfer Function study

Modulation Transfer Function(MTF) is a measure of how much of object contrast is transferred to image by the imaging system. It is convenient to define it using equally spaced lines as shown in figure 3.15. For decreasing line spacing or increasing frequency of the object the contrast that the imaging system is able produce decreases naturally. Generally, image contrast percentage versus spatial frequency of the object is plotted to compare MTF of different imaging systems.

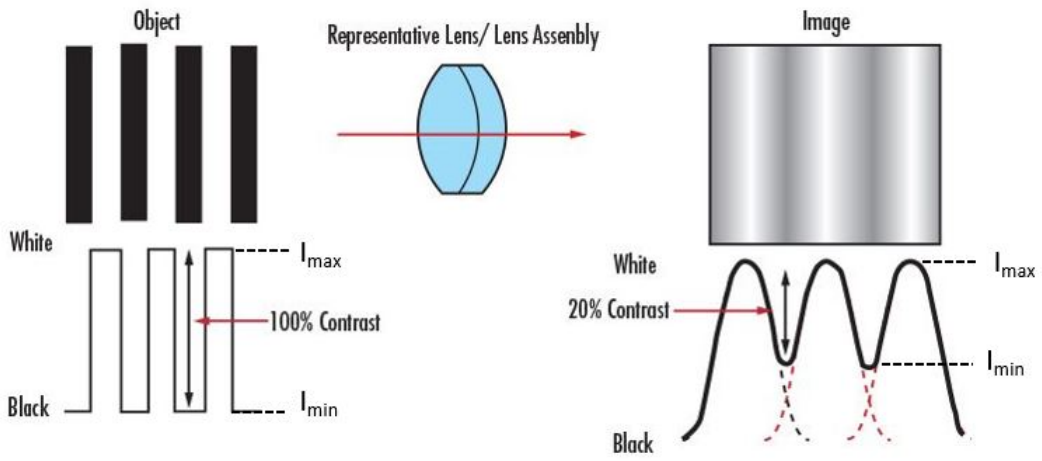

Figure 3.15: A schematic figure to visualize Modulation Transfer Function[14]

MTF is a variant of Optical Transfer Function(OTF) which is a general function to describe how the optical system handles different spatial frequencies. Generally, Optical Transfer Function is a complex-valued function in spatial frequency and is given by the fourier transform of PSF. The absolute value of OTF corresponds to MTF. And the complex argument of OTF is called as Phase Transfer Function (PhTF). Therefore MTF and PhTF are both real valued functions.

$$OTF(k) = MTF(k)e^{iPhTF(k)} \tag{3.24}$$

Also from the image contrast, Modulation can be defined as shown in figure 3.15. This is given by

$$Modulation(M) = \frac{(I_{max} - I_{min})}{(I_{max} + I_{min})} \tag{3.25}$$

Therefore, spatial frequency(k) dependent modulation which is again MTF is given by

$$MTF = \frac{M_{image}(k)}{M_{object}} \tag{3.26}$$

The comparison between MTF of lens and that of LSAM combination is shown in figure 3.16. It is obtained by performing Fast Fourier Transform (FFT) on experimentally obtained PSF at the focal plane. The blue curves in each figures of 3.16 correspond to MTF of

diffraction limited system. It is calculated by considering the lens pupil function as discussed in [15]. Pupil function P(x,y) is the function of aperture of the lens which in our case is a circle of diameter 1 cm. With co-ordinates $\xi = \frac{x}{\lambda f}$ and $\eta = \frac{y}{\lambda f}$, MTF is given by

$$MTF_{diffraction}(\xi, \eta) = \mid \mathcal{F}(\mid \mathcal{F}(P(x, y)) \mid^2) \mid \tag{3.27}$$

f and λ stand for focal length of the lens and wavelength respectively. The symbol $\mathcal{F}$ represents Fourier transform of a function.

Here the cutoff frequency f_c is defined as for all $k > f_c$, the contrast is equal to zero. The cutoff frequency for a diffraction limited system is given by $f_c = \frac{1}{\lambda \times (\frac{f}{D})}$ [16]. Here λ is the incident light wavelength and the ratio $\frac{f}{D}$ is known as f-number of an ideal lens where 'f' is its focal length and 'D' the diameter of its aperture. Similarly, the spatial frequency of a camera is defined as $f_{camera} = \frac{M}{p}$ where 'M' is the magnification of the imaging system and 'p' is the pixel size of the camera. To study the MTF of a lens using a camera and magnifying optics with magnification 'M', it is required that $f_c < f_{camera}$ [17]. If this condition is not satisfied then the PSF of a point source is confined to only one pixel of the camera and hence the details cannot be studied. In our case, f=5.04 cm and D=1 cm for the plano-convex lens used in the setup for λ=650 nm. With these values, the cutoff frequency f_c is found to be 0.305 line pairs/µm as seen in figure 3.16 A) and B). For the case of LSAM, from the design of the metasurface the focal length increases to 5.27 cm. With 'D' and λ being the same as previous case, the cutoff frequency for this case is found to be f_c'=0.291 line pairs/µm as shown in figure 3.16 C) and D). In the setup, Thorlabs CMOS camera is used whose pixel dimensions are 5.2 µm X 5.2 µm. As shown in figure 3.12, the optics on the motorized stage imparts magnification of 40X to the image. Therefore with p=5.2 µm and M=40 we get f_{camera}=7.692 line pairs/µm. Therefore, it is verified that $f_c < f_{camera}$ and $f_c' < f_{camera}$. Instead of magnification factor of 40, if M=1 is used, we get f_{camera}=0.192 which is less than f_c and f_c'. This justifies the utilization of extended optics to magnify the PSF.

As the focal length of plano-convex lens and LSAM combination have different focal lengths of 5cm and 5.23 cm respectively, they have different $MTF_{diffraction}$. The experimentally calculated MTFs are compared with their corresponding $MTF_{diffraction}$ for plano-convex lens in figure 3.16 A), B) and for LSAM combination in figure 3.16 C), D). At lower frequencies, the difference between the two cases is not huge. But at frequencies higher than

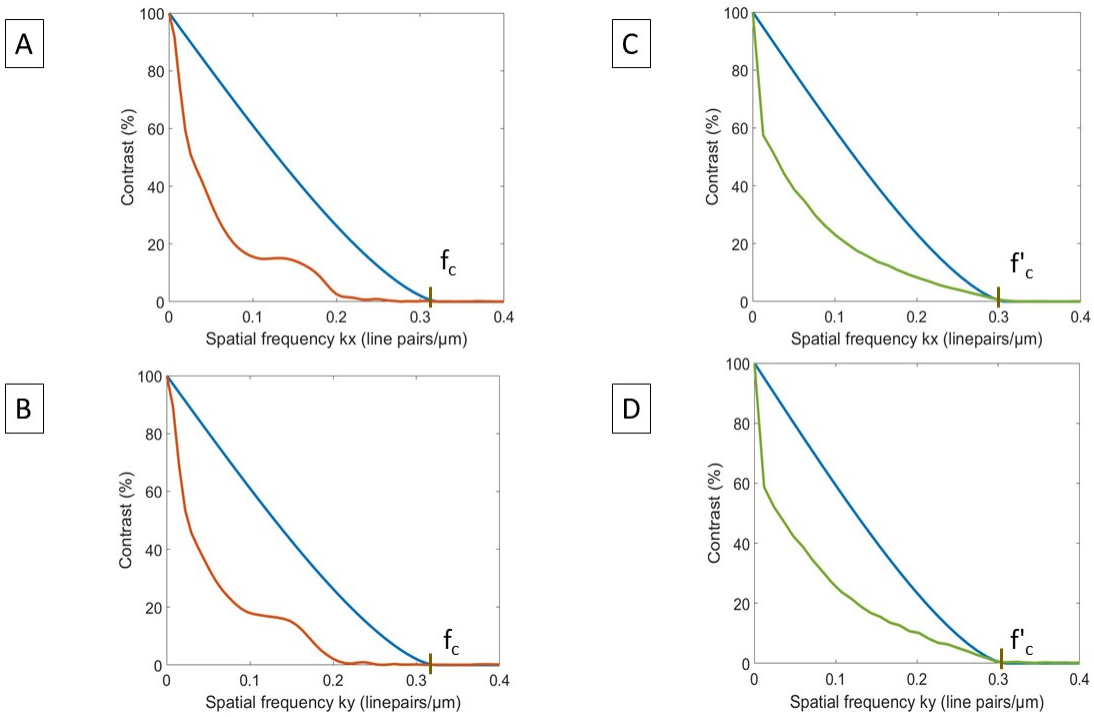

Figure 3.16: MTF for plano-convex lens in A) and B) along k_x and k_y axis respectively (red curve). Similarly, MTF for LSAM combination in C) and D) (green curve). In all the figures, blue curves correspond to diffraction-limited MTF.

0.2 line pairs/μm, better contrast with LSAM combination over the plano-convex lens is evident. This can be attributed to Spherical aberration correction.

3.6 Zernike analysis

By expressing wavefront in a polynomial form one can study aberrations in a comprehensive manner[18]. Often, Zernike polynomials are employed for this purpose as they are composed of terms which have similar form as the types of aberrations normally found in the optical systems.

Zernike polynomials in circular basis are defined over a circle of unit radius. For polar co-ordinates (r,ϕ), even Zernike polynomials can be defined as $Z_n^m(r,\phi) = R_n^m(r)\cos(m\phi)$. Whereas odd Zernike polynomials are given by $Z_n^m(r,\phi) = R_n^m(r)\sin(m\phi)$. Where n≥m≥0,

ϕ is the azimuthal co-ordinate and r is the radial co-ordinate with 0≤r≤1. It also satisfies the condition $\mid Z_n^m(r,\phi) \mid \leq 1$. The radial component is given by

$$R_n^m(r) = \sum_{k=0}^{\frac{n-m}{2}} \frac{(-1)^k (n-k)!}{k!(\frac{n+m}{2}-k)!(\frac{n-m}{2}-k)!} r^{n-2k} \tag{3.28}$$

when (n-m) is even and 0 when (n-m) is odd. An important property of Zernike polynomials is their orthogonality. When integrated over a unit disc it is given by

$$\int Z_n^m(r,\phi) Z_{n'}^{m'}(r,\phi) d^2r = \frac{\epsilon_m \pi}{2n+2} \delta_{m,m'} \delta_{n,n'} \tag{3.29}$$

Here ϵ_m is equal to 2 if $m = 0$ and equal to 1 if $m \neq 0$. Also $\delta_{m,m'} = 1$ if $m = m'$ and equal to 0 otherwise. It is also the same for $\delta_{n,n'}$.

This property signifies that Zernike polynomials are independent of each other and using them each aberration can be quantified independently. The deviation of a given wavefront from the ideal wavefront is given by W(r,ϕ) which can expressed in terms of Zernike polynomials as follows [19]

$$W(r,\phi) = \sum_{n=0}^{\infty} \sum_{m=0}^{n} C_{nm} N_n^m R_n^m(r) A_n^m(\phi) \tag{3.30}$$

Here R_n^m and A_n^m are the radial and angular components of zernike polynomials respectively as mentioned before. N_n^m is the normalization factor obtained from orthogonality condition of equation 3.29. The term C_{nm} is the zernike co-efficient associated with the order of aberration n,m. Therefore error from a given wavefront can be fit to zernike polynomials series using zernike co-efficients. Through this, each aberration of the wavefront can be independently quantified.

We employ Zernike analysis to quantify spherical aberration correction from the metasurface. It was experimentally performed using the phase measurement setup which is same as in figure 3.7. The only difference being here lens and lens-metasurface combination is imaged instead of bare metasurface. The outgoing wavefront is analysed using Zernike analysis tool of Phasics software. Circular mask or pupil of size approximately 7.5 mm in diameter is used.

It is crucial to keep the mask size constant as the Zernike co-efficients heavily depend on it. The resulting zernike co-efficients are as shown in figure 3.17. Here the 'defocus' component is set to zero and 'piston' aberration is not shown. As discussed in [20], the defocus for this case is nothing but the phase profile of an ideal lens, therefore it can be subtracted. Piston component is a constant added to the optical path and just shifts the position of the focal point. Therefore it is not a true optical aberration and hence can be neglected.

The study was performed with 617 nm LED illumination which is close to the design wavelength for Spherical Aberration correction Metasurface (SAM). The optical thickness and corresponding Zernike co-efficients are shown in figure 3.17 for both plano-convex lens and LSAM combination. It can be noticed from the color bars of figure 3.17 A) and C) that the optical thickness is significantly lower LSAM compared to the lens. For the case of lens in figure 3.17 B), one can see that the major aberration is spherical aberration. Figure 3.17 D) is the result for LSAM for cross-polarized component in which PB phase is encoded. One can notice that the spherical aberration of the system is drastically reduced in this case. Quantitatively, at least 70% of the spherical aberration is mitigated with the metasurface. However, both the Tetrafoil aberrations seem to shoot up with the metasurface. But as it is a higher order aberration, it doesn't contribute much to the overall imaging quality as shown in subsequent section. When the plano-convex lens is replaced by the LSAM in the setup, it is possible that the alignment is slightly different compared to the lens case. Therefore, to verify this, we also analyse the co-polarized component of LSAM as shown in figure 3.18 A). The co-polarized component is nothing but the zero order of diffraction which is not affected by the phase profile imparted by the metasurface. The similarity between figure 3.17 B) and 3.18 A) ensures that the alignment is not very different for both the cases. Figure 3.18 B) is the analysis result for combination of lens and no c-correction SAM. It mitigates spherical aberration only by around 25%. Much better performance of c-corrected metasurface (Figure 3.17 d)) over no c-corrected metasurface (Figure 3.18 b)) in spherical aberration correction can be seen. This supports the fact that accurate calculations are crucial in spherical aberration correction metasurface design. It has to be noted that both c-corrected and no c-corrected metasurface mitigates also both the Coma aberrations of lens from figure 3.17 and 3.18 d).

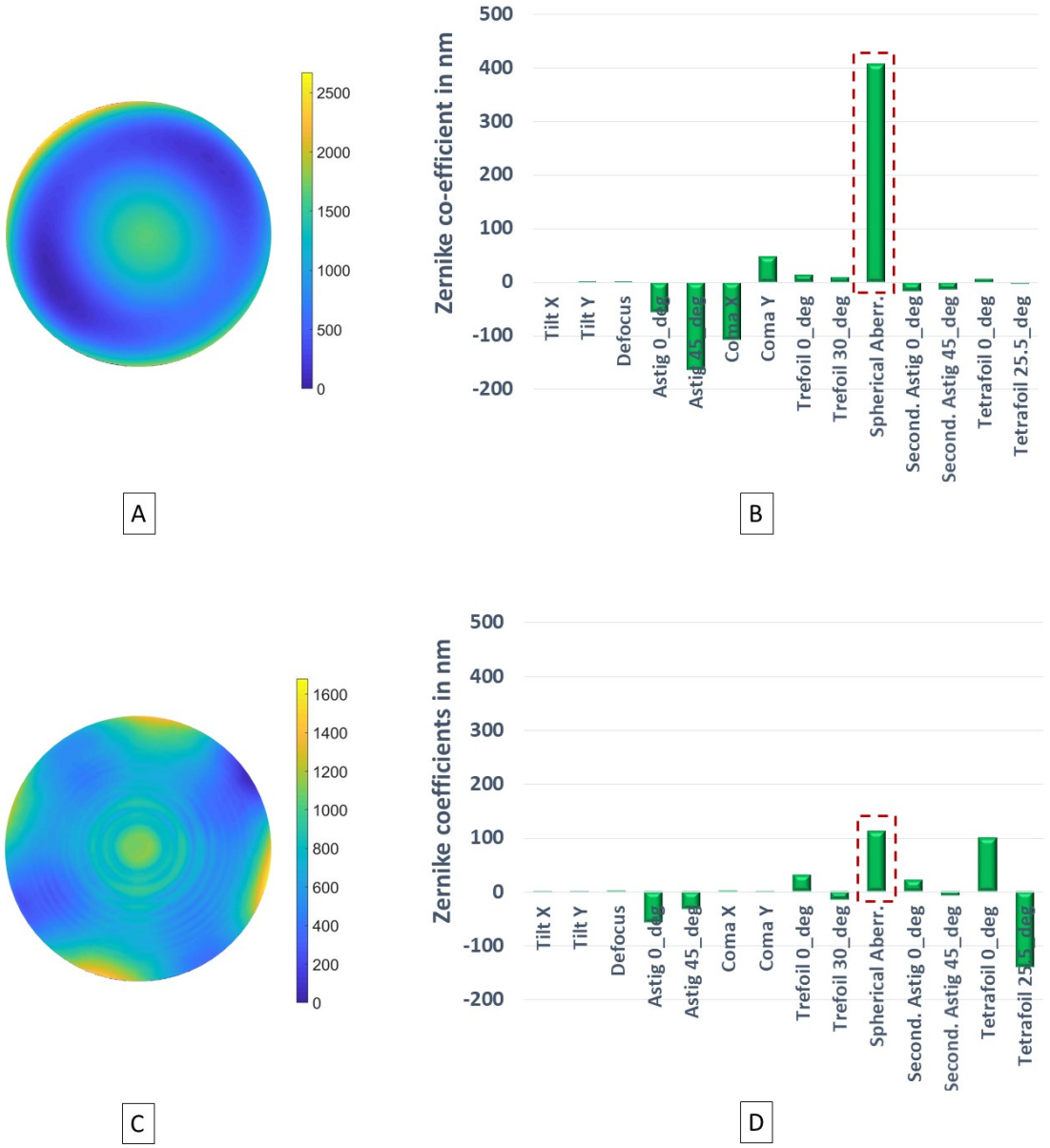

Figure 3.17: A) Optical thickness and B) Zernike co-efficients measured on phase measurement setup for the Plano-convex lens. C) and D)- The same measurements for LSAM combination (c-corrected) for cross-polarization component. Defocus is subtracted in both the cases. Aberration name in the same order as in the figures - Tilt X, Tilt Y, Defocus (=0), Astigmatism 0°, Astigmatism 45°, Coma X, Coma Y, Trefoil 0°, Trefoil 30°, Spherical aberration, Secondary astigmatism 0°, Secondary astigmatism 45°, Tetrafoil 0°, Tetrafoil 25.5°

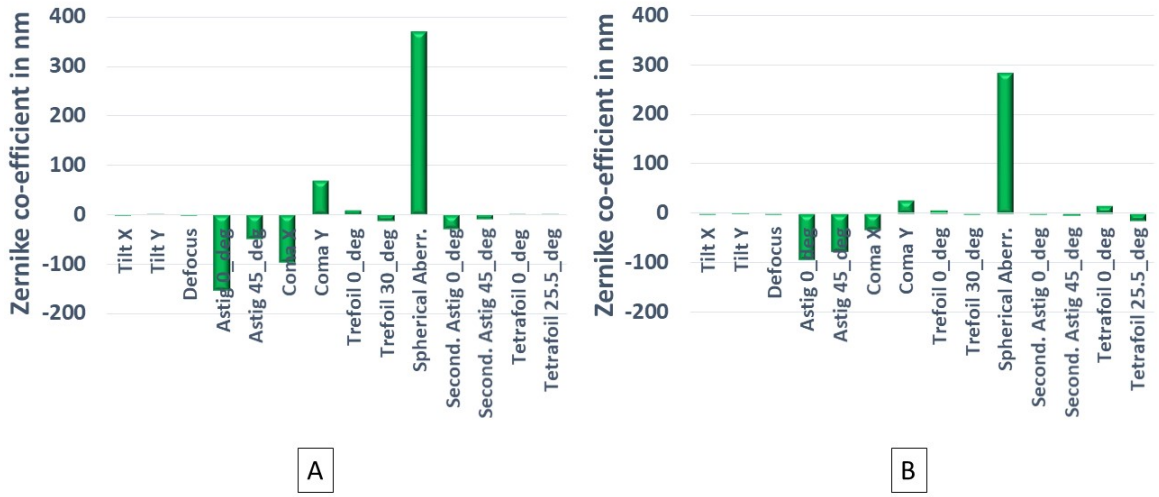

Figure 3.18: Zernike co-efficients measured on phase measurement setup for A) LSAM combination for co-polarization component B) Lens and no c-correction Spherical aberration correction metasurface combination for cross polarization component.

3.7 Imaging

To assess the performance of the metasurfaces, imaging of 1951 US Air Force (USAF) resolution target was performed. The setup as shown in figure 3.19 was used for imaging the standard target plate with the lens-metasurface combination. Figure 3.20 shows the comparison between images from a normal plano-convex lens and LSAM combination. Here illumination is chosen to be at 650 nm in the supercontinuum setup with a bandwidth of 10 nm (least possible). Again for LSAM combination cross polarization component is chosen to avoid the background light and to obtain only the corrected image. Much better resolution of figure 3.20 b) over a) again proves that the significant amount of spherical aberration is mitigated. The visibility of smaller structures in the bottom panel is low owing to relatively low polarization conversion efficiency of the metasurface but the difference caused by the metasurface is clear.

Figure 3.21 shows the imaging result for chromatic aberration correction. Here broadband light of 550-800 nm from the supercontinuum source is used for illumination. The images

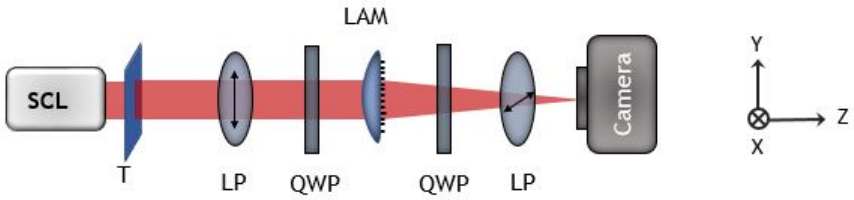

Figure 3.19: Setup to perform imaging of a target. The expanded form of each component: SCL-Super Continuum Laser, T-Target, LP-Linear polarizer, QWP-Quarter Wave Plate, LAM-Large Area Metasurface (placed on plano-convex lens)

are captured with Thorlabs Zelux CMOS color camera (1.6 MP) by removing the IR filter already present in the camera. Above 750 nm wavelength, the light is color coded as magenta (Red+Blue) in the camera. Comparison between figures 3.21 a) and b) shows that the images with LCAM combination are much sharper than that with the plano-convex lens for group 2 and 3 elements of USAF target. Again because of relatively low polarization conversion efficiency of the metasurface, the signal to noise ratio is not very high owing to other orders of diffraction from the metasurface. It has to be noted that even though the chromatic aberration is corrected with the metasurface in the wavelength range of 550-800 nm, the spherical aberration is still present in the system.

One can argue that lens-CAM-SAM combination should mitigate both spherical as well as chromatic aberration simultaneously. Unfortunately here it is not the case as CAM adds some amount of spherical aberration and SAM adds also chromatic aberration to the system. But it is possible that for some design parameters the SAM and CAM compound system might correct both Spherical and Chromatic aberration of the lens. In this thesis we haven't investigated in this direction.

3.8 Conclusion

In this chapter, a systematic discussion is carried out as to how a metasurface can be designed to correct lens aberrations. Through detailed experimental studies it is shown that indeed significant amount of lens aberration is mitigated. The essence of this chapter is that instead of using a refractive component like an objective lens or diffractive component like a metalens,

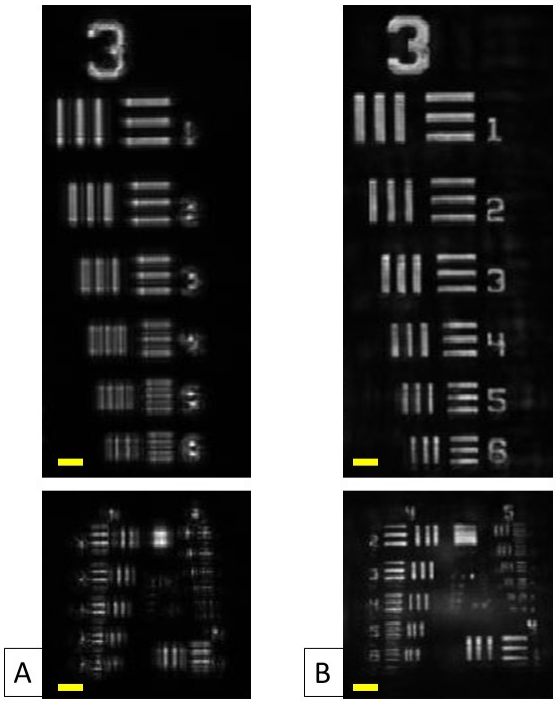

Figure 3.20: Imaging of USAF target with A) Plano-convex lens B)LSAM combination. Scale bar in top panel corresponds to 35 µm, bottom panel corresponds to 28 µm

advantages of both of them is combined in the form of hybrid lens-metasurface to achieve aberration free imaging. Even though metacorrectors have been discussed in some works, the novelty of this work lies in the fact that the design of metasurface is convenient for large area devices. This factor pushes the metasurface a step closer to practical applicability. In a standard objective lens, several lenses and different types of glasses are utilized to achieve aberration free imaging for wavelengths from violet to near infrared. One can imagine that just a lens-metasurface combination replacing an objective lens results in orders of magnitude miniaturization and paves the way for realizing ultra-compact optical devices. This work is a step towards this objective; with optimized design of metasurface we believe that it is possible in future.

It is important to ponder upon the limitations of these metasurfaces as it gives a future direction for improvement. One of the major limitations is the relatively low polarization conversion efficiency of 20%. This can be dealt with by choosing appropriate material which should also be suitable for large area fabrication. Another drawback is that one needs 2 sets of linear polarizers and quarter wave plates to extract the PB phase component from

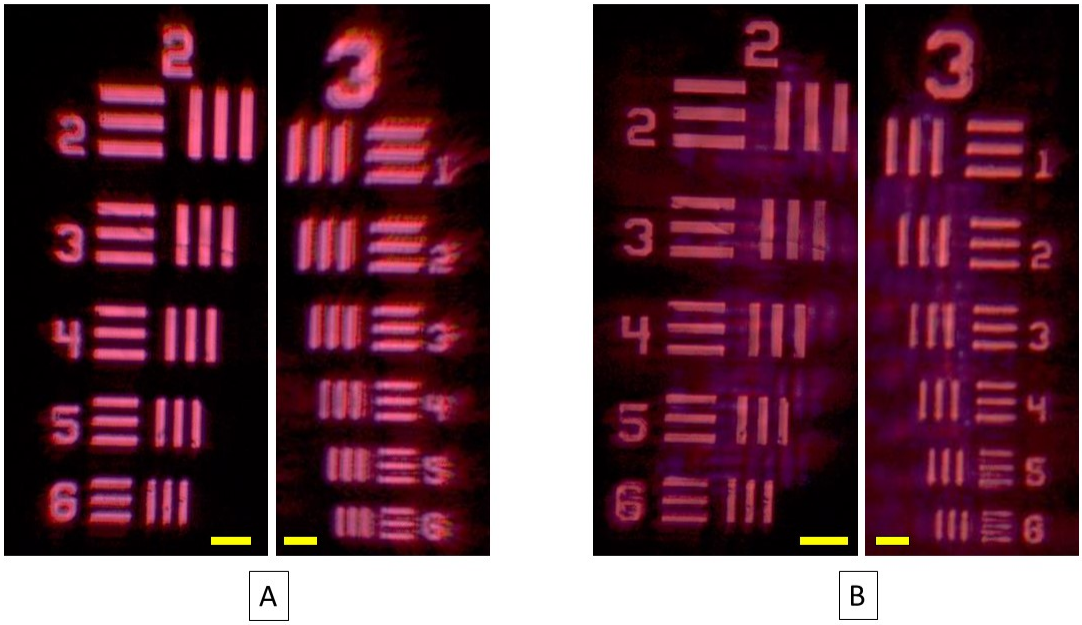

Figure 3.21: Imaging of USAF target with A) Plano-convex lens B)LCAM combination. Scale bar in group 2 panel corresponds to 70 µm, group 3 panel corresponds to 35 µm

the metasurface. One solution to achieve 'standalone' metasurfaces is to design properly optimized propagation phase metasurfaces which can be polarization independent. Also instead of two metasurfaces combining the functionality of spherical aberration and chromatic aberration correction in one metasurface is a way forward [5].

Bibliography

[1] Sajan Shrestha, Adam C Overvig, Ming Lu, Aaron Stein, and Nanfang Yu. Broadband achromatic dielectric metalenses. *Light: Science & Applications*, 7(1):85, 2018.

[2] Wei Ting Chen, Alexander Y. Zhu, Vyshakh Sanjeev, Mohammadreza Khorasaninejad, Zhujun Shi, Eric Lee, and Federico Capasso. A broadband achromatic metalens for focusing and imaging in the visible. *Nature Nanotechnology*, 13(3):220–226, 2018.

[3] Wei Ting Chen, Alexander Y. Zhu, Jared Sisler, Yao Wei Huang, Kerolos M.A. Yousef,

Eric Lee, Cheng Wei Qiu, and Federico Capasso. Broadband Achromatic Metasurface-Refractive Optics. *Nano Letters*, 18(12):7801–7808, 2018.

[4] Chenglong Hao, Shecheng Gao, Qifeng Ruan, Yuanhua Feng, Ying Li, Joel K.W. Yang, Zhaohui Li, and Cheng Wei Qiu. Single-Layer Aberration-Compensated Flat Lens for Robust Wide-Angle Imaging. *Laser and Photonics Reviews*, 14(6):1–10, 2020.

[5] Amir Arbabi, Ehsan Arbabi, Seyedeh Mahsa Kamali, Yu Horie, Seunghoon Han, and Andrei Faraon. Miniature optical planar camera based on a wide-angle metasurface doublet corrected for monochromatic aberrations. *Nature Communications*, 7:13682, nov 2016.

[6] Rajath Sawant, Purva Bhumkar, Alexander Y Zhu, Peinan Ni, Federico Capasso, and Patrice Genevet. Mitigating Chromatic Dispersion with Hybrid Optical Metasurfaces. *Advanced Materials*, 31(3):1805555, jan 2019.

[7] Maria Ruiz-gonzalez. Good Educational for Ray Tracing.

[8] Daniel Andrén, Jade Martínez-Llinàs, Philippe Tassin, Mikael Käll, and Ruggero Verre. Large-Scale Metasurfaces Made by an Exposed Resist. *ACS Photonics*, 7(4):885–892, apr 2020.

[9] Dario L Goldfarb, Juan J de Pablo, Paul F Nealey, John P Simons, Wayne M Moreau, and Marie Angelopoulos. Aqueous-based photoresist drying using supercritical carbon dioxide to prevent pattern collapse. *Journal of Vacuum Science & Technology B: Microelectronics and Nanometer Structures Processing, Measurement, and Phenomena*, 18(6):3313–3317, nov 2000.

[10] Samira Khadir, Pierre Bon, Dominique Vignaud, Elizabeth Galopin, Niall McEvoy, David McCloskey, Serge Monneret, and Guillaume Baffou. Optical Imaging and Characterization of Graphene and Other 2D Materials Using Quantitative Phase Microscopy. *ACS Photonics*, 4(12):3130–3139, dec 2017.

[11] J. C. Chanteloup. Multiple-wave lateral shearing interferometry for wave-front sensing. *Applied Optics*, 44(9):1559–1571, 2005.

[12] Samira Khadir, Daniel Andrén, Patrick C Chaumet, Serge Monneret, Nicolas Bonod, Mikael Käll, Anne Sentenac, and Guillaume Baffou. Full optical characterization of single nanoparticles using quantitative phase imaging. *Optica*, 7(3):243–248, 2020.

[13] Pierre Bon, Guillaume Maucort, Benoit Wattellier, and Serge Monneret. Quadriwave lateral shearing interferometry for quantitative phase microscopy of living cells. *Optics Express*, 17(15):13080–13094, 2009.

[14] Introduction to modulation transfer function @ www.edmundoptics.fr.

[15] G Boreman. Modulation Transfer Function in Optical and Electro-Optical Systems. 2001.

[16] B E A Saleh and M C Teich. *Fundamentals of Photonics*. Wiley Series in Pure and Applied Optics. Wiley, 2019.

[17] Aline Vernier, Baptiste Perrin, Thierry Avignon, Jean Augereau, and Lionel Jacubowiez. Measurement of the modulation transfer function (MTF) of a camera lens. In *Education and Training in Optics and Photonics*, page TPE28. Optical Society of America, 2015.

[18] Vasudevan Lakshminarayanan and Andre Fleck. Zernike polynomials: a guide. *Journal of Modern Optics*, 58(7):545–561, 2011.

[19] zernike_aberrations @ www.telescope-optics.net.

[20] Samira Khadir, Daniel Andrén, Ruggero Verre, Qinghua Song, Serge Monneret, Patrice Genevet, Mikael Käll, and Guillaume Baffou. Metasurface optical characterization using quadriwave lateral shearing interferometry, 2020.

Chapter 4

Metasurface for Quantum Optics applications

In recent years, tremendous progress has been made in the field of quantum technologies. This brings us more closer to realizing something revolutionary as a realistic quantum computer. Most widely used systems to study quantum principles are cold atoms and single photons. Single photons states are relatively convenient to generate, manipulate and measure.

Until the end of 19th century light was thought to be as waves. But in the early 20th century, to explain the photoelectric effect, Einstein proposed a revolutionary theory of light as discrete packets of energy called 'quanta'. This gave birth to the concept of wave-particle duality of matter which also laid the foundation for quantum mechanics. This implies that light can exhibit properties of both wave as well as particles depending on the measurement. Therefore to access the particle aspect of light one needs to deal with single photons.

4.1 Photon statistics

With the advent of ultrafast photodetectors it is possible to study photon statistics of even single photons [1]. A click detector, similar to a Geiger counter, when struck by a single photon produces a short electric pulse in response to an absorbed photon. The counting

electronics connected to the detector registers the number of electric pulses within a defined time period 'T' (Figure 4.1 B). Consider a total of 'N' number of photons are incident on a detector for a time period of 'T'. When the counting is done within a time interval of 't' for $n = \frac{T}{t}$ number of intervals, a photon distribution depending on the nature of light source is obtained. In other words, even though the average photons in each interval is the same (N/n), the variance of the distribution can be different for different sources as shown in figure 4.1 A).

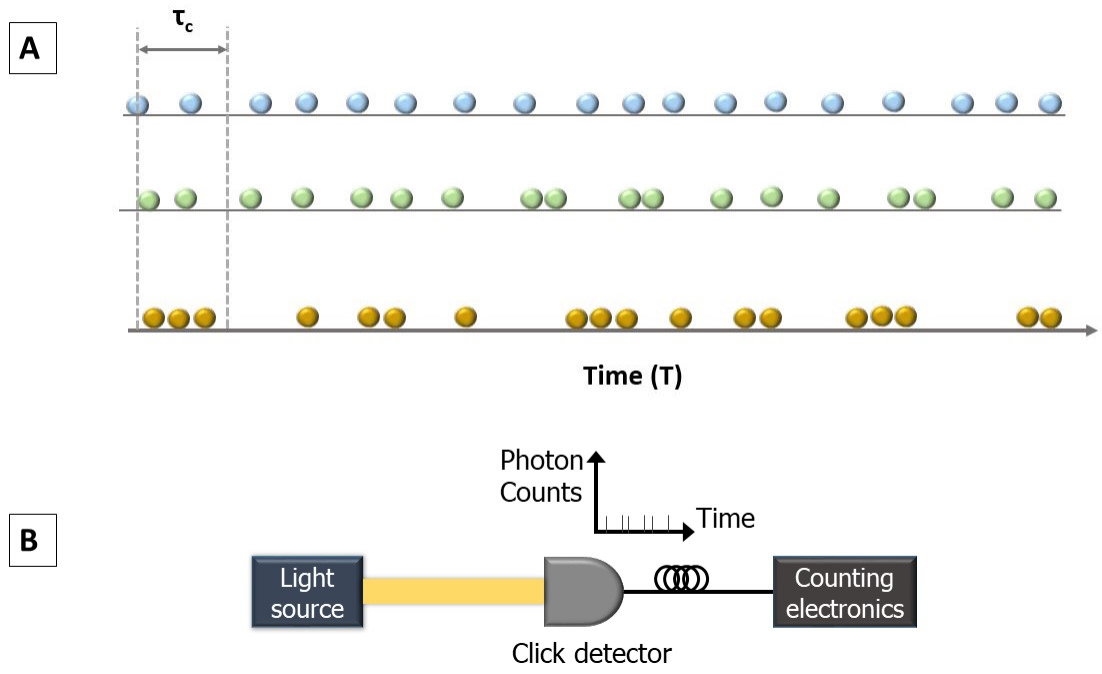

Figure 4.1: A) Spheres in Blue, Green and Yellow color correspond to photon detection as a function of time for antibunched photons, random light (coherent state) and bunched photons respectively. Here 'τ_c' stands for coherence time. B) Schematic of a click detector for single photon counting.

Depending on photon statistics, light can be classified into three types namely bunched photons, random photons and antibunched photons. A coherent light source such as a laser yields Poissonian photon statistics which means that the photons are randomly placed which results in random light. Thermal light has super Poissonian behaviour which is a result of bunching of photons. On the other hand, single photon sources are antibunched which exhibit sub Poissonian statistics.

It is convenient to apply photon statistics utilizing photon number operator $\hat{n}$. This is because the Fock states $|n\rangle$ are eigen states of number operator which is discussed in detail in [2] [3].

$$\hat{n_i} |n_i\rangle = n_i |n\rangle \tag{4.1}$$

Here the eigenvalue n_i of photon number operator gives the number of photons in a specific mode 'i'.

As discussed in [3][4], photons from a coherent light source show the following statistics, where Variance V is given by

$$V = \langle n^2 \rangle - \langle n \rangle^2 = (\Delta n)^2 = \langle n \rangle \tag{4.2}$$

As variance of the distribution is equal to its mean, it represents Poissonian distribution.

An incoherent light source produces photons with random intensity fluctuations. This gives rise to super Poissonian distribution.

$$V = (\Delta n)^2 = \langle n \rangle + \langle n \rangle^2 > \langle n \rangle \tag{4.3}$$

As expected here the variance is invariably greater than the mean of the distribution.

On the other hand, one can say that a stream of photons are single photons when they follow this condition.

$$V = (\Delta n)^2 < \langle n \rangle \tag{4.4}$$

This is nothing but sub-Poissonian distribution. This cannot be explained with classical electromagnetic theory, hence it is called non-classical light or Quantum light.

4.1.1 Degree of coherence

Another statistical quantity often used to express the photon statistics are correlation functions. Degree of coherence is the normalized correlation of electric fields. First order coherence $g^{(1)}$ quantifies electric field fluctuations whereas second order coherence measures

intensity fluctuations of two fields.

Degree of first order coherence for electric fields E_1 and E_2 for time delay of τ between each other can be defined as,

$$g^{(1)}(\tau) = \frac{\langle E_1^*(t)E_2(t+\tau)\rangle}{\sqrt{\langle \mid E_1(t) \mid^2\rangle\langle \mid E_2(t+\tau) \mid^2\rangle}} \tag{4.5}$$

It is an useful quantity in optical interferometry. The visibility of an interference pattern ν of two electric fields with equal intensities is given by the absolute value of $g^{(1)}$. The visibility varies from 0 for incoherent light to 1 for coherent light.

Similarly, the degree of second order coherence is defined as follows. It is the intensity analogue of $g^{(1)}$. $g^{(2)}$ is intensity-intensity correlation whereas $g^{(1)}$ is amplitude-amplitude correlation.

$$g^{(2)}(\tau) = \frac{\langle E_1^*(t)E_2^*(t+\tau)E_2(t+\tau)E_1(t)\rangle}{\langle E_1^*(t)E_1(t)\rangle\langle E_2^*(t)E_2(t+\tau)\rangle}$$

$$g^{(2)}(\tau) = \frac{\langle I_1(t)I_2(t+\tau)\rangle}{\langle I_1(t)\rangle\langle I_2(t+\tau)\rangle} \tag{4.6}$$

For classical light, it can be written in the form of intensities I_1 and I_2.Since intensity of light is proportional to number of photons, $g^{(2)}$ can also be written in terms of 'n'. It simply means if 'n' number of photons are detected at time 't', what is the probability of detecting same number of photons at time 't+τ'. One can see that it is an useful quantity for studying single photons. It is related to photon statistics explained before as $g^{(2)}(0) = 1 + \frac{V(n)-\langle n\rangle}{\langle n\rangle^2}$. Also by experimentally measuring $g^{(2)}(0)$ one can study the photon statistics; for bunched light $g^{(2)}(t) > 1$, for coherent light $g^{(2)}(t) = 1$ and for anti bunched light $g^{(2)}(t) < 1$ [3].

4.2 Hong Ou Mandel experiment

Hong Ou Mandel (HOM) effect is a result of interference of two single photons. Hence it can be explained only by considering the quantum nature of light and there is no classical analogue for this.

Consider a single photon is incident on a 50/50 beam splitter with output arms 'A'

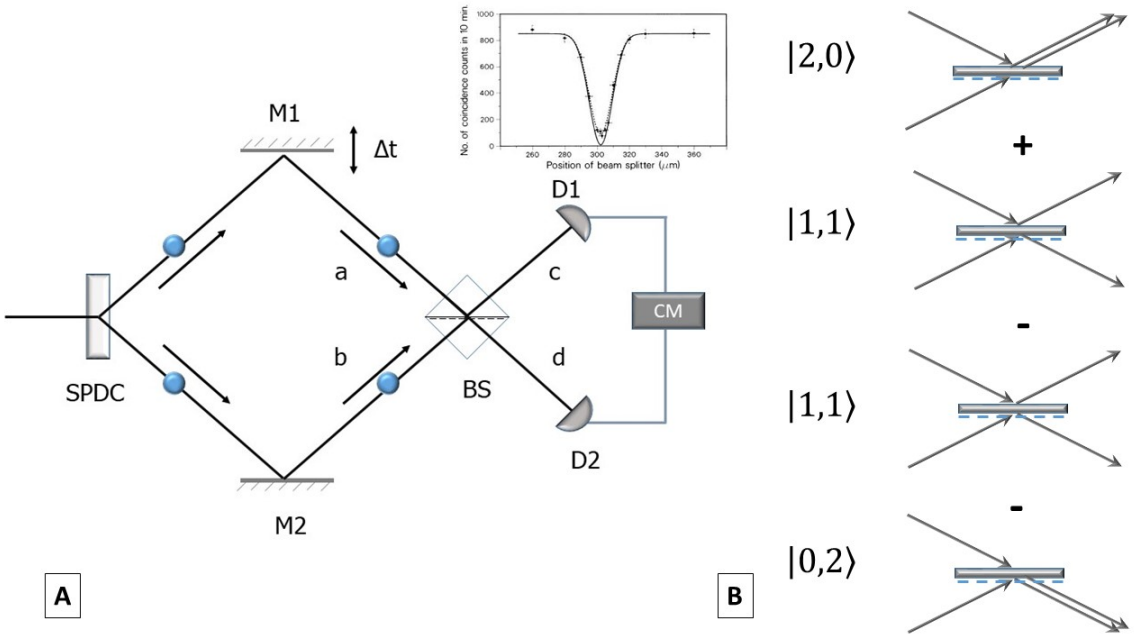

Figure 4.2: A) Hong Ou Mandel experiment setup [5], SPDC - Spontaneous Parametric Down Conversion, M1,M2 - Mirrors, BS-Beam splitter, D1, D2- Detectors, CM- Coincidence Measurement.Δt corresponds to shifting of M1 position. Inset: Coincidence counts as a function of Δt showing HOM dip.[6] B) All 4 possible output states are shown. Side with the blue dashed line imparts π phase shift on reflection.

and 'B'. In the case of classical light, it is known that 50% of light travels in either of the output arms. But in the case of single photon it can be said that it has the probability of transmitting in output A or B. This can represented in photon number states $\mid 0\rangle$ and $\mid 1\rangle$. The two cases of one photon in output A or output B can be written as states $\mid 1\rangle_A \mid 0\rangle_B$ and $\mid 0\rangle_A \mid 1\rangle_B$ respectively. Therefore, the output state is the quantum superposition of these 2 states which is written as

$$\psi_{out} = \frac{\mid 1\rangle_A \mid 0\rangle_B + \mid 0\rangle_A \mid 1\rangle_B}{\sqrt{2}} \tag{4.7}$$

It is hard to imagine in the classical sense how a single photon can exist in a linear superposition in probability. But when detectors are placed at each output, the probabity wave function collapses to either one of the states, transmission or reflection from the beam splitter. When the photon counting is performed for a sufficiently long period one should obtain 50% of the counts for output A (or B) for a perfectly 50-50 beam splitter.

Considering 2 identical single photons incident on a beam splitter as shown in figure 4.2, one can observe two-photon interference effect called Hong Ou Mandel (HOM) effect [6]. A pair of single photons are produced using Spontaneous Parametric Down Conversion (SPDC) process using a nonlinear crystal. The beam splitter is such that the reflection from one side acquires a π shift compared to that from other side. This scenario can be mathematically realized utilizing creation and annihillation operators. For example, if $\hat{a}$ is an annihillation operator and $\hat{a}^\dagger$ its corresponding creation operator then their operation on photon number states will have these properties. $\hat{a} \mid n\rangle = \sqrt{n} \mid n-1\rangle$; $\quad \hat{a}^\dagger \mid n\rangle = \sqrt{n+1} \mid n+1\rangle$. And they obey the commutation relation $[\hat{a}, \hat{a}^\dagger] = 1$ [3].

For the case of setup in figure 4.2, two creation operators $\hat{a}^\dagger$ and $\hat{b}^\dagger$ are considered for 2 input arms. The 50-50 beam splitter mixes these states into two output modes. This is described by a transformation from input to beam splitter modes as $\hat{a}^\dagger \rightarrow \frac{\hat{c}^\dagger + \hat{d}^\dagger}{2}$; $\quad \hat{b}^\dagger \rightarrow \frac{\hat{c}^\dagger - \hat{d}^\dagger}{2}$. The negative sign in $\hat{d}^\dagger$ term when transformed from $\hat{b}^\dagger$ is because of the π phase shift associated with bottom reflection as mentioned before. Therefore a unitary transformation between these modes can be written as follows.

$$\begin{pmatrix} \hat{a} \\ \hat{b} \end{pmatrix} \rightarrow \frac{1}{\sqrt{2}} \begin{pmatrix} 1 & 1 \\ 1 & -1 \end{pmatrix} \begin{pmatrix} \hat{c} \\ \hat{d} \end{pmatrix} \tag{4.8}$$

The beam splitter employed here with π phase shift reflection is not unique. Other beam splitter transformations are possible as long it is unitary. An operator 'U' is said to be unitary if $UU^\dagger = I$. This condition is necessary as it preserves the probability amplitude between the original and transformed states. Starting from the vacuum state, the the two identical single photons mixing in the beam splitter can be expressed as follows

$$\begin{gathered} \text{Incident modes} : \mid 1,1\rangle_{ab} = \hat{a}^\dagger \hat{b}^\dagger \mid 0,0\rangle_{ab} \rightarrow \\ \text{Beam splitter modes} : \frac{1}{2}(\hat{c}^\dagger + \hat{d}^\dagger)(\hat{c}^\dagger - \hat{d}^\dagger) \mid 0,0\rangle_{cd} = (\hat{c}^{\dagger 2} - \hat{d}^{\dagger 2}) \mid 0,0\rangle_{cd} = \frac{\mid 2,0\rangle_{cd} - \mid 0,2\rangle_{cd}}{\sqrt{2}} \end{gathered} \tag{4.9}$$

This shows that the cross terms cancel which can be thought of as destructive interference of two indistinguishable states. As shown in figure 4.2 b), the Feynman rules dictate that the probability amplitudes of all the possible states are to be added to obtain the final state. The

cancellation of states 2 and 3 demands that the two incident photons be perfectly identical in polarization, spatiotemporal modes etc. Only under these conditions, 2 photons exit in pairs in either of the output as seen from above calculations. If a slight change in the pathlength as shown in figure 4.2 a) as Δt is imparted, the photons become distinguishable. This can be detected in co-incidence measurements as HOM dip shown in the inset of figure 4.2 [6]

4.2.1 Metasurface in quantum optics

Metasurfaces for quantum optics applications is not much explored compared to that in classical optics. The robust control that the metasurface has over the polarization and phase of outgoing light can be tremendously useful in quantum photonics. The terminology "quantum metaphotonics", concerned with the utilization of artificial photonic devices for quantum state manipulation, has recently been proposed to describe light-matter interaction in unconventional material parameters and extreme coupling conditions [7][8].

As an example of the important implication of quantum effects in nanophotonics, it has been shown for example that quantum coherence could significantly enhance the generation of surface plasmons by stimulated emission of radiation holding promise for new quantum control of nanoplasmonic devices [9]. Metasurfaces are also demonstrated to create Anisotropic Quantum Vacuum in the vicinity of a quantum emitter to induce interference among radiative decay channels hence engineering the light-matter interactions [10]. Photons are one of the efficient systems for quantum experiments, because of the ease of preparation of quantum states and their manipulation. It has been recently shown that metasurfaces being classical devices doesn't destroy the coherence of quantum light [11] . Also in the same work an interesting phenomenon of entanglement between spin and angular momentum states using metasurfaces have been shown reiterating that metasurfaces are an effective platform for quantum information studies. Metasurfaces have been used as a mediator for quantum entanglement[12]. They have been employed for multi-photon quantum state measurement and their polarization state reconstruction[13].

Inspired by these works, in this thesis we have made an attempt to systematically explore the potential of metasurfaces by introducing them in HOM interference experiment which is one of the fundamental experiments in quantum optics. The idea is to replace the 50-50 beam splitter in HOM setup with a dual phase gradient metasurface for photon state mixing. This

is demonstrated in subsequent sections and shown that metasurfaces offer greater flexibility over conventional optical components. We also note the similarity between our work with a recent work on quantum interferometry with metasurface [14]. But we propose here a novel metasurface with additional functionality which might be useful for other quantum optics experiments.

4.3 Pancharatnam Berry phase measurement

The final objective is to design a phase gradient metasurface based on PB phase to measure second order correlation ($g^{(2)}$) function in two-photon interference experiment. But prior to that, to study the behaviour of PB phase gradient metasurface and for the completeness of the discussion, conventional interference measurement ($g^{(1)}$) is performed with metasurfaces.

The idea is to replace the beam splitter with a Pancharatnam Berry (PB) phase gradient metasurface in a standard Mach-Zehnder interferometer (MZI) setup. The metasurface is designed such that the transmitted power in 0th and 1st order of diffraction are equal (1:1) to mimic the 50:50 beam splitter in the original experiment. As discussed in the Introduction chapter, the PB phase is associated with the first order of diffraction. Owing to PB phase and different pathlength, the deflected beam (1st order) and undeflected beam (0 order) have a phase difference of ϕ. From standard MZI equations we know that the intensity of 2 interfered beams is given by $I_1 + I_2 + 2\sqrt{I_1 I_2}\cos(\phi)$. For an ideal 50-50 beam splitter, $I_1 = I_2 = I_0$. Therefore, the intensity of interfered beam is given by

$$I = 2I_0(1 + \cos(\phi)) = 4I_0(\cos\left(\frac{\phi}{2}\right))^2 \tag{4.10}$$

Now, to design a metasurface functioning as a 50-50 beam splitter, the following strategy is applied. Recalling equation 1.10 for transmitted field from a PB phase nanopillar from the Introduction chapter,

$$E_T = \frac{(e^{i\phi_x} + e^{i\phi_y})}{2}.E_{LCP} + \frac{(e^{i\phi_x} - e^{i\phi_y})}{2}.e^{im2\alpha}.E_{RCP} \tag{4.11}$$

Here LCP is the incident polarization and the opposite circular polarization RCP has

PB phase. From this equation, it can be seen that by substituting $\phi_x - \phi_y = \pi$ the LCP component (0th order) becomes zero and 100% deflection from RCP component (1st order) can be obtained in the output. To design a 50-50 beam splitter, intensity of the transmitted field can be calculated by taking the complex conjugate of the field. By equating the transmission intensity of LCP and RCP component the following condition is obtained.

$$(e^{i\phi_x} + e^{i\phi_y}).(e^{-i\phi_x} + e^{-i\phi_y}) = (e^{i\phi_x} - e^{i\phi_y}).(e^{-i\phi_x} - e^{-i\phi_y}) \tag{4.12}$$

Solving this, one arrives at the condition $\phi_x - \phi_y = \frac{\pi}{2}$. It implies that by designing nanopillars to impart phase shift of $\frac{\pi}{2}$ between and x and y axis one can achieve 50-50 beam deflection. Therefore, it can be said that by tuning the birefringence of PB phase metasurfaces, the transmission ratio along 0th and 1st order of diffraction can be controlled.

4.3.1 Metasurface Simulation

The simulation, fabrication and experimental results of this metasurface are discussed in our recent work [15]. To design the metasurface, electromagnetic simulation in Lumerical is performed. PB phase metasurfaces can be realized by disposing Gallium Nitride (GaN) nanopillars on Sapphire substrate with designed structural parameters to introduce proper forward scattering phase and amplitude. The amplitude and phase responses are related to the length and width of nanopillar and for this case meta-atoms with a constant height of 800 nm are considered. To build this PB phase metasurface, the phase retardation difference between ordinary and extraordinary axis of a nanopillar should be $\frac{\pi}{2}$ as explained. To quantify the phase retardation difference of light transmitted through GaN nanopillars, electromagnetic simulations of subwavelength nanopillars arranged in a square lattice were performed using the FDTD using two sources of 632.8 nm wavelength with polarization Ex and Ey. In the FDTD simulation, perfectly matched layer (PML) conditions in the direction of light propagation and periodic boundary conditions along all the in-plane directions were used, respectively as shown in figure 4.3 A). The use of PML boundary conditions in the propagation direction results in an open space simulation while in-plane periodic boundary conditions mimic a subwavelength array of identical nanostructures. After identifying the elements with $\frac{\pi}{2}$ phase difference from the phase map (figure 4.4 A), they were arranged in an array by successively rotating by angle as shown in figure 4.3 B). Again by rotating

pillars in the range of 0 to 180 degrees, a full phase coverage of 0 to 2π can be achieved in a period. For example, in figure 4.3 B), one period of 3 µm is discretized into 5 equally spaced points represented by 5 nanopillars with successive rotation of $\theta = 36°$ compared to the adjacent pillar. Usually, discretization in a period is chosen such that the adjacent pillars have sufficient gap in between them to avoid near field coupling effects. Employing the same method, three different metasurfaces were designed with periods of array 2µm, 2.9µm, 4µm with $\theta = 45°, 36°, 30°$ respectively. Also subwavelength period of 320 nm along y-axis was used to suppress diffraction orders along this axis. The deflection angle of the array can be calculated using generalized law of refraction ($n_t \sin(\theta_t) = n_i \sin(\theta_i) + \frac{\lambda}{2\pi}\frac{d\phi}{dx}$). Here $\sin(\theta_i) = 0$ as it is the normal incidence case.

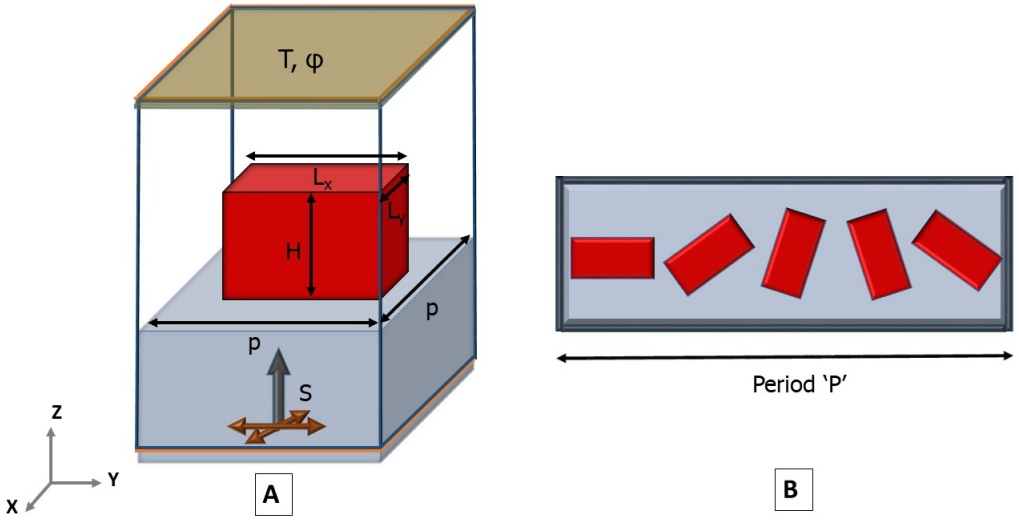

Figure 4.3: A) FDTD simulation setup for a single Gallium Nitride nanopillar of height H=800nm on Sapphire substrate with p=320 nm. The 4 faces bound by blue lines correspond to periodic boundary condition and the top and the bottom face bound by orange lines represent Perfectly Matched Layer (PML). 'S' stands for source with polarization components along both X and Y axis. The farfield monitor on the top face records Transmission(T) and phase (ϕ). B) Arrangement of PB phase nanopillars in array period P=2.9µm of a phase gradient is shown. Here successive rotation of $\theta = 36°$ is used and the nanopillars are equally spaced.

Figure 4.4 A) and B) are the resulting phase and transmission maps from the simulation. The white points and lines correspond to dimensions of nanopillars introducing relative phase shift of $\frac{\pi}{2}$ or $\frac{3\pi}{2}$ between x and y axis. But from our previous experience, dimensions slightly

different from these points of $L_x = 260nm$ and $L_y = 85nm$ which corresponds to phase shift of $\frac{\pi}{4}$ was chosen to account for phase variation due to tapering of tall nanapillars [16] [15] . The transmission map guides us to choose the dimensions of nanopillars with high transmission values. Also it has to be made sure that the chosen dimension of L_x, L_y have equal transmission along x and y axis. This is because to obtain circular polarization in the output, it is required to have equal amplitudes for E_x and E_y components. Figure 4.5 C) is the scanning electron microscopy image of one of the fabricated metasurfaces with the period of 3µm. Here tapering of the pillars can be noticed. The nanofabrication of the metasurface is discussed in the next section.

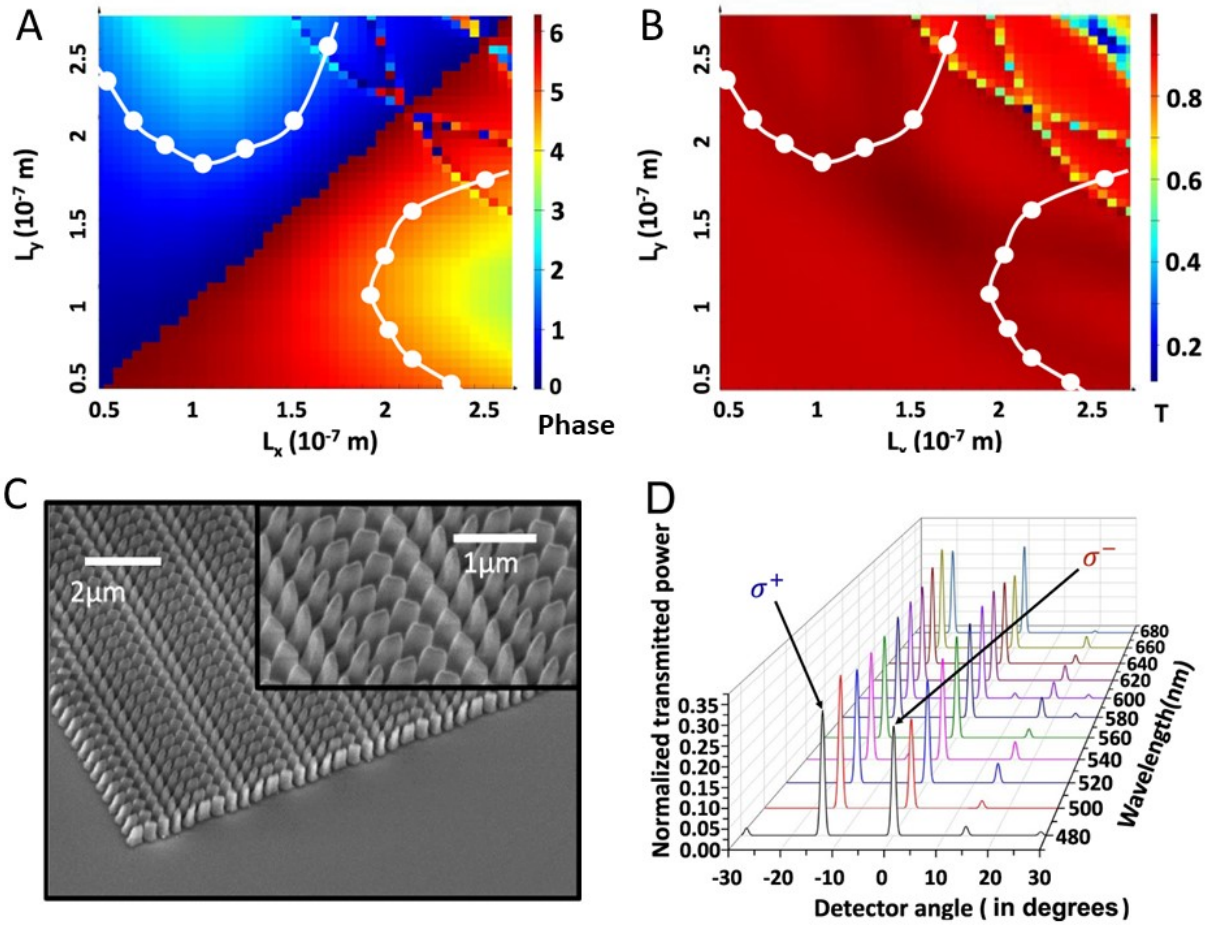

Figure 4.4: Results of FDTD simulation A) Phase difference($\phi_x - \phi_y$) map B) Transmission map. Here the white dots and lines correspond to (L_x, L_y) with phase shift of $\frac{\pi}{2}$ or $\frac{3\pi}{2}$ C) Scanning Electron Microscopy (SEM) image for metasurface with array period P=2.9 µm D) Transmission power measurement as a function of detection angle of a circularly scanning detector for metasurface with array period P=2 µm with incident LCP polarization. [15]

4.3.2 Experimental results

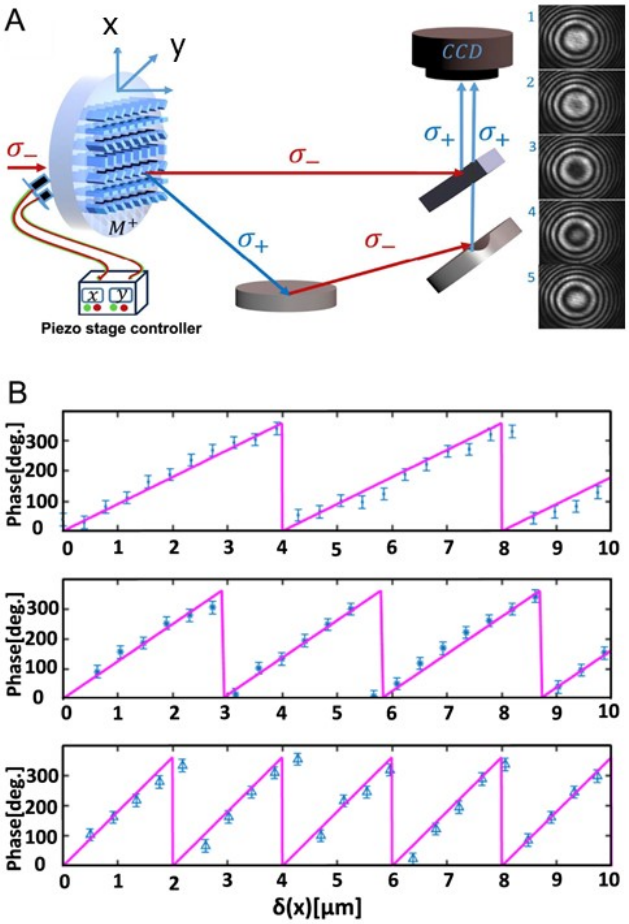

Figure 4.5: (A) (Left) Schematic of the interferometric measurement for the characterization of the topological phase shift introduced by Pancharatnam–Berry (PB) metasurface as a 50/50 Circular polarization beam splitter. (Right) The interference fringes displacement according to the phase gradient direction δx, resulting from the topological phase delay shift introduced on the deflected beam. (B) The measured phase delays as a function of the displacements are reported for three different metasurfaces, with array periods P = 4, 2.9 and 2 µm from top to bottom, respectively.[15]

To measure the angles of deflection from the metasurface, a detector scanning in a circular fashion was employed to span all angles which is shown in figure 4.11 A). The PB metasurface was placed exactly at the center of the scanning circle. A supercontinuum source was used to span wavelengths of light from 480-680 nm with the intervals of 20 nm. With the polarization LCP incident on the metasurface, angles from -30 to 30 degrees was scanned to obtain the

data in figure 4.4 D). The results shown are for metasurface with array period of 2µm which has deflection angle of 18.44° at its design wavelength of 632.8nm. It can be noticed that zero order and first order indicated as σ^- and σ^+ respectively have approximately equal transmitted power around the design wavelength. Zero order being at 0 degrees, one can observe that the dominant 1st order and weaker -1st order show angular variation as a function of wavelength depicting dispersion owing to diffraction from metasurface.

In a standard MZI setup, the first beam splitter is replaced by the fabricated metasurface as shown in figure 4.5. Helium-Neon laser of wavelength 632.8 nm and Left circular polarization is incident on the metasurface. Along one arm of the MZI, the first order deflection from the metasurface imparts a phase ϕ_{PB}. The total phase difference between the two arms (zero order and first order) is due to the PB phase and difference in propagation distance of the two arms. Interference pattern is obtained on the detector by mixing both the arms in a beam splitter. A Piezo stage capable of translation of tens of nanometer is employed to translate the metasurface along the direction of phase gradient (x axis). This results in variation of interference pattern as shown in 4.5 A) insets. Reference point of center of the rings is chosen where intensity is measured with respect to the peak intensity. From this, phase is retrieved according to the equation 4.10. This is plotted as a function of translation distance in figure 4.5 B) (blue points) for metasurfaces with array periods 2µm, 3µm, 4µm. One can be sure that the phase variation plotted is PB phase as it is resulting from translation of the metasurface in the plane normal to the incident beam and the propagation distance of both arms are remaining constant throughout.

Here the key take-away point is that the overall PB phase is dependent on the position where the beam is incident in the period of metasurface. Hence it is said to be topological phase which is suitably utilized in HOM setup in the next section. It should not be misunderstood that the beam is interacting with a single nanopillar as suggested by figure 4.5 A) but it illuminates the whole period. Even so, the phase of the transmitted beam varies with translation along the period owing to topological phase.

4.4 HOM effect with metasurface

Extending the idea of designing metasurface for MZI, in this section a metasurface is designed for measuring second order correlation function of single photons. A novel flat optical element

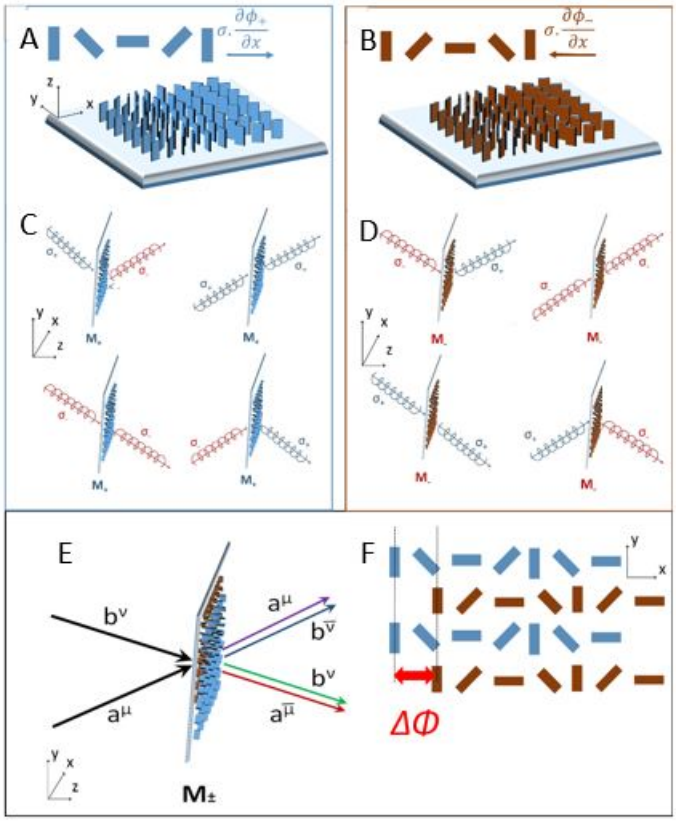

Figure 4.6: Design of Dual Gradient Metasurface (DGM) A) and B) show the phase gradient along positive and negative x-axis respectively. C) and D) describe the functionality of each metasurface with blue and red rays corresponding to RCP and LCP respectively. E) Mixing of different spatial and polarization modes of incident photons in DGM is shown. F) $\Delta\Phi$ shift of a grating with respect to the other for HOM experiment.

called Dual-Gradient Metasurface (DGM) is proposed which is constructed by superimposing two lattices with opposite sense of phase gradients. The functionality of the metasurface with incident light of polarizations are shown in the Figure 4.6. The incident polarization splits into two beams with orthogonal polarization in the same basis depending on the incident angle. For instance, an incident beam with right circular polarization creates one beam with right circular and one with left circular polarization which is originated from the topological Pancharatnam-Berry (PB) phase of the metasurface.

4.4.1 Theory for Dual Gradient Metasurface

As mentioned before, from an intial photon of frequency ω_0, two down converted single photons can be produced using a nonlinear crystal through SPDC process. However, the two single photons may not have exactly the same frequency but the sum of them is always equal to ω_0 which ensures energy conservation. Assuming the two photons to be of frequencies $\omega_1 = \frac{\omega_0}{2} + \omega$ and $\omega_2 = \frac{\omega_0}{2} - \omega$, the resulting two photon state can be written as

$$|\psi_0\rangle = \int d\omega . S(\frac{\omega_0}{2} + \omega, \frac{\omega_0}{2} - \omega) a^\dagger_{\frac{\omega_0}{2}+\omega} a^\dagger_{\frac{\omega_0}{2}-\omega} |0\rangle \tag{4.13}$$

where $S(\omega_1, \omega_2)$ is a spectral weight function. Here $|0\rangle$ represents vacuum state and dagger on each mode stands for creation operator. The discussion below is borrowed from the original work of Hong Ou Mandel [6] which is later modified for the case of metasurface. Instead of measuring the field intensities, the HOM interferometer measures the coincidence counting signal as,

$$G^{(2)} = \int d\tau \langle E_1^\dagger(t) E_1^\dagger(t+\tau) E_2(t+\tau) E_1(t) \rangle \tag{4.14}$$

where the expectation value is calculated with respect to the initial state ϕ_0. Here $G^{(2)}$ is same as $g^{(2)}$ from equation 4.6 except that the latter is the normalized coincidence counting. The fields $E_{1,2}$ after the beam splitter relate to input fields $E_{01,02}$ as

$$\begin{aligned} E_1(t) &= \sqrt{T} E_{01}(t - \tau_1) + i\sqrt{R} E_{02}(t - \tau_1 + \delta t) \\ E_2(t) &= \sqrt{T} E_{02}(t - \tau_1) + i\sqrt{R} E_{01}(t - \tau_1 - \delta t) \end{aligned} \tag{4.15}$$

where 'T' and 'R' are transmission and reflection coefficients of the beam splitter, τ_1 accounts for the propagation in the interferometer arms. Here δt represents the shifting of the beam splitter towards one or another source creating the asymmetry in the overall propagation lengths in two arms (enters with different sign into expressions). This is equivalent to Δt in HOM setup in figure 4.2 A). Note, that the factor 'i' is added in front of reflection coefficient R to mimic the notation used in the literature related to HOM interferometer. Also

this ensures that the beamsplitter operator $\frac{1}{\sqrt{2}}\begin{pmatrix}1 & i\\ i & 1\end{pmatrix}$ is an unitary matrix when $T = R = \frac{1}{2}$ which is a necessary condition as discussed before. By substituting equation 4.15 in 4.14 we get,

$$G^{(2)} = \int d\tau \mid G(0) \mid^2 [T^2 \mid g(\tau) \mid^2 + R^2 \mid g(2\delta\tau - \tau) \mid^2 - TRg(\tau)^* g(2\delta\tau - \tau) + g(\tau)g(2\delta\tau - \tau)^*] \tag{4.16}$$

Here $G(\tau)$ is the first order correlation function which is related to the spectral weight function by a fourier transform as,

$$G(\tau) = \int d\omega \Phi(\omega_0/2 + \omega, \omega_0/2 - \omega) e^{-i\omega\tau} \tag{4.17}$$

Also $g(t) = \frac{G(t)}{G(0)}$. For the special case when $g(\frac{\omega_0}{2} + \omega, \frac{\omega_0}{2} - \omega)$ is gaussian in ω with bandwidth $\Delta\omega$ results in $g(\tau) = e^{-(\Delta\omega\tau)^2/2}$. Substituting this in equation 4.16 with $T = R = \frac{1}{2}$ we obtain,

$$G^2(\delta\tau) \sim 1 - e^{-(\Delta\omega\delta\tau)^2} \tag{4.18}$$

We now modify the setup and add a Dual-Gradient metasurface shown in figure 4.6 instead of the 50-50 beam splitter. Here each gradient in the DGM yields a phase to the orthogonal polarization component. To make it similar to the beam splitter in the HOM interferometer case, the possibility to adjust the arm length to create asymmetry between them is considered. The polarization can either be RCP or LCP, it is not fixed for the incoming two photons. The metasurface output will be governed by a modified relation that depends on the polarization state μ, ν of the two input fields. The following calculations are borrowed from [17]

$$\begin{aligned} E_1^{\mu}(t) &= \sqrt{T_0} E_{01}^{\mu}(t - \tau_1) + ie^{-i\phi_2^{\mu}} \sqrt{T_1} E_{02}^{\bar{\mu}}(t - \tau_1 + \delta t) \\ E_2^{\nu}(t) &= \sqrt{T_0} E_{02}^{\nu}(t - \tau_1) + ie^{-i\phi_2^{\nu}} \sqrt{T_1} E_{01}^{\bar{\nu}}(t - \tau_1 + \delta t) \end{aligned} \tag{4.19}$$

where T_0 and T_1 are the transmission coefficients for zero and first order components respectively. We also assumed that the transmission amplitudes do not depend on the polarization. The coincidence counting for a pair of arbitrary polarization is given by $G^{(2)}$

$$G^{(2)}_{\mu\nu} = \int d\tau \langle E_1^{\mu\dagger}(t) E_2^{\nu\dagger}(t+\tau) E_2^{\nu}(t+\tau) E_1^{\mu}(t) \rangle \tag{4.20}$$

Substituting equation 4.19 in 4.20 and carrying out similar treatment as for the 50-50 beam splitter case,

$$G^{(2)}_{\mu\nu}(\delta\tau) \sim 1 - \cos(\phi_1^{\mu} - \phi_2^{\nu}) e^{-(\Delta\omega\delta\tau)^2} \tag{4.21}$$

Here, when both incident photons have same polarization, due to nonlinear topologically induced splitting, the photons are scattered from different phase gradients. This leads to $\phi_1^{\mu} - \phi_2^{\nu} = \Delta\Phi$, where $\Delta\Phi$ is the topological phase shift between two phase gradients. We thus get an oscillating pre-factor $\cos(\Delta\Phi)$. One can thus make the two grating to be shifted relative to each other by any amount. Making several measurements with different phase delay $\Delta\Phi$ allows us to change the degree of distinguishability between photon and thus controlling the photon statistics. It is to be noted that the right hand side of equation 4.21 ranges from 0 to 2 as compared 0 to 1 in equation 4.18 which implies that the DGM offers more control over the experiment.

4.4.2 Dual Gradient Metasurface design

Recalling the generalized law of refraction taking into account the incident polarization of PB metasurface,

$$n_t \sin(\theta_t) - n_i \sin(\theta_i) = \sigma_{\pm} m \frac{\lambda}{2\pi} \frac{d\phi}{dx} \tag{4.22}$$

Here for Right Circularly Polarized (RCP) incidence $\sigma_+ = 1$ and for Left Circularly Polarized (LCP) incidence $\sigma_- = -1$. Also 'm' is the diffraction order in transmission. In a DGM, the incident angles for two spatial modes are θ and $-\theta$. For only one phase gradient in the dual gradient (figure 4.6), one needs to consider the condition that if $\theta_i = \theta$ then $\theta_t = -\theta$ for m=1 order. As it is based on PB phase, the first order is essentially in the

opposite circular polarization. Considering the case of RCP incidence ($\sigma_+ = 1$) and air as the surrounding medium of metasurface ($n_t = n_i = 1$) and substituting the above conditions in equation 4.22, we get

$$\frac{d\phi}{dx} = -2\sin(\theta).\frac{2\pi}{\lambda} \tag{4.23}$$

This is the phase gradient of metasurface required for the above functionality. In principle, metasurface for any θ can be designed but practically there are constraints which have to be taken into account. First, metasurface deflection efficiency tends to decrease as incidence angle increases. This is because metasurface has to impart higher magnitude of momentum or phase gradient for higher θs to drive the beam from θ to $-\theta$ as shown in equation 4.23. Therefore, higher values of θ are not favourable for metasurface performance. On the other hand, metasurface opens many diffraction orders in transmission for lower angles of incidence. But it is ideal to have only zero and first diffraction orders as undesirable diffraction orders result in decreased efficiency in the first order. This is an obstacle for achieving 50:50 beam splitter DGM. Therefore this factor determines the lower limit of θ. Taking into account the above conditions, we impose a constraint on equation 4.22 that the orders m=-1 and 2 which are immediately next orders of 0 and 1 should cease to exist in transmission. Assuming the same conditions for metasurface as before ($\theta_i = \theta$, $n_t = n_i = 1$, $\sigma_+ = 1$) and calculating refraction angle for m=-1 order in equation 4.22 we get,

$$\sin(\theta_t) - \sin(\theta) = -\frac{\lambda}{2\pi}\frac{d\phi}{dx} \tag{4.24}$$

It has to be noted that the phase gradient of the metasurface is already calculated in equation 4.23 by imposing the condition $\theta_t = -\theta$ when $\theta_i = \theta$ for m=1 order. The response of the same metasurface for m=-1 order is being calculated here. Therefore substituting equation 4.23 in 4.22 we get,

$$\sin(\theta_t) = -3\sin(\theta) \tag{4.25}$$

Now for the condition $\sin(\theta_t) > 1$ or $\sin(\theta_t) < -1$ the m=-1 order ceases to exist. Applying this inequality in equation 4.25, we get $\sin(\theta) > \frac{1}{3}$ or $\sin(\theta) < -\frac{1}{3}$. The range of angles satisfying these inequalities are $\theta < -19.47°$ and $\theta > 19.47°$. Performing the same calculations for m=2 order also leads to the same permissible range of θ. Therefore, we

choose $\theta = 20°$ and$-20°$ as the incidence angles on the metasurface. The equal and opposite angles are necessary for obatining symmetric spatial modes in HOM setup as shown in figure 4.7.

The primary source of photons is a 400 nm laser which is fed to a nonlinear Barium Borate(BBO) crystals. This results in down converted single photons of approximately 800 nm wavelength. Therefore, here a PB phase gradient metasurface is designed to function at the wavelength of 800 nm. Again from equation 4.22, the array period to design the metasurface can be calculated. For a constant phase gradient, $\frac{d\phi}{dx} = \frac{\Delta\phi}{\Delta x}$. By substituting $\theta_i = 20°$, $\theta_i = -20°$, $n_t = n_i = 1$, $\sigma_+ = 1$,$m = 1$ and $\Delta\phi = 2\pi$ in equation 4.22 we get $\Delta x =$ period=1170 nm. With this array period, DGM is designed and the dimension required for each nanopillar is obtained from FDTD simulation which is explained in the next subsection.

4.4.3 Metasurface simulation and fabrication

The FDTD simulation is done in Lumerical software for 1200 nm tall GaN nanopillars on Sapphire substrate. The simulation setup is exactly the same as in figure 4.3 A) except that the periodic boundary conditions are replaced by Bloch boundary conditions to account for oblique incidence in periodic structures. Also the angle of incidence is 20°. But from the figure it can be seen that the source is in Sapphire substrate. The refraction angle in Sapphire is calculated to be 11.2° for 20° incident angle in air using Snell's law. For this oblique incidence, the phase difference (between x and y axis) map and transmission map is computed for L_x and L_y spanning from 50 nm to 400 nm with an interval of 10 nm as shown in figure 4.7. The dimensions marked with red stars on the maps are chosen as they correspond to π on the phase difference map. They also satisfy the condition of high transmission(T) and $T_x = T_y$ for circular polarization output as discussed before. They correspond to $L_x = 370nm$, $L_y = 120nm$ and $L_x = 120nm$, $L_y = 370nm$ which are symmetric, hence either one of them can be chosen. It can be noticed that the transmission for this case is relatively low compared to that in figure 4.4 B). This might be due to difference in waveguiding modes at different incident angles.

The array period of 1170 nm is discretized into 3 points on which the nanopillars with above dimensions are arranged as shown in figure 4.7 C). Also along y axis, subwavelength array period of 430 nm is used to avoid diffraction along this axis. To span phase from 0 to 2π,

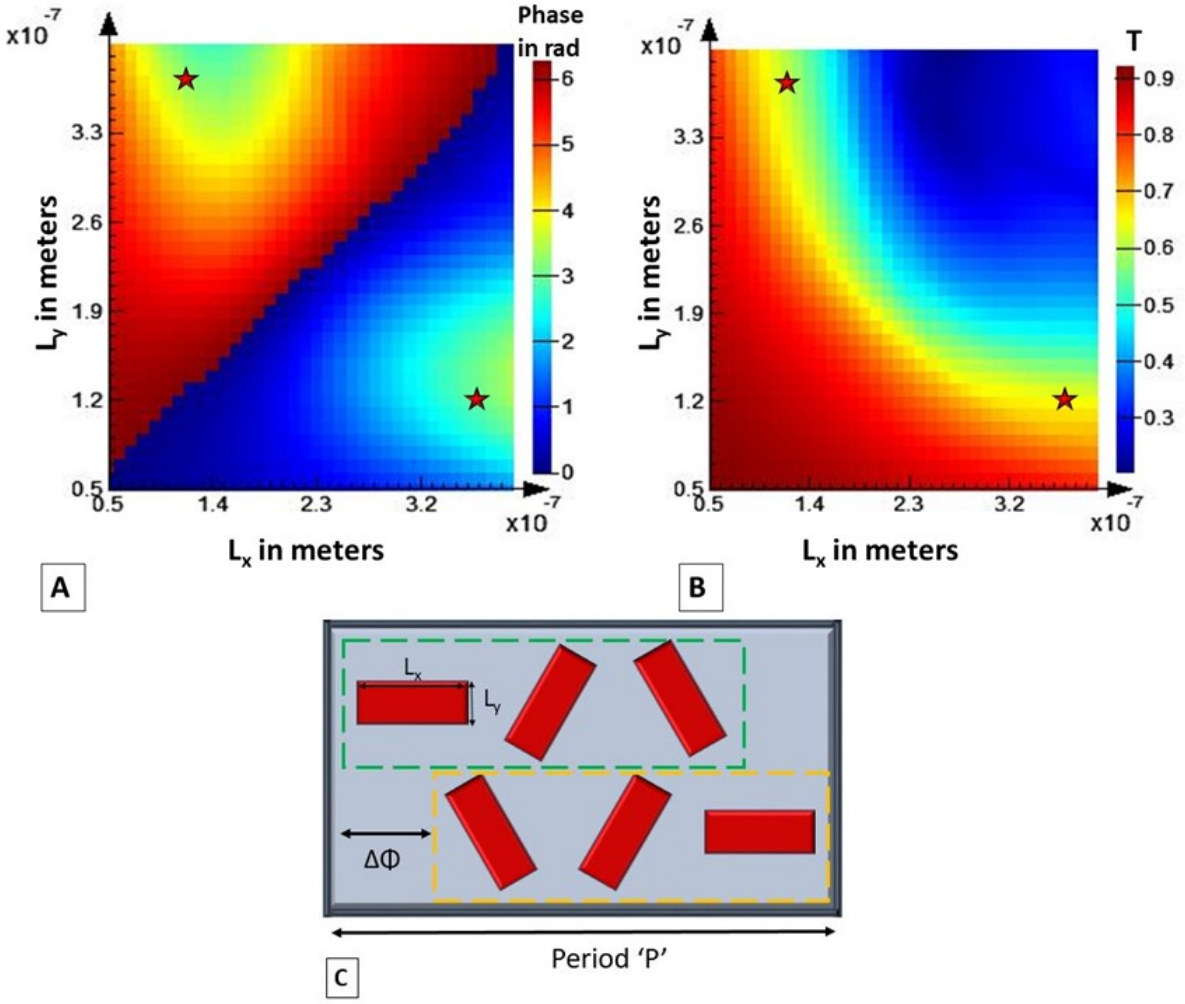

Figure 4.7: FDTD simulation results for single GaN nanopillars on Sapphire substrate A) Phase difference ($\phi_x - \phi_y$) map B) Transmission (T) map. Points with red stars correspond to dimensions (L_x, L_y) with π phase shift. C) A unit cell of DGM is shown with opposite phase gradients (with green and yellow dotted boxes) having phase shift of $\Delta\Phi$.

one period includes nanopillars of rotation 0°, 60° and 120°. For realizing DGM, the phase gradient is set along positive (green dotted box) and negative x-axis (yellow dotted box) with a phase shift between them $\Delta\Phi$ as shown in the figure. This shift can be expressed in terms of distance $\Delta X = \frac{\Delta\Phi}{2\pi}.P$ where 'P' is the array period. This is not to be mistaken with ϕ which is the PB phase from each nanopillar. Six different metasurfaces with $\Delta\Phi = 0, \frac{\pi}{3}, \frac{2\pi}{3}, \pi, \frac{4\pi}{3}, \frac{5\pi}{3}$ are fabricated.

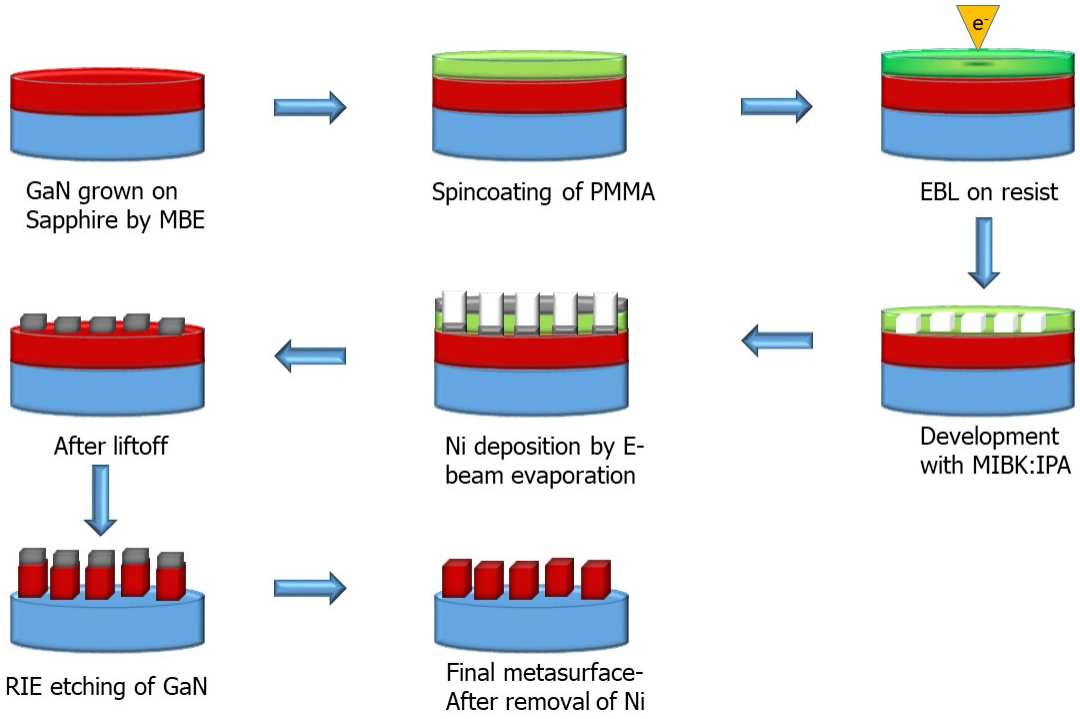

Figure 4.8: Nanofabrication steps of metasurface is shown. Here blue cylinder stands for Sapphire substrate, red for Gallium Nitride, green for Poly(methyl methacrylate)(PMMA), an electron beam resist, silver for Nickel. And MBE stands for Molecular Beam Epitaxy, EBL-Electron Beam Lithography, MIBK:IPA - Methyl Isobutyl Ketone: Isopropyl Alcohol, RIE - Reactive Ion Etching

The nanofabrication process followed is depicted in figure 4.8 [15]. It was realized by patterning a 1200 nm thick GaN thin film grown on a double side polished c-plan sapphire substrate via a Molecular Beam Epitaxy (MBE) RIBER system. The GaN nanopillars were fabricated using a conventional electron beam lithography system (Raith ElphyPlus, Zeiss Supra 40) process with metallic Nickel (Ni) hard masks through a lift-off process. To this purpose, a double layer of around 200 nm Poly(methyl methacrylate) (PMMA) resists (495A4 then 950A2) was spin-coated on the GaN thin film, prior to baking the resist at a temperature

of 125 °C. E-beam resist exposition was performed at 20 keV. Resist development was realized with 3:1 Isopropyl Alcohol:Methyl Isobutyl Ketone (IPA: MIBK) and a 50 nm thick Ni mask was deposited using E-beam evaporation. After the lift-off process in the acetone solution for 4 hours, GaN nanopillar patterns were created using reactive ion etching (RIE, Oxford system) with a plasma composed of Cl_2CH_4Ar gases. Finally, the Ni mask on the top of GaN nanopillars was removed by using chemical etching with 1:2 solution of $HCl : HNO_3$.

4.4.4 Experimental results

The Scanning Electron Microscopy(SEM) images of final metasurfaces after fabrication is shown in figure 4.9. Figure A) corresponds to the metasurface with phase shift between arrays $\Delta\Phi = \frac{2\pi}{3}$. The two opposite phase gradient periods are shown as red and yellow rectangles from which the phase shift can be noticed. The dimension of nanopillars (L_x, L_y) and array period 'P' were measured and were found to be close to the design values. Figure 4.9 B) corresponds to the metasurface with phase shift $\Delta\Phi = 0$ and is captured by tilting the microscope stage. Significant tapering of the nanopillars can be observed here. This is due to the fact that the nanopillars are relatively tall (1200 nm) which results in high aspect ratio of the pillars. It is shown in the optical characterization results (Figure 4.11 A)) that the tapering drastically affects the performance of metasurface for oblique incidence.

Therefore, the fabrication was repeated with increased power of etching in the RIE step. The Radio frequency (RF) , Microwave power during RIE was maintained at 20 W, 600 W respectively compared to 20 W, 200 W in the previous fabrication. Figure 4.10 A) shows the SEM image of the final metasurface, it corresponds to $\Delta\Phi = \frac{2\pi}{3}$. Figure B) is the SEM image of metasurface corresponding to $\Delta\Phi = \pi$ captured with the tilted stage. It can be noticed that the pillars have very low degree of tapering. This significantly enhances the optical performance of the metasurface as discussed figure 4.11.

The optical characterization of transmission at different angles are performed to assess the deflection efficiency of the DGM. The supercontinuum laser is tuned to be at 800 nm which is the design wavelength of the metasurface. A set of linear polarizer and Quarter wave plate is used to obtain circularly polarized light which is weakly focused on the metasurface with a convex lens as shown in figure 4.11. A detector scanning in circular fashion is used with metasurface at the center of the scanning circle.

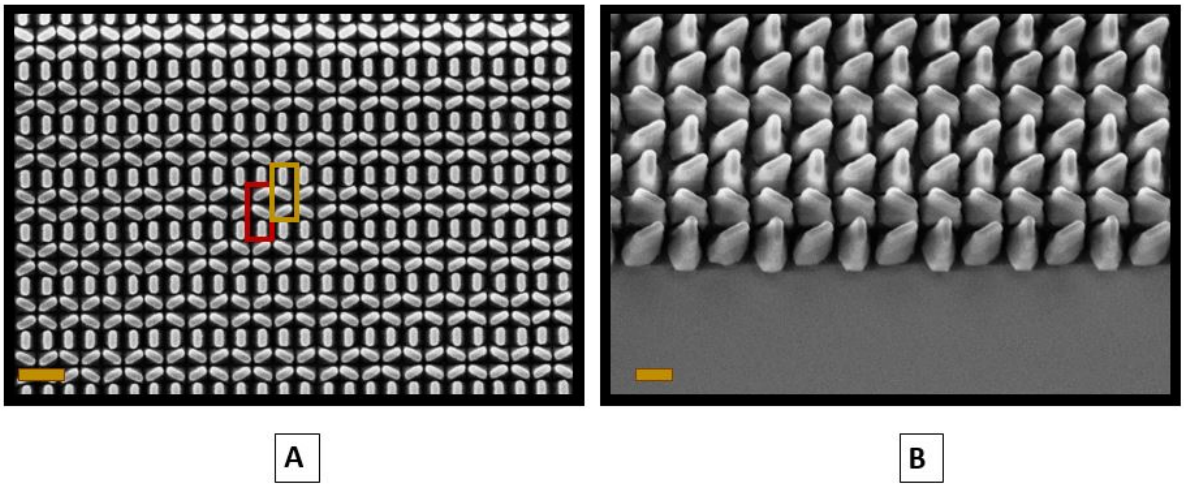

Figure 4.9: SEM images of final Dual Gradient metasurface A) For $\Delta\Phi = \frac{2\pi}{3}$. Red and yellow boxes indicate opposite phase gradients. Yellow scale bar measures 1 µm B) With tilted stage for metasurface with phase shift $\Delta\Phi = 0$. Yellow scale bar measures 0.5 µm

Figure 4.11 B) and C) compares the performance of DGM for incident angle of $-20°$ and RCP incident polarization. It can be inferred from the figures that for oblique incidence the deflection efficiency is quite sensitive to tapering of nanopillars. The optimization of fabrication method was necessary to achieve straight nanopillars and 1:1 transmission in zero and first order. Equal transmission is imperative to attain indistinguishability condition in HOM experiment. The same measurement was done for all 6 metasurfaces with varying $\Delta\Phi$ and similar results were observed. The complete characterization of the metasurface was done for incident angle of $-20°$ and $+20°$ for incident polarizations of RCP and LCP, one of the results is shown in the figure 4.6. Therefore, we claim to have fabricated a DGM which is eligible for replacing a beam splitter in HOM experiment. Single photon measurement on DGM is still underway and the progress will be discussed in the presentation.

4.5 Discussion

We have demonstrated topological metasurfaces, based on Pancharatnam-Berry phase to convert circular polarization state from left to right and reciprocally from right to left using spatially oriented birefringent nanopillars for single photon interference experiments. However, there are certain drawbacks of DGM compared to a 50-50 beam splitter. Apart from

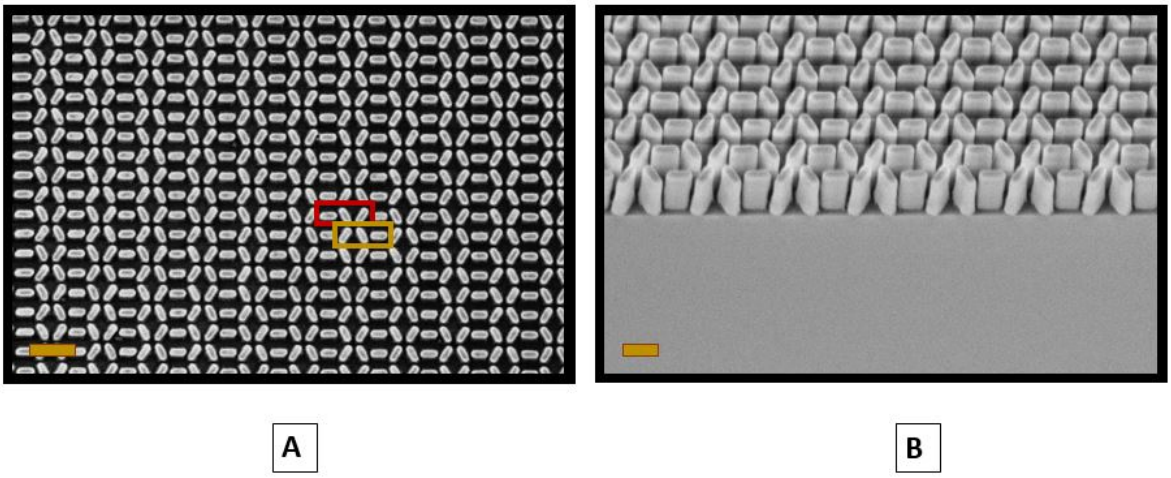

Figure 4.10: SEM images of final Dual Gradient metasurface with optimized nanofabrication A)For $\Delta\Phi = \frac{2\pi}{3}$. Red and yellow boxes indicate opposite phase gradients. Yellow scale bar measures 1 µm B) With tilted stage for metasurface with phase shift $\Delta\Phi = \pi$. Yellow scale bar measures 0.5 µm

zero and first order, other orders of diffraction were also observed in farfield measurements with the metasurface. This considerably decreases the single photon counts obtained in both detectors which can adversely affect coincidence measurements. By properly optimizing the metasurface, its efficiency can be increased so that the incident photons transmit in only either one of the channels (zero or first order) to imitate 50-50 reflection and transmission of a beam-splitter. On the other hand, the phase and polarization control offered by DGM can be utilized to achieve more functionalities than a conventional beam splitter can offer. One such possibility is obtaining Bell's states with DGM and going beyond the limits of Bell's No-Go theorem.

Bell's states pertains to entangled photon states. Two particles are said to be entangled when the quantum state of each particle cannot be described independently of the state of the other particle. Measurement of a physical property such as polarization, spin etc of the entangled particles can be found to be correlated[18][19]. The effect is also said to be non-local; measurement of the property of one particle results in wavefunction collapse of the other particle instantaneously irrespective of how far away the particles are. Consider two entangled photons with spatial modes 'a', 'b' and polarization modes '1', '2' which stand for any pair of orthogonal polarization states. Four modes can be described from them a^1, a^2, b^1, b^2. The complete Hilbert space is spanned by the orthonormal set of Bell states

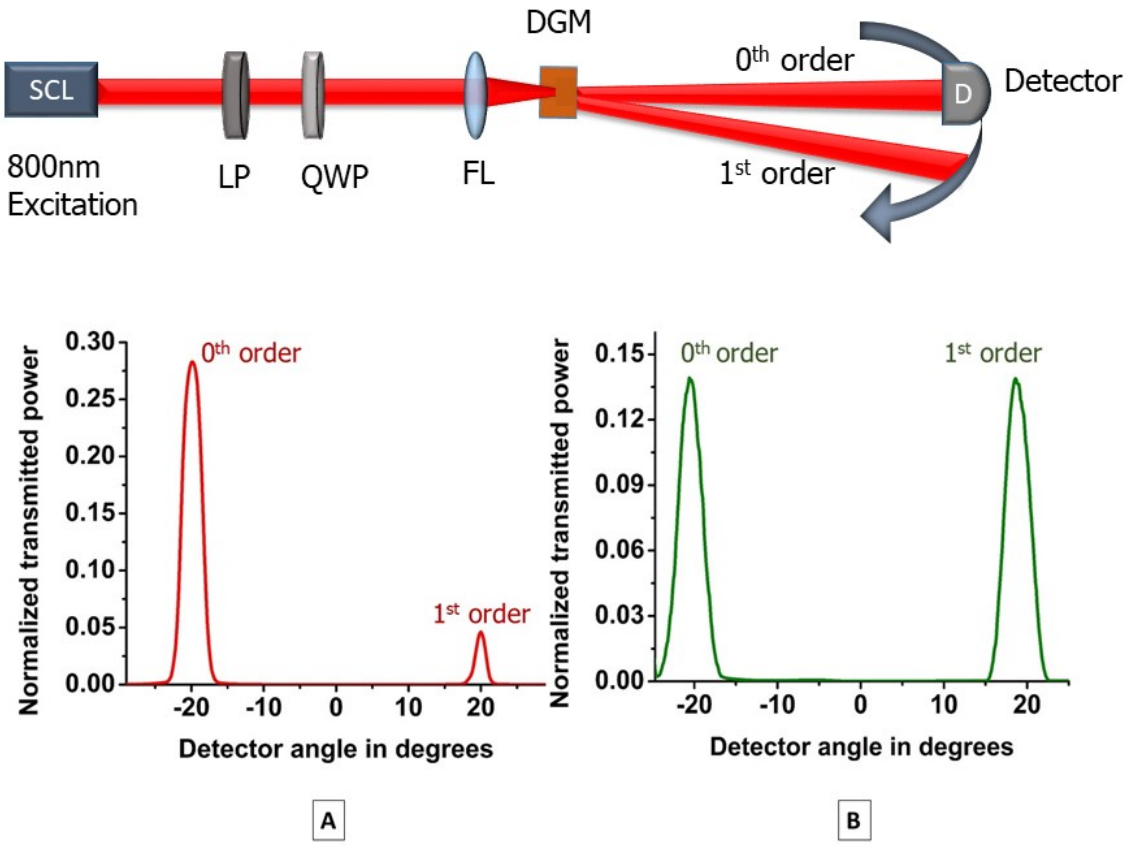

Figure 4.11: Top image: Setup to measure transmission power as a function of refracted angle of DGM. SCL- Supercontinuum Laser, LP-Linear Polarizer, QWP- Quarter Wave Plate, FL- Focusing Lens. Bottom images: Transmitted power as a function of detector angle for DGM A) with tapered nanopillars B) with nearly straight nanopillars with optimized nanofabrication steps.

given by

$$|\psi_{1,2}\rangle = \frac{1}{\sqrt{2}}(a^{1\dagger}b^{2\dagger} \mp a^{2\dagger}b^{1\dagger})\,|0\rangle$$
$$|\psi_{3,4}\rangle = \frac{1}{\sqrt{2}}(a^{1\dagger}b^{1\dagger} \mp a^{2\dagger}b^{2\dagger})\,|0\rangle \tag{4.26}$$

where $|0\rangle$ represents vacuum state and dagger on each mode stands for creation operator. Consider one of the 4 Bell states $\frac{1}{\sqrt{2}}(a^{1\dagger}b^{2\dagger} + a^{2\dagger}b^{1\dagger})\,|0\rangle$. It corresponds to entangled photon pairs where if a photon is in a^1/a^2 mode then the other photon is bound to be in b^2/b^1 mode. One of the versions of the Bell's no-go theorem can be stated as 'All of the Bell states cannot be distinguished using any standard linear optical measurements'[20]. It can be elaborated as performing photon coincidence measurements with any number of linear optical elements such as polarization beam splitters, mirrors, waveplates etc or with any combination of them, it is not possible to distinguish all four Bell states. One of the well known setup is Innsbruck detection scheme from which at most two out of four states can be detected[20]. This setup uses a beam splitter, two polarization beam splitters and four detectors for single photon detection. But by introducing an optical element such as a Dual Gradient metasurface it might be possible to distinguish more than two Bell states owing to the superior control over the phase of transmitted photons. The fact that in DGM the incident polarization splits into two beams with orthogonal polarization in the same basis (right circular polarization incident beam creates one beam with right circular and one - with left circular polarization) makes it an unique optical element. In contrast, the linear optical elements allow to create two beams of orthogonal polarization only in different basis, e.g. circularly polarized light may split into a beam with vertical and another with horizontal polarization. In this context, DGM can be considered as a non-linear optical element which technically, doesn't violate the Bell's No-Go theorem. Carefully designed metasurfaces which facilitate fully deterministic characterization of all four Bell states can open tremendous possibilities in the field Quantum communication and cryptography.

4.6 Conclusion

In this chapter, we have explored the potential of metasurfaces in the field of Quantum optics. Utilizing phase gradient metasurface in standard Mach-Zehnder interferometer, Pancharatnam-Berry phase is studied in detail. Extending the same idea, a novel design

of Dual Gradient metasurface is proposed to replace the beam splitter in Hong Ou Mandel experiment. Theoretical calculation is performed to describe the role of DGM in HOM experiment. A systematic approach is presented to design DGM using FDTD simulation. Nanofabrication and classical optical characterization of the metasurfaces are also dicussed in detail. By optimizing the fabrication method it is made sure that equal transmission is obtained in zero and first order of diffraction which is crucial to achieve accurate results in HOM experiment.

All in all, metasurfaces can not only replace bulky conventional optical elements in Quantum optics experiments but also offer added functionalities and flexibility. This is described in detail in the calculations of metasurface in HOM experiment. Metasurfaces hold promise to bring a new perspective to the field of Quantum optics.

Bibliography

[1] Robert H Hadfield. Single-photon detectors for optical quantum information applications. *Nature Photonics*, 3(12):696–705, 2009.

[2] Mark Fox. *Quantum optics: an introduction*. Oxford master series in atomic, optical, and laser physics. Oxford Univ. Press, Oxford, 2006.

[3] R Loudon. *The Quantum Theory of Light*. Oxford University Press, 2000.

[4] H Paul. Photon antibunching. *Reviews of Modern Physics*, 54(4):1061–1102, oct 1982.

[5] Sample experiments – 2-photon-interference by hong, ou & mandel @ www.qutools.com.

[6] C K Hong, Z Y Ou, and L Mandel. Measurement of subpicosecond time intervals between two photons by interference. *Phys. Rev. Lett.*, 59(18):2044–2046, nov 1987.

[7] Iñigo Liberal and Nader Engheta. Nonradiating and radiating modes excited by quantum emitters in open epsilon-near-zero cavities. *Science Advances*, 2(10), 2016.

[8] Ruzan Sokhoyan and Harry A Atwater. Quantum optical properties of a dipole emitter coupled to an ϵ-near-zero nanoscale waveguide. *Optics Express*, 21(26):32279–32290, 2013.

[9] Konstantin E. Dorfman, Pankaj K. Jha, Dmitri V. Voronine, Patrice Genevet, Federico Capasso, and Marlan O. Scully. Quantum-coherence-enhanced surface plasmon amplification by stimulated emission of radiation. *Physical Review Letters*, 111(4):1–5, 2013.

[10] Pankaj K. Jha, Xingjie Ni, Chihhui Wu, Yuan Wang, and Xiang Zhang. Metasurface-Enabled Remote Quantum Interference. *Physical Review Letters*, 115(2):1–5, 2015.

[11] Tomer Stav, Arkady Faerman, Elhanan Maguid, Dikla Oren, Vladimir Kleiner, Erez Hasman, and Mordechai Segev. Quantum entanglement of the spin and orbital angular momentum of photons using metamaterials. *Science*, 361(6407):1101 LP – 1104, sep 2018.

[12] Pankaj K. Jha, Nir Shitrit, Jeongmin Kim, Xuexin Ren, Yuan Wang, and Xiang Zhang. Metasurface-Mediated Quantum Entanglement. *ACS Photonics*, 5(3):971–976, 2018.

[13] Kai Wang, James G. Titchener, Sergey S. Kruk, Lei Xu, Hung Pin Chung, Matthew Parry, Ivan I. Kravchenko, Yen Hung Chen, Alexander S. Solntsev, Yuri S. Kivshar, Dragomir N. Neshev, and Andrey A. Sukhorukov. Quantum metasurface for multiphoton interference and state reconstruction. *Science*, 361(6407):1104–1108, 2018.

[14] Philip Georgi, Marcello Massaro, Kai-Hong Luo, Basudeb Sain, Nicola Montaut, Harald Herrmann, Thomas Weiss, Guixin Li, Christine Silberhorn, and Thomas Zentgraf. Metasurface interferometry toward quantum sensors. *Light: Science & Applications*, 8(1):70, 2019.

[15] Zhanjie Gao, Sandeep Golla, Rajath Sawant, Vladimir Osipov, Gauthier Briere, Stephane Vezian, Benjamin Damilano, Patrice Genevet, and Konstantin E Dorfman. Revealing topological phase in Pancharatnam–Berry metasurfaces using mesoscopic electrodynamics. *Nanophotonics*, (0):20200365.

[16] Gauthier Brière, Peinan Ni, Sébastien Héron, Sebastien Chenot, Stephane Vézian, Virginie Brändli, Benjamin Damilano, Jean-Yves Duboz, Masanobu Iwanaga, and Patrice Genevet. An etching-free approach toward large-scale light-emitting metasurfaces. *Advanced Optical Materials*, 7(14):1801271, 2019.

[17] Konstantin E Dorfman. Topological quantum optics with metasurfaces; subwavelength manipulation of light statistics. *(Unpublished work carried out at CNRS-CRHEA, France under the aegis of 'Fédération Doeblin')*, 2018.

[18] A Einstein, B Podolsky, and N Rosen. Can Quantum-Mechanical Description of Physical Reality Be Considered Complete? *Physical Review*, 47(10):777–780, may 1935.

[19] E Schrödinger. Discussion of Probability Relations between Separated Systems. *Proceedings of the Cambridge Philosophical Society*, 31(4):555, jan 1935.

[20] N. Lütkenhaus, J. Calsamiglia, and K. A. Suominen. Bell measurements for teleportation. *Physical Review A - Atomic, Molecular, and Optical Physics*, 59(5):3295–3300, 1999.

Conclusion

We have explored here various functionalities that are achievable using phase gradient metasurfaces. Dielectric materials based metasurfaces are employed as they are less lossy compared to plasmonic materials and favourable to work in transmission mode for visible-infrared region of spectrum. Primarily, the idea of controlling outgoing wavevectors by controlling the phase gradient has been used throughout this work. Various devices for classical and quantum optics applications are been proposed.

First, hybrid optical components were designed to combine the advantages of refractive and diffractive components. It was demonstrated with a simple example of prism by designing a phase gradient metasurface to mitigate the prism dispersion as a proof of concept. It was shown by fabricating metasurfaces of phase gradient as low as the order $10^{-5} rad/nm$ to compensate for prism dispersion. To experimentally measure such small magnitudes of dispersion, properly calibrated Fourier plane imaging and spectroscopy technique was employed. It was shown that the by tuning the phase gradient, material dispersion can be mitigated in the wavelength range where the material refractive index varies linearly with the wavelength. It can be approximated so for glass like materials in the visible region. But for the material dispersion which is not linear, perfectly achromatic hybrid devices cannot realized with this approach as there is some residual dispersion which is a limitation of this technique. As an application, an achromatic compressor using prism-metasurface combination was discussed in detail.

Extending the same principle to a lens, which is interesting for real applications, lens aberration correction metasurfaces were designed. Most common lens aberrations, chromatic and spherical aberrations were discussed. Instead of using constant phase gradient, radially vary phase gradient were designed as the wavevectors in rays refracted from a lens varies radially. These phase gradient values were analytically calculated based on ray optics

for chromatic and spherical aberrations separately. It was shown that this design is suitable for large area metasurfaces of centimeter scale which is favourable for real applications. In this sense, it can be said that this approach has an advantage over the other techniques such as addressing group delay and group delay dispersion which involves accurate calculations. However, the meta-correctors obtained from our technique can be said to be nearly achromatic but not perfectly achromatic as there is a trade-off between the size of the metasurface and the achromaticity. The performance of lens-metasurface combination was studied using ray tracing and the phase gradient calculated was verified. Large area metasurfaces of centimeter scale were fabricated separately for chromatic and spherical aberrations utilizing a recent technique. The phase delay profiles was experimentally characterized and verified using phase measurement setup. To asses the performance of lens-metasurface combination, point spread function measurement and z-scan was carried out. To quantify spherical aberration correction, Zernike decomposition measurement was done on the phase front of the hybrid device. Finally, the overall performance of the lens-metasurface combination was assessed by imaging a standard target using the combination. To summarize the results, chromatic aberration correction of 80% in the wavelength range of 600-800 nm and spherical aberration correction of around 70% was achieved at 650 nm wavelength. Therefore it can be said that lens aberration is mitigated if not completely corrected. However, we believe that there is much room for improvement. Firstly, efficiency of the metasurfaces can be improved by optimizing the nanopillar design both in terms of Pancharatnam-Berry phase design and by considering near field interactions between the pillars. As discussed, with the current design, it is not possible to correct both chromatic and spherical aberration by using metasurfaces in cascading fashion. But it might be possible to correct various lens aberrations using series of high efficiency metasurfaces similar to cascading lenses used in an objective lens. The Pancharatnam-Berry phase based metasurfaces requires polarizers and quarter wave plates to function in circular polarization mode. This can be avoided by constructing metasurfaces with properly optimized propagation phase nanopillars which are essentially polarization independent. Taking into account all these factors, the proposed hybrid metacorrectors can have tremendous practical applications in imaging systems.

In quantum optics experiments with single photons, traditional optical components such as beam splitters, waveplates etc are utilized. The control that can be achieved on phase and polarization of light using metasurfaces can be tremendously useful in manipulating quantum states of photons. One such application was discussed in this work for one of the fundamental experiments of Quantum Optics, Hong Ou Mandel interference. A novel

device, Dual gradient metasurface was proposed for this purpose which acts as a 50/50 beam splitter but with additional functionality. A detailed theoretical calculation was carried out and electromagnetic simulations were performed to realize this metasurface. Nanofabrication steps followed to fabricate the metasurface were discussed in detail and proper optimization of fabrication steps were done to achieve 50/50 transmission which is necessary to observe quantum interference. Because of flexibility offered by metasurfaces in terms of phase and polarization design, one can think beyond the functionalities of conventional components. However, the performance of metasurfaces depends on the accuracy of nanofabrication. By decreasing the degree of tapering and by obtaining accurate dimensions of nanopillars, one can avoid undesirable diffraction orders. Designing metasurfaces to manipulate entangled photon states can be promising for future compact quantum devices.

All in all, in this thesis various aspects of phase gradient metasurfaces are discussed as a beam deflector, meta-corrector and as novel 50/50 beam splitter. Various stages of metasurface design such as analytical calculation, electromagnetic simulation, nanofabrication and optical characterization are discussed in detail. The tremendous potential of metasurface are realized for various applications at the same time their limitations and future prospects are also stated.